Dissertation

Analysis of 3D Shape Measurement for Fringe Projection Profilometry based Intraoral Scanner

Graduate School, Myongji University

Department of Mechanical Engineering

Furqan Ullah

Dissertation Advisor Professor Kang Park

February, 2014

명지대학교

Analysis of 3D Shape Measurement for Fringe Projection Profilometry based Intraoral Scanner

Submitted in partial fulfillment of the requirements for the Ph.D. degree in Mechanical Engineering

December, 2013

Graduate School, Myongji University

Department of Mechanical Engineering

Furqan Ullah

Analysis of 3D Shape Measurement for Fringe Projection Profilometry based Intraoral Scanner

Graduate School, Myongji University

Department of Mechanical Engineering

Furqan Ullah

We hereby recommend that the dissertation by the above candidate for the Ph.D. degree in Mechanical Engineering be accepted.

Chair, Evaluation Committee Kye Han Rhee, Ph.D. (Signature)

Member, Evaluation Committee Kang Park, Ph.D. (Signature)

Member, Evaluation Committee Soo Jin Lee, Ph.D. (Signature)

Member, Evaluation Committee Seungjae Min, Ph.D. (Signature)

Member, Evaluation Committee Ji Hyun Yang, Ph.D. (Signature)

December, 2013

Dedicated to my dear parents

and

my professor Kang Park

Acknowledgments

I would like to express my deepest gratitude and appreciation to my advisor, **Prof. Kang Park, Ph.D.**, for his excellent guidance, support and enthusiastic encouragement throughout this work. His teachings were inspiring. Without his help, support, and patience, this dissertation would not have been possible.

I would also like to thank the chair **Kye Han Rhee**, **Ph.D.**, and other members in my dissertation review committee, **Soo Jin Lee**, **Ph.D.**, **Seungjae Min**, **Ph.D.**, and **Ji Hyun Yang, Ph.D.**, for their valuable time and suggestions.

Finally, thanks are also extended to my Korean friends and colleagues here at the Myongji University, specially Gun Su Lee, Song Min Hong, and Woo Song Park for their support.

Table of Contents

Analysis of 3D Shape Measurement for Fringe Projection Profilometry based Intraoral Scanner

Furqan Ullah
Department of Mechanical Engineering
Graduate School, Myongji University
Directed by Professor Kang Park

During recent years, 3D shape measurement is becoming increasingly important in many industrial applications. Representative applications of 3D shape measurement include precision shape measurement for production control, reverse engineering, volume measurement, skin surface measurement for cosmetics and medicine, body shape measurement, intraoral dental measurement, forensic science inspections, microscale measurements, and entertainment, etc. Many 3D measurement systems have already been developed based on different principles, resulting in different accuracy, resolution, speed, and scanning efficiency. Among numerous systems to perform 3D measurement, fringe projection based 3D measurement system has become an increasingly popular because of its numerous advantages including real-time, fast, flexible, robustness, exactness, and high resolution. The research work of this dissertation presents the analysis of 3D shape measurement systems based on fringe projection profilometry. Four mathematical models of 3D measurement systems based on collimating and non-collimating projections are evaluated, and analysis and performance comparison of the phase-to-coordinate relation is presented.

Due to the restrictions of size and volume on the 3D scanner for dental applications, it is not easy to perform non-contact profile scanning in the mouth cavity. In this research, a novel collimating illumination based 3D intraoral scanner is presented for the measurement

of tooth profiles in the mouth cavity. In addition, nonlinear system models are proposed for collimating illumination that gives a more accurate mathematical representation of the system, thus improving the shape measurement accuracy. In order to test and verify the methodology and used algorithms in the development of intraoral scanner, we present a real-time virtual 3D scanner which is very similar to the real-world digital fringe projection (DFP) profilometry based 3D scanner. Finally, optical and simulation measurement results are presented to verify the feasibility and performance of the developed algorithms and systems.

Chapter 1. Introduction

During recent years, 3D shape measurement is becoming increasingly important in many industrial applications. Representative applications of 3D shape measurement include precision shape measurement for production control, reverse engineering, volume measurement, skin surface measurement for cosmetics and medicine, body shape measurement, intraoral dental measurement, forensic science inspections, microscale measurements, and entertainment, etc. In order to perform part inspection and quality control in the manufacturing industry, the objects need to be scanned and analyzed against computer-aided design (CAD) models, so that possible errors can be detected. For this purposes, many industries use contact-based 3D shape measurement system such as Coordinate Measuring Machine (CMM), coordinate measurement arm, and laser tracking systems. Use of physical contact based systems lead to some disadvantages such as time consuming, scratches on soft surfaces, and expensive. On the other hand, non-contact structured-light technology based 3D shape measurement systems such as fringe projection based 3D scanner has several advantages on real-time measurement, fast, flexible, robustness, exactness, inexpensive, and high resolution [1-5].

In the fringe projection based systems, the structured light of the fringe pattern is projected onto the shape of the object, mostly fringe strip patterns with sinusoidal intensity distributions. The charge-coupled device (CCD) captures the projected patterns which are modulated by the object profile and then transmitted to the host computer for image processing, reconstruction of the depth of the object shape, display, and so forth [6-9]. A flow chart of the 3D shape measurement based on fringe projection profilometry methods is presented in Fig. 1.

The shape measurement technique by using optical fringe patterns is often referred as Shape Measurement based on Fringe Projection (SMFP) and the shape measurement by using a computer generated digital fringe patterns with digital projectors is reference as Shape Measurement based on Digital Fringe Projection (SMDFP). A schematic diagram of a typical SMDFP system with one camera and one light source can also be seen in Fig. 1 that shows the hardware setup of the SMDFP system in which a light source projects fringe pattern onto the object and a camera captures the modulated fringe pattern by having some distance from the optical axis of the light source. The final output is a dense point cloud

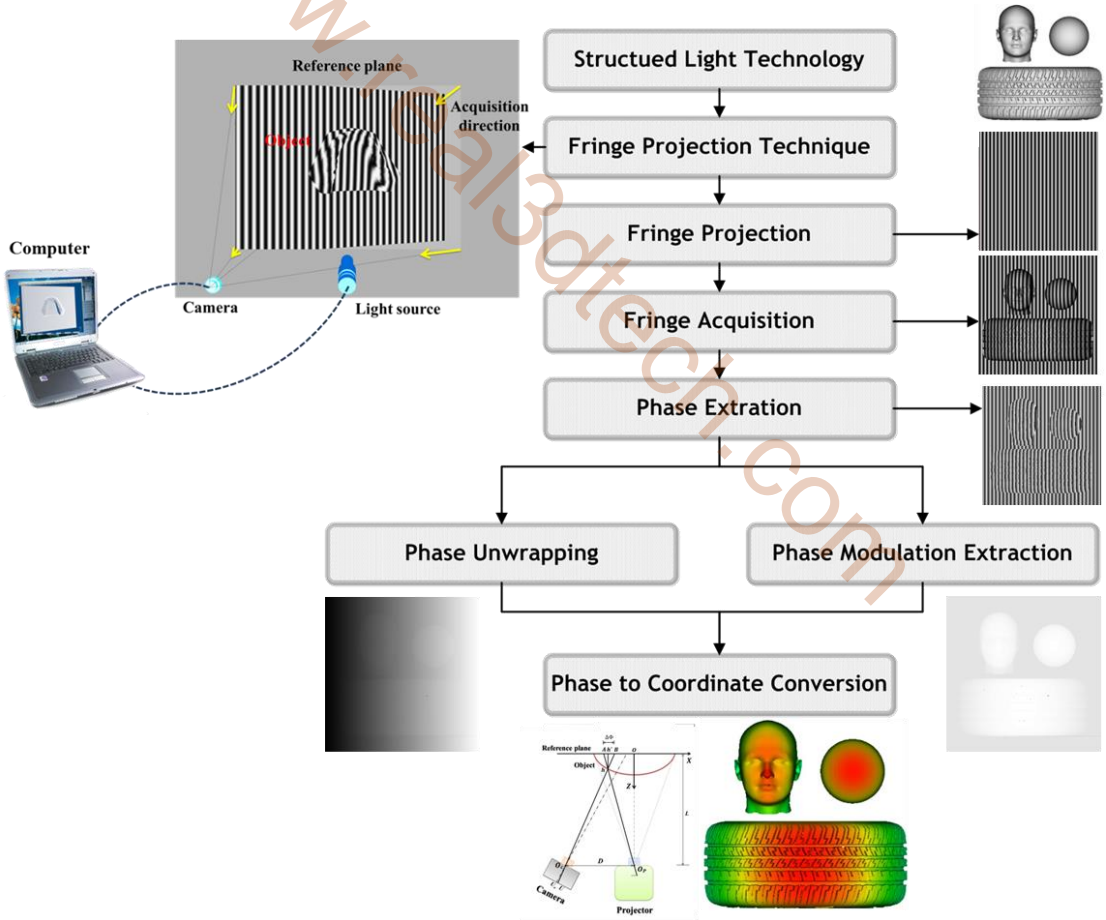

Fig. 1: Flowchart of the methods involved in 3D shape measurement based on fringe projection profilometry

that represents the surface of the object.

The core function of both systems is the pattern switching or phase shifting which is a challenging task in optical scanning system. In this system, the phase shifts of the projected fringe patterns are controlled by a mechanical device (i.e., piezoelectric transducer (PZT)) that expands or contracts with an externally applied voltage. If the applied voltage varies smoothly, a phase shift of a desired form or series of steps can be produced. The reciprocating motion of the PZT and the obtained phase shifts are not proportional due to the mechanical nature of the PZT. Therefore, the calibration of the PZT for accurate phase shift is a critical and challenging issue if good measurement results are to be obtained [9-16]. On the other hand, the phase-shifts in SMDFP is controlled by the computer which has several advantages on measurement speed and system cost [17-20].

1. Motivation and Research Objectives

As mentioned above, non-contact 3D shape measurement system has many advantages over the contact based 3D measurement, however, it is still passing the development stage and its potentials have not been fully exploited. In order to make it more robust and accurate, improvements are needed in ease of calibration, measuring the complex shapes, measurement accuracy, and measurement speed. The mathematical models for SMFP can be classified into two categories, geometry based models and calibration matrix based models [21]. Compared with the calibration model, the geometry based models has become more popular and studied by numerous researchers, because it has more potential to achieve high accurate measurements. However, geometry based models require a large number of parameters in order to calibrate the system, and there is not a specific system setup for SMFP, but the system setup can be represented in several ways. Therefore, it is required to modify mathematical models and new algorithms need to be developed.

Complex surfaces or surfaces with large range of normal directions require multiple patterns with

different fringe pitches for a single measurement which is not desired for real-time and fast applications. Therefore, new algorithms and methods need to be developed in order to measure shapes with large range of normal directions.

In dentistry, a very accurate 3D tooth model requires to be constructed from a human jaw. However, there are several issues involve in SMFP system that make this system complicated and all those issues have not been fully exploited yet. The research work of this dissertation focuses on, several possible issues related to development of a dental 3D intraoral scanner (IOS) based on optical fringe projection technique. The ultimate objective of this dissertation is to develop a complete 3D intraoral scanning system, and a general purpose computer-aided scanning software for the analysis of 3D shape measurement systems. The main goals include:

- Analysis of 3D shape measurement in order to develop an intraoral scanner
- Development of a general purpose computer-aided 3D scanning software

In order to achieve the goals, the following tasks will be implemented and completed:

- Investigate the issues and problems in the development of an intraoral scanner

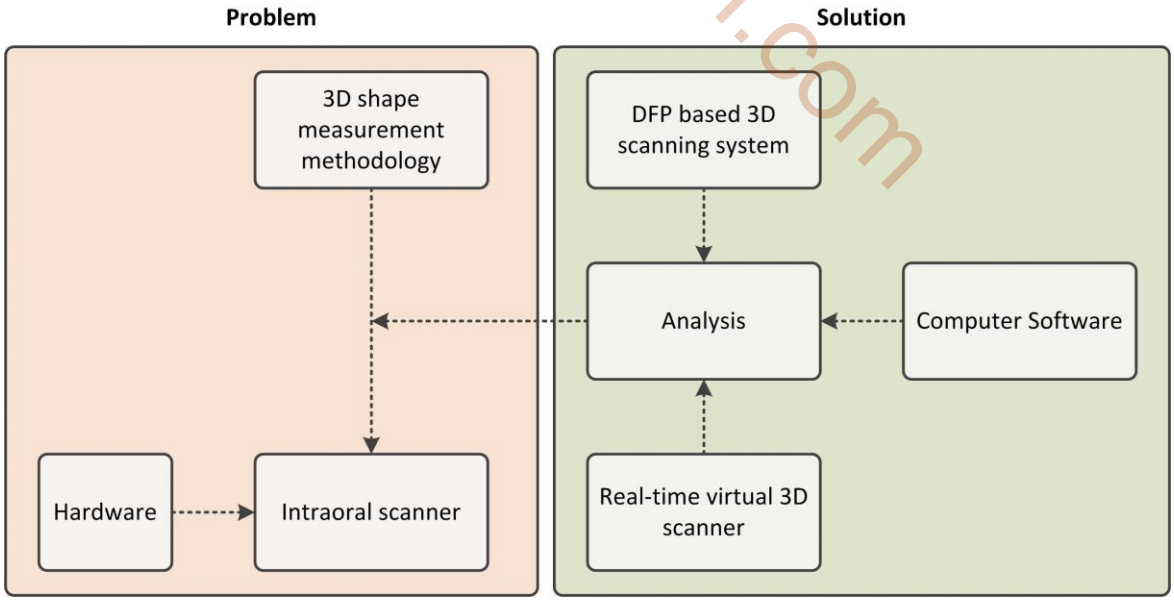

Fig. 2: Description of problem and solution of the research of this dissertation

- Improve the existing method and develop new approaches for acquiring the accurate point cloud data
- Develop a real-time virtual 3D scanner in order to analyze different kinds of 3D scanning system models and to verify the proposed methods and algorithms
- Develop a SMDFP system in order to test and verify the scanning methodology
- Improve the various existing algorithms that involve in the pre and post processing

In addition, Fig. 2 presents the problem and solution of the research of this dissertation which describes that in order to develop an intraoral scanner, the adopted methodology was analyzed and verified using a virtual 3D scanner, DFP scanning system, and computer software. Since the hardware of the intraoral scanner was not easy to develop, therefore, in the meantime we developed a real-time virtual 3D scanner that helped us to analyze the system and improve existing algorithms. The virtual 3D scanner was a perfect addition to analyze the adopted methodology and algorithms, however, it was necessarily required to analyze the effectiveness of the adopted methodology using an optical scanning system. Therefore, we developed a real-world DFP based 3D scanning system.

1.1 3D Intraoral Scanner

Traditionally, dental stone model forms the basis for the dentistry to manufacture crowns and frames attached to natural teeth. The traditional workflow has proven itself in dentistry; however, it involves serious issues and problems such as dimensional changes in the model. A 3D intraoral scanner could solve some of the issues associated with cast production, traditional impression taking, and it could also provide a digital workflow with digital output data [22]. Some advantages of an intraoral scanning are the production of the prosthesis can be performed directly after 3D optical measurement, absence of many intermediate steps, reduced pain level for the dental patient, patients no longer need to

make multiple visits to the clinicians, and there is no need for temporary restorations.

Due to the restrictions of size and volume on the 3D scanner for dental applications, it is not easy to perform non-contact profile scanning in the mouth cavity and there are not so many 3D profile measurement tools designed specifically for narrow spaces, for example, to scan the tooth shape of a human jaw. Some existing intraoral scanners adopted non-contact optical technologies such as structured light interferometry and phase shifting, active and passive stereovision, confocal microscopy, triangulation, photogrammetry, and optical coherence tomography [23-28]. However, most intraoral scanners are passing the prototype testing phase and only some devices are currently available on the market. All the existing intraoral scanners try to face with problems and disadvantages of traditional impression fabrication process and are driven by several non-contact optical technologies and principles. Most of them are largely under development; accuracy is still needed to be improved in current scanners.

The research work of this dissertation presents the development procedure of a 3D intraoral scanner based on structured light fringe projection technology. In this research work, three devices were developed with different specifications. In the first device, piezoelectric transducer (PZT) was utilized in order to move the graticule with fringe patterns. Second device replaced PZT with the voice coil actuator (VCA) in order to obtain more accurate phase shifts as well as gain the stability of the device. Third device was the improved version of the second hardware in term of design, specifications, and accuracy.

1.2 Real-Time Virtual 3D Scanner

In 3D shape measurement, several algorithms for point cloud construction are crucial to the system's measurement accuracy such as phase-to-coordination conversion, phase

wrapping and unwrapping, noise reduction, refining, and filtering algorithms, etc. It is so important to test and verify all these algorithms and involved methods in a controlled atmosphere before performing the real implementations. For this purpose, simulations have always been used to verify the effectiveness of new developed algorithms and systems. Extensive research has been done on the SMFP technology but not on the virtual simulation of the 3D measurement procedures and methods. In this research work, we present a complete real-time virtual 3D scanner which is very similar to the real-world optical SMDFP system. Real-time virtual 3D scanner is a high resolution SMDFP technology based virtual scanner that scans virtual or CAD objects in the virtual environment. It performs projection of computer generated fringe patterns onto the virtual 3D object, virtually images capturing, point cloud acquisition, reconstruction, and display processes, simultaneously. The virtual system comprises a virtual camera, a virtual projector, and a virtual reference plane. All the virtual parameters can be easily adjusted according to the real-world 3D shape measurement system.

In this system, we created a very similar system model like our 3D IOS, and before finalizing the hardware of the IOS device, we tested the complete scanning procedure that involved in the intraoral scanning.

1.3 Digital Fringe Projection based 3D Shape Measurement

Extensive research has been done on real-time systems based on different principles, resulting in different accuracies, resolutions, sampling speeds, and measurement efficiencies [1]. During recent years, the use of fringe projection techniques for generating three-dimensional surface information has become one of the most active research areas in optical metrology. S. Zhang deeply focused on real-time 3D shape measurement technique

using the digital fringe projection technique, and explained the most recent efforts towards advancing this technology and addressed the critical challenges [7]. In this technique, the fringe patterns are generated by a computer, projected through a digital display device such as Digital-Light-Processing (DLP) projector or Liquid-Crystal-Display (LCD) projector onto the object and obtained the height of an object from deformed fringe images, which are modulated by the object surface. Some advantages of DFP technology are different shapes of patterns can be generated easily, the shape of the patterns can be accurately controlled by computer software, and the errors caused by mechanical devices for phase shifting are eliminated, etc.

In order to do real-time 3D shape measurement, fringe pattern images must be captured rapidly, 3D reconstruction must be performed quickly, and the reconstructed 3D shapes must be displayed instantaneously in real time. Hence, the coordinate acquisition, reconstruction, and display processes must be completed simultaneously and quickly. In real-time SMDFP systems, basically two approaches are most common: one is to use a single pattern (i.e., color pattern) and the other is to use multiple patterns. Numerous researchers have been used a single pattern technique [29-31]. Huang et al. implemented a single color fringe pattern technique in which a pattern was produced by a DLP projector. Zhang et al. developed a color structured light technique for high-speed scans of moving objects [32]. The issue to use color patterns is, the shape measurement is affected to various degrees by the variations of the object's surface color. In general, fringe projection methods require more projection patterns if good measurement results in term of higher accuracy and capability of handling surface discontinuities are to be obtained. However, single pattern technique sacrifices accuracy for improved acquisition speed.

This dissertation presents a SMDFP system that is capable of performing small and large

scale measurements in real-time and can be applied to various applications. The system utilizes a digital projection unit to project the desired phase-shift patterns onto the object and a CCD imaging device to capture the projected patterns which are modulated by the object shape and then transmitted to the host computer for image processing, reconstruction, and display.

We believe that, to develop such a DFP based scanning system was essential for the development of IOS device because IOS is a micro-scale device and very sensitive to several issues such as phase-shifts, vibration, etc. Therefore, it was required to develop a system with the controlled parameters in order to verify and effectiveness of the existing and proposed methods and algorithms.

1.4 Computer Software

The important portion of the research work of this dissertation is to design and develop a general-purpose computer-aided scanning software. The software has ability to perform real-time DFP based virtual 3D scanning, real-time DFP based optical scanning, and 3D intraoral scanning. In addition, the system has various functional modules such as controls for system devices, image processing and visualization, point cloud and triangular model visualization, mesh filtering and refinement, and post-processing, etc.

2 Dissertation Outline

The research conducted in this dissertation is presented in the following manner:

Chapter 2 describes the theory of 3D intraoral scanning. Chapter 3 gives the development procedure of real-time virtual 3D scanner. Chapter 4 gives the analysis and performance comparison of 3D shape measurement system models. Chapter 5 describes the development of SMDFP system. Chapter 6 explains the development procedure of the IOS

device. Chapter 7 summarizes the conclusions reached from this dissertation.

.

Chapter 2. Theory of 3D Intraoral Scanning

This chapter gives a theory of the existing and improved algorithms such as phase-shifting, phase-unwrapping, phase-to-coordination conversion techniques, and camera calibration, filtering, smoothing, registration, and merging, etc.

2.1 The Fringe Pattern:

In phase-shifting technique, a fringe pattern can be considered as a sinusoidal signal

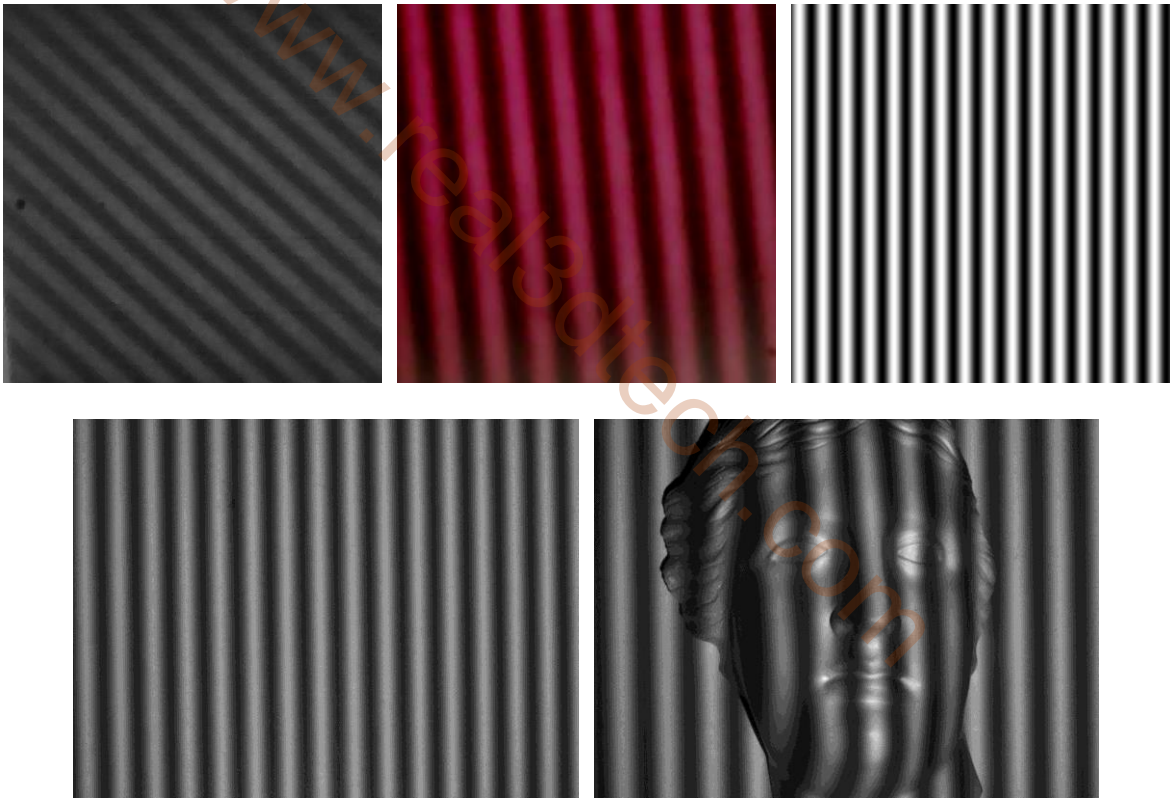

Fig. 3: Fringe patterns: (top left) fringe pattern created by an optical grating with the pitch value 200 mm, (top middle) red laser fringe pattern created by an optical device with the pitch value 400 mm, (top right) a fringe pattern created by Eqn.1, (bottom left) a fringe pattern projected onto a flat surface using a DLP projector, (bottom right) a fringe pattern projector onto a sculpture using a DLP projector

fluctuation in two-dimensional space and can be created with Eqn. 1.

$$I(i,j) = a(i,j)\left[1 + b(i,j)\cos\Phi(i,j)\right] + n(i,j) \quad (1)$$

where (i, j) are the indices for pixels, and for a given pixel (i, j), $I(i, j)$, $a(i, j)$, $b(i, j)$, $\Phi(i, j)$, $n(i, j)$ are intensity, background, visibility, phase, and noise functions, respectively. However, the fringe patterns generated using graticule or grating have non-sinusoidal waveforms and due to mechanical nature of the optical device, achieved phase-shifts are not often linear and precise which causes noise and jumps in the point cloud data. Similar problem could also happen with the digital fringe patterns projected by digital projectors. For example, if the intensity of the projector and gamma effect are not properly adjusted. Some fringe patterns generated from different devices are presented in Fig. 3.

2.2 Phase-Shifting Method

The phase-shifting interferometry (PSI) method was first introduced by Bruning et al [33]. in 1974 for testing optical components using a video CCD array; later it became the most common technique used to detect the modulating phase of interferograms. Numerous researches have been done on the design of PSI algorithms for classical and digital interferometry. All the PSI algorithms will give the accurate results if the following conditions are fulfilled:

- The phase-shifts between the phase-shifted interferograms exactly the same.
- The light-intensity range should be within the linear range of the CCD.
- The device (i.e. PZT) moves the graticule linearly.
- Mechanical vibration or other perturbations should be very small during the capturing of interferograms.

However, it is not possible to design such a system in which we can fulfill all the above conditions, sometimes one or several conditions are not met for both SMFP and SMDFP systems. In this case, a robust and accurate algorithm needed to be designed. The most common sources of errors in PSI are:

- Incorrect phase shift between data frames
- Vibrations
- Sensors non-linearity
- Quantization errors
- Stray reflections
- Intensity fluctuations
- Frequency stability

Some of the above errors occur because of the incorrect system setup and some happen because of the incompatibility of hardware with PSI [34]. For example, incorrect phase-shift between data frames produces large errors in the reconstructed phase due to incorrect phase shifter calibration, air turbulence or vibration. These kinds of errors can be reduced by using the large number of fringe pattern images and even can be eliminated by using the digital system setup such as digital fringe pattern.

The basic equation for the phase-shifting interferogram can be written as:

$$I(i,j,t) = a(i,j) + b(i,j)\cos\left[\Phi(i,j) + \delta(t)\right] \tag{2}$$

where a(i, j) is the intensity bias, b(i, j) is half the peak-to-valley intensity modulation, δ(t) is a time-varying phase shift, and Φ(i, j) is the phase to be solved at each point in the interferogram. There are three unknowns in the equation, a, b, and Φ; therefor, three simultaneous equations are needed to evaluate the unknowns. Many phase-shifting algorithms are designed because of different time-varying phase shifts.

2.2.1 3-Step Phase-Shifting Algorithm

Since there are three unknown in Eqn. 1, the minimum number of patterns will be three. The three equations can be expressed as:

$$I_1(i,j) = a(i,j) + b(i,j)\cos[\Phi(i,j) - \delta] \tag{3}$$

$$I_2(i,j) = a(i,j) + b(i,j)\cos[\Phi(i,j)] \tag{4}$$

$$I_3(i,j) = a(i,j) + b(i,j)\cos[\Phi(i,j) + \delta] \tag{5}$$

where I_1, I_2, I_3 are the intensity distributions with the phase-shifts of –δ, 0, and +δ, respectively. Simultaneously solving Eqn. 4-5, the wrapped phase map Φ(i, j) can be obtained as:

$$\Phi(i,j) = \tan^{-1}\left[\left(\frac{1-\cos\delta}{\sin\delta}\right)\frac{I_1(\mathrm{i,j}) - I_3(\mathrm{i,j})}{2I_2(\mathrm{i,j}) - I_1(\mathrm{i,j}) - I_3(\mathrm{i,j})}\right] \tag{6}$$

If we use the value of phase shift $\delta = 2\pi/3$, the above equation becomes:

$$\Phi(i,j) = \tan^{-1}\left[\sqrt{3}\frac{I_1(\mathrm{i,j}) - I_3(\mathrm{i,j})}{2I_2(\mathrm{i,j}) - I_1(\mathrm{i,j}) - I_3(\mathrm{i,j})}\right] \tag{7}$$

The 3-step algorithm is the simplest form of PSI method because it uses the minimum number of fringe patterns. However, it is very sensitive to the phase-shift errors. In order to obtain more accurate wrapped phase map, other algorithms use more than three phase-shifted fringe patterns.

2.2.2 4-Step Phase-Shifting Algorithm

Four-step algorithm is the most common and widely used algorithm in PSI. It has several advantages over the other algorithms such as it reduces the inaccurate phase shifts between data frames, more robust against disturbing influences, and computational time.

The fringe image intensities of the four-step phase-shifting algorithm with a phase shift of $\pi/2$ are written as:

$$I_1(i,j) = a(i,j) + b(i,j)\cos[\Phi(i,j)] \tag{8}$$

$$I_2(i,j) = a(i,j) + b(i,j)\cos[\Phi(i,j) + \pi/2] \tag{9}$$

$$I_3(i,j) = a(i,j) + b(i,j)\cos[\Phi(i,j) + \pi] \tag{10}$$

$$I_4(i,j) = a(i,j) + b(i,j)\cos[\Phi(i,j) + 3\pi/2] \tag{11}$$

Using the above four equations, the wrapped phase can be determined as:

$$\Phi(i,j) = \tan^{-1}\left[\frac{I_4(\mathrm{i},\mathrm{j}) - I_2(\mathrm{i},\mathrm{j})}{I_1(\mathrm{i},\mathrm{j}) - I_3(\mathrm{i},\mathrm{j})}\right] \tag{12}$$

The intensity data for the four-step phase-shifting algorithm can also be evaluated to

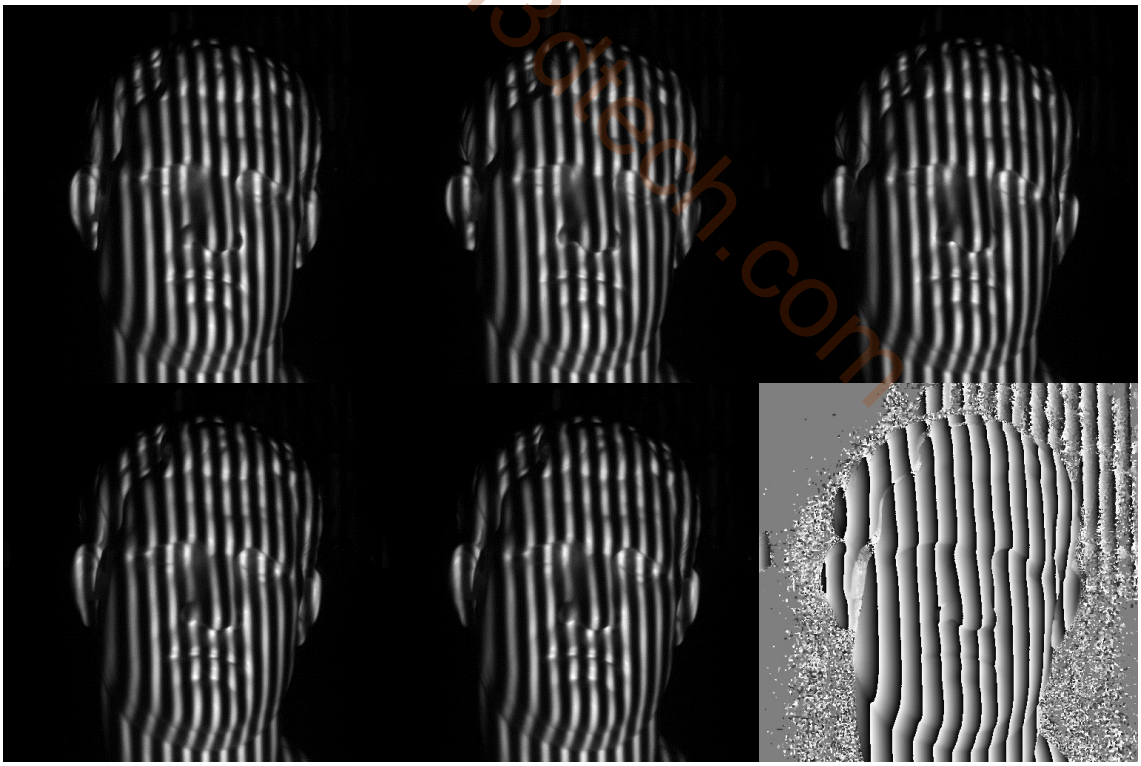

Fig. 4: 5-Step phase-shifting method: five patterns are projected onto a sculpture and obtained the wrapped phase using Eq. 19

determine the data modulation γ(i, j) across the interferogram.

$$\gamma(i,j)=\frac{2\sqrt{[I_4(i,j)-I_2(i,j)]^2+[I_1(i,j)-I_3(i,j)]^2}}{I_1(i,j)+I_2(i,j)+I_3(i,j)+I_4(i,j)} \tag{13}$$

The above equation is very useful for the evaluating of the quality of the data. The numerator can be called as intensity modulation and the denominator can be named the average intensity. However, the value of γ(i, j) is application dependent.

2.2.3 5-Step Phase-Shifting Hariharan Algorithm

A very popular five-step algorithm offer advantages in reduced uncertainties in the phase calculation, reduced sensitivity to phase-shifter calibration, and robust to detuning. The five-phase stepped interferograms with a phase shift of π can be written as:

$$I_1(i,j)=a(i,j)+b(i,j)\cos[\Phi(i,j)-2\pi] \tag{14}$$

$$I_2(i,j)=a(i,j)+b(i,j)\cos[\Phi(i,j)-\pi] \tag{15}$$

$$I_3(i,j)=a(i,j)+b(i,j)\cos[\Phi(i,j)] \tag{16}$$

$$I_4(i,j)=a(i,j)+b(i,j)\cos[\Phi(i,j)+\pi] \tag{17}$$

$$I_4(i,j)=a(i,j)+b(i,j)\cos[\Phi(i,j)+2\pi] \tag{18}$$

By solving above five equations the simplest form of the wrapped phase map can be expressed as:

$$\Phi(i,j)=\tan^{-1}\left[\frac{2\{I_4(\mathrm{i,j})-I_2(\mathrm{i,j})\}}{I_1(\mathrm{i,j})-2I_3(\mathrm{i,j})+I_5(\mathrm{i,j})}\right] \tag{19}$$

An example of 5-step phase-shifting algorithm is presented in Fig. 4 in which five phase-shifted images and a wrapped phase map can be seen.

2.2.4 Carré Algorithm for Unknown Phase-shifts

The optical SMFP system which uses graticule in order to produce phase-shifts often deal with non-linear calibration problems because small amounts of phase-shifting nonlinearity can introduce large error in the measurements. Carré algorithm uses four fringe patterns and treats the amount of phase-shift as an unknown. The four-phase stepped interferograms with a linear phase shift of 2δ can be expressed as:

$$I_1(i,j) = a(i,j) + b(i,j)\cos[\Phi(i,j) - 3\delta] \tag{20}$$

$$I_2(i,j) = a(i,j) + b(i,j)\cos[\Phi(i,j) - \delta] \tag{21}$$

$$I_3(i,j) = a(i,j) + b(i,j)\cos[\Phi(i,j) + \delta] \tag{22}$$

$$I_4(i,j) = a(i,j) + b(i,j)\cos[\Phi(i,j) + 3\delta] \tag{23}$$

Since there are four unknown and fortunately we also have four equations, the final obtained wrapped phase map from the four equations can be determined as:

$$\Phi(i,j) = \tan^{-1}\left[\frac{\sqrt{3\{(I_2(i,j) - I_3(i,j)) - (I_1(i,j) - I_4(i,j))\}\{(I_1(i,j) - I_4(i,j)) + (I_2(i,j) - I_3(i,j))\}}}{(I_2(i,j) + I_3(i,j)) - (I_1(i,j) + I_4(i,j))}\right] \tag{24}$$

Carré algorithm is very convenient for non-linear optical devices because the value of the phase-shift is not very important as long as the phase-shift between consecutive frames is a constant.

2.3 Two-dimensional Phase-Unwrapping Method

The phase obtained from the equations (7), (12), (19), (24) is called the wrapped phase map (modulo 2π of the original phase) due to the arc tangent function involved in the phase-estimation process. However, the obtained wrapped phase is in the range of [-π, +π] along with the saw-tooth like discontinuities. In order to correct these 2π discontinuities to

obtain a continuous phase map, a phase-unwrapping algorithm is required. The relationship between the wrapped and the unwrapped phases can be seen in Fig. 5 and expressed as:

$$\Phi_u(i,j) = \Phi(i,j) + 2\pi k(i,j) \tag{25}$$

where $\Phi_u(i, j)$ is the unwrapped phase, and $k(i, j)$ is an integer-valued correcting field. A linear unwrapped phase can be obtained by adding or subtracting 2π according to the phase jump ranging from $-\pi$ to $+\pi$ or vice versa. However, there are several challenging issues involved in the computation of the linear phase such as:

1. Discontinuities and noise in the observed image, which may cause large changes in the measured data.
2. Dark or low intensity area in the image, which makes the unwrapping equation difficult or sometime impossible to solve.
3. Inconsistencies in the unwrapping process when following different paths.
4. Phase jumps and undersampling

In order to address above issues and computation difficulties, many phase-unwrapping algorithms have been proposed in the past and the number of new phase-unwrapping algorithms continues to grow [35-47].

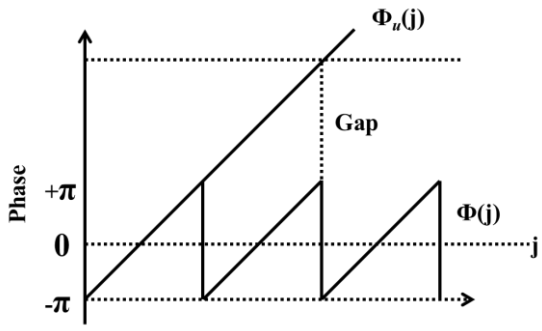

Fig. 5: Relationship between the wrapped and unwrapped phases

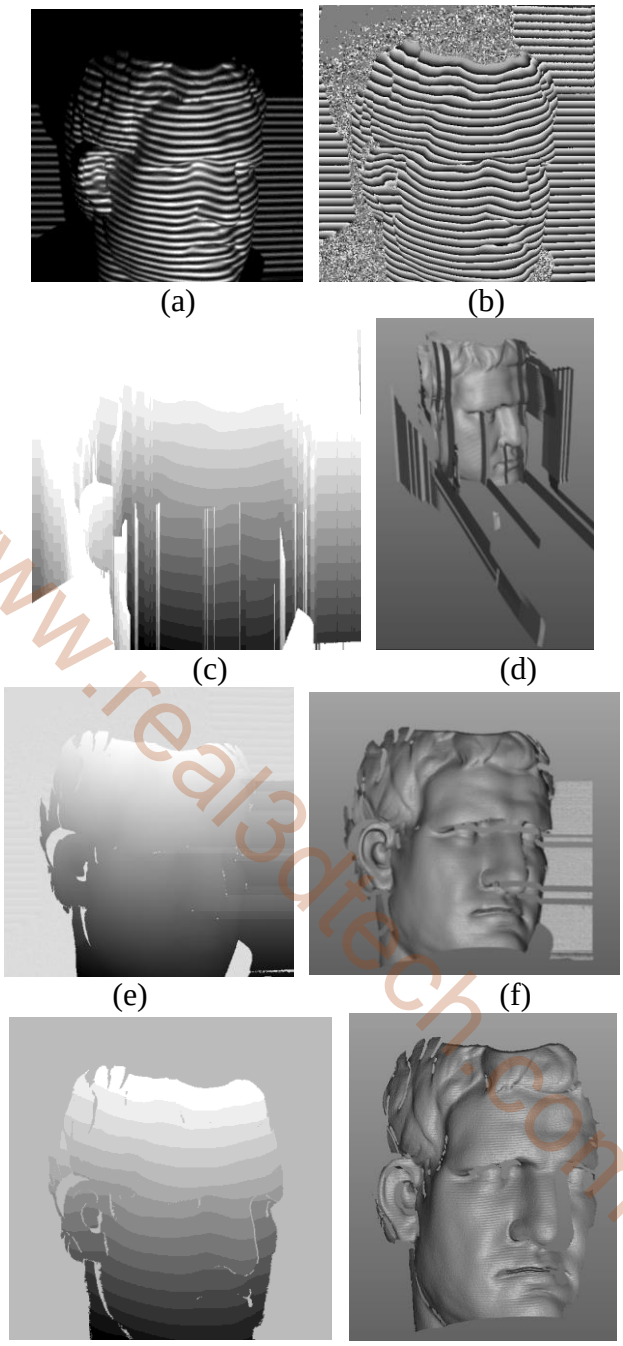

Fig. 6: 2D phase unwrapping: comparison of different phase unwrapping algorithms, (a) and (b) shows the one of the phase-shifted fringe patterns and the wrapped phase, respectively, 6(c) and (d) gives the results of the linear 2D phase unwrapping algorithm and the reconstructed mesh, respectively, 6(e) and (f) presents the results of simple flood-fill phase unwrapping algorithm without any quality map, and the reconstructed mesh, respectively, 6(g) and (h) shows the results of path-following quality guided algorithm and the reconstructed shape, respectively.

The unwrapping method can be classified as path-following, region-growing, cellular automata, least-squares, and simulated annealing methods. Furthermore, the path-following method can be sub-classified into quality-guided, minimum-discontinuity, Goldstein's branch-cut, and Flynn's mask-cut algorithms. A detailed review for unwrapping algorithms can be found in [48-49]. Among all the mentioned unwrapping methods, quality-guided method requires a least execution time and it is most robust to discontinuities and noise. For this method, it is absolutely necessary to use the phase-quality map for guidance. A phase-quality map is a 2D data array that identifies the quality or goodness of each pixel in a wrapped phase map. By the analyzing the quality map, we can remove the residues and unwrap the reliable data first, so that the phase-unwrapping errors limited to the smallest possible area. The path-following quality-guided algorithm may operate as follows:

1. Create a quality map from the wrapped phase map
2. Find the highest quality pixel and take its wrapped value as its unwrapped value
3. Unwrap all the neighbors of the current pixel
4. Add the unwrapped neighbors to a list
5. Find the pixel with the highest quality value in the list
6. Return to Step 3.

The advantages of quality-guided algorithms are, these algorithms relatively simple to implement, have low memory overheads, and do not find residues or create branch-cuts. The success of this algorithm relies on how good the quality or weight map is. Fig. 6 demonstrates the comparison of different phase unwrapping algorithms in which Fig. 6(a) and (b) shows the one of the phase-shifted fringe patterns and the wrapped phase using 4-step phase-shifting method, respectively. Fig. 6(c) and (d) gives the results of the linear 2D phase unwrapping algorithm and the reconstructed mesh, respectively. Fig. 6(e) and (f)

presents the results of simple flood-fill phase unwrapping algorithm without any quality map, and the reconstructed mesh, respectively. Fig. 6(g) and (h) shows the results of path-following quality guided algorithm and the reconstructed shape, respectively. As can be seen in Fig. 6, the basic algorithms cannot unwrap the residues or discontinuities area and create large disturbance in the reconstructed shape, on the other hand, the quality-guided algorithm with a quality map works correctly and is more efficient than the conventional algorithms.

Virtual simulation results was also performed and presented in Fig. 7 which shows the comparison of flood-fill without quality map and quality guided phase unwrapping

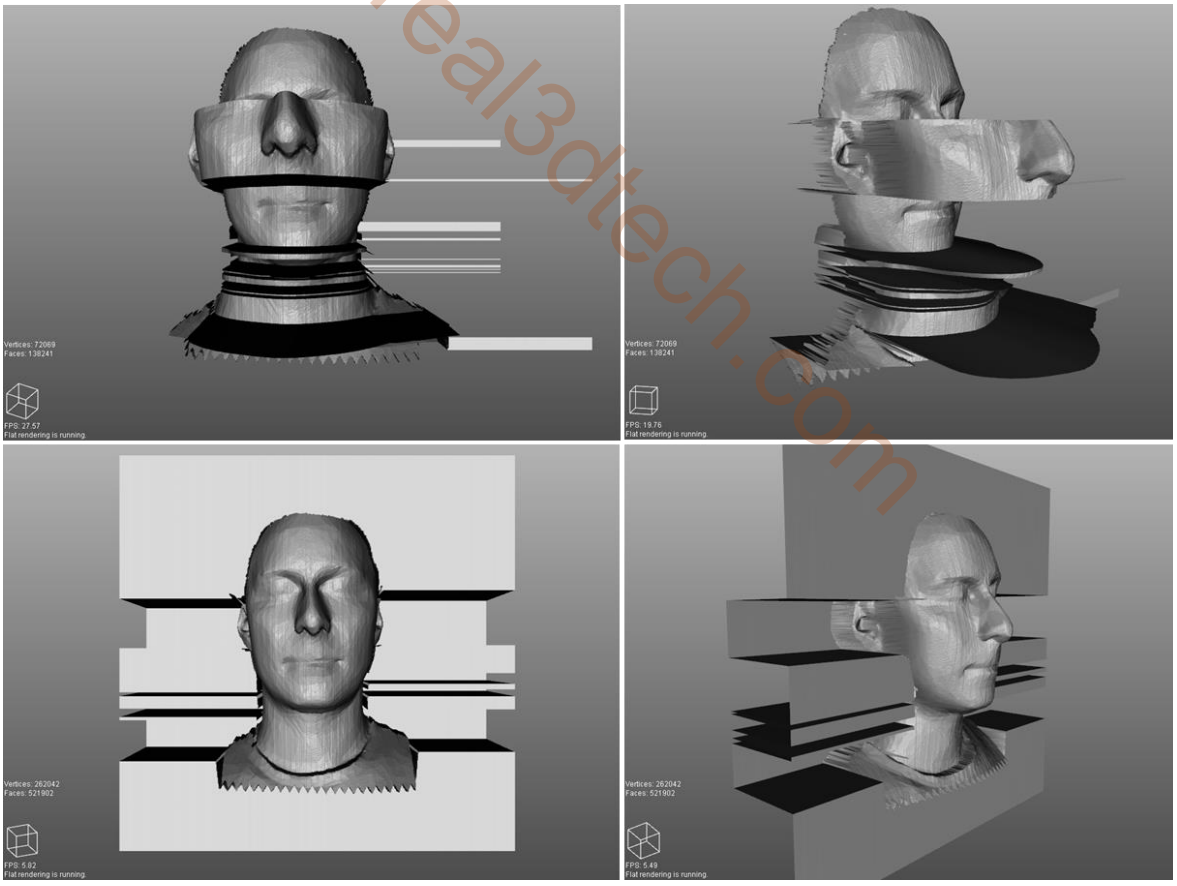

Fig. 7: 2D phase unwrapping: comparison of flood-fill (without quality map) and quality-guided (with quality map) phase unwrapping algorithms

algorithms. Some other phase unwrapping algorithms such as minimum discontinuity, branch-cut, and L^o also offer good performance; however, these methods are less practical and are not discussed in this dissertation [92].

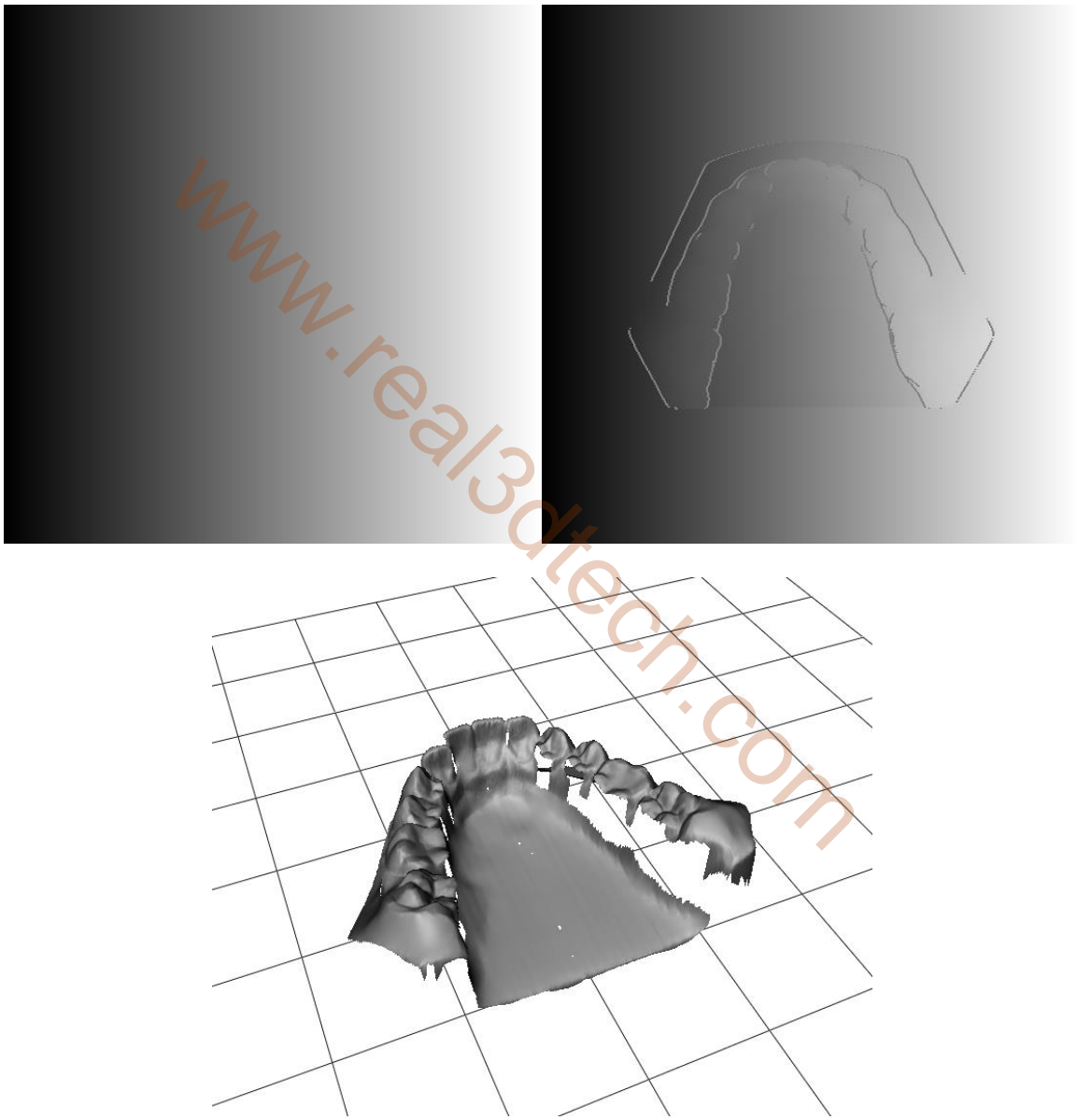

Fig. 8: Carrier phase removal: (top left) unwrapped phase map of the reference plane, (top right) unwrapped phase of the object, (bottom) phase distribution after carrier component removal

2.4 Two-Dimensional Carrier Removal Method

After obtaining the unwrapped phase map from the wrapped phase, in general, we need to remove the fringe relation carrier phase component in order to accurately estimate the 3D shape of the object. [51]. Depending on the linearity of the carrier phase component, the carrier phase can be classified into two kinds: linear carrier phase with the first-order function, and nonlinear carrier phase with being a higher-order function. The linear and non-linear carrier removal techniques can be further subdivided into spectrum-shift approach, average-slope approach, plane-fitting approach and reference-subtraction approach, phase-mapping approach, series-expansion approach, respectively [52-55].

Fig. 8 demonstrates the carrier phase removal using reference-subtraction technique. As can be seen in the figure, the reference phase map contains only the carrier phase, while the object phase map has both carrier and shape-related phases. When the reference phase map is subtracted from the object phase map, the final phase distribution of the object can be seen at the bottom of the Fig. 8 (bottom).

2.5 Mathematical Models for 3D Measurement Systems

The mathematical models for SMFP can be classified into two categories, geometry based models and calibration matrix based models. Compared with the calibration model, the geometry based models has become more popular and studied by numerous researchers, because it has more potential to achieve high accurate measurements. This dissertation focusses on the geometric based models and presents the analysis and performance comparison of four geometric models of 3D shape measurement systems in the next chapter.

2.5.1 Collimating Illumination based Model

Srinivasan et. al. [56] proposed one of the earliest mathematical model in 1984 for collimating illumination (the pitch of the strip pattern remains constant despite the distance to the projection unit) based 3D shape measurement system in which they used a laser as a projection unit with sinusoidal intensity generated by the polarization interferometer.

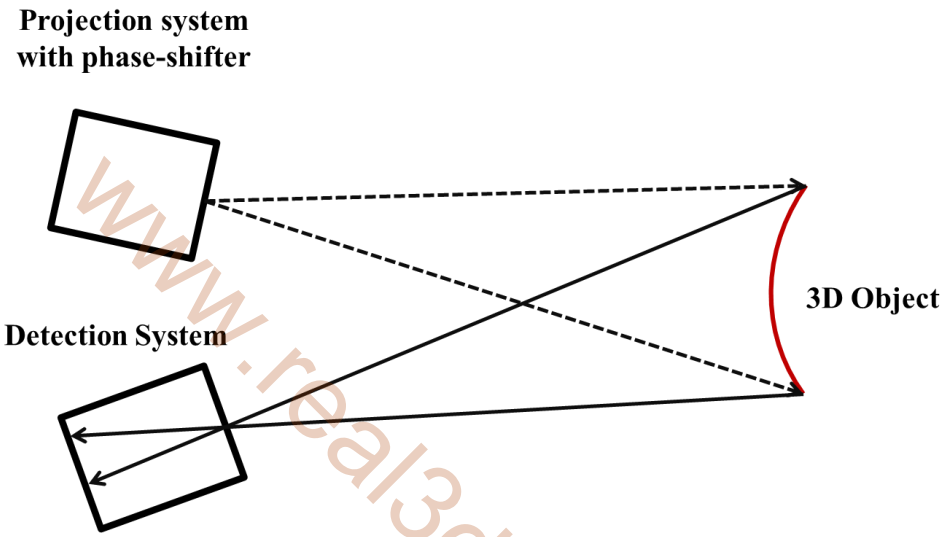

Fig. 9: Schematic diagram of the geometric model proposed by Srinivasan et. al.

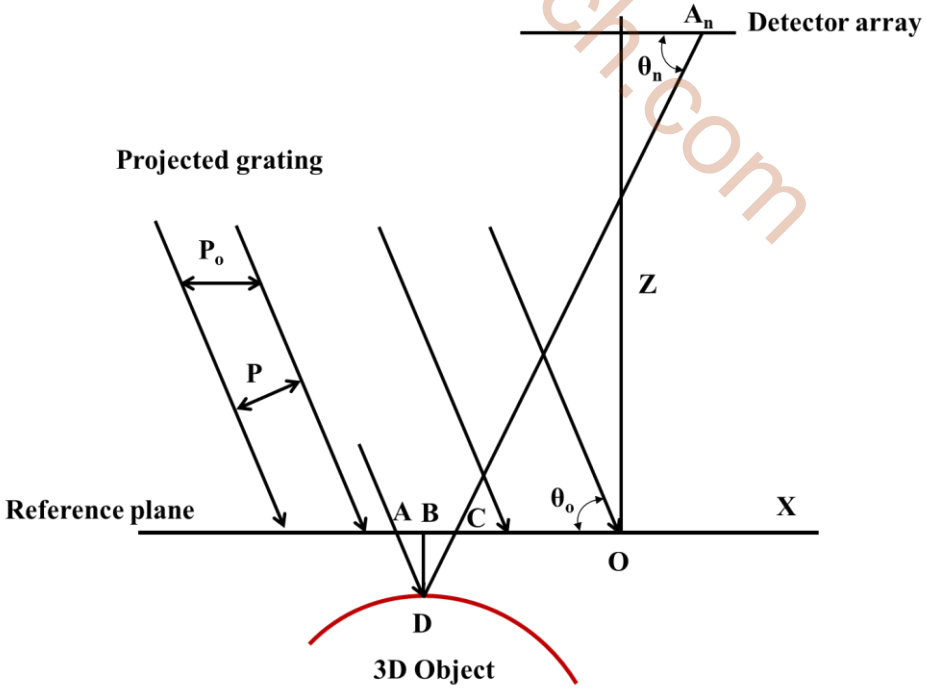

Fig. 10: Geometry relationship of the geometric model proposed by Srinivasan et. al.

Three images each were recorded for the reference plane and the object surface, with a phase increment of 120^o of the projected fringe pattern following each recording. The system consists of a projection unit with a phase-shifter and a light detector array. Fig. 9 shows the schematic diagram of the system's hardware and Fig. 10 describes the geometry relationship of the system. From Fig. 10, the height of the object at point *D* can be expressed as:

$$BD = \frac{AC \tan\theta_o}{1 + \tan\theta_o / \tan\theta_n} \tag{26}$$

where AC is the phase difference ΔΦ and can be written as:

$$AC = \frac{P_o}{2\pi} \Phi_{CD} \tag{27}$$

Some other collimating illumination based mathematical models were proposed by Quan et. al., Bashar et. al. and Agnès et. al. which can be reviewed in [57].

2.5.2 Non-collimating Illumination based Model

The popular cited mathematical model for SMFP system based on non-collimated projection is from Takeda et. al. [58]. Fig. 11 demonstrates the geometry relationship of the Takeda's model in which a projection unit, a capturing device, a reference plane, and a 3D object can be seen. The optical axes of a projector and a camera lie in the same plane and intersect a point near the center of the object. In the figure, y represents the coordinate in the field of view of the camera, D is the distance between the optical axes of the projector and camera, L is the distance between the optical center of the camera and the reference plane, and h is the height of the object to be measured. The height of the object can be expressed as:

$$h_y = \frac{L\Delta\Phi_y}{\Delta\Phi_y - \omega_o D} \tag{28}$$

where $\Delta\Phi_y$ is the change in phase, and ω_o is the frequency of the fringe pattern on the projector image plane and can be written as:

$$\omega_o = \frac{\omega_p \cos\theta}{G_p} \tag{29}$$

where ω_p is the frequency of the fringe pattern on the projector's grating and G_p is the magnification factor of the projector.

Several other mathematical models for SMFP systems have been developed over the years [60-66] and recently there has been an increasing interest in the development of flexible

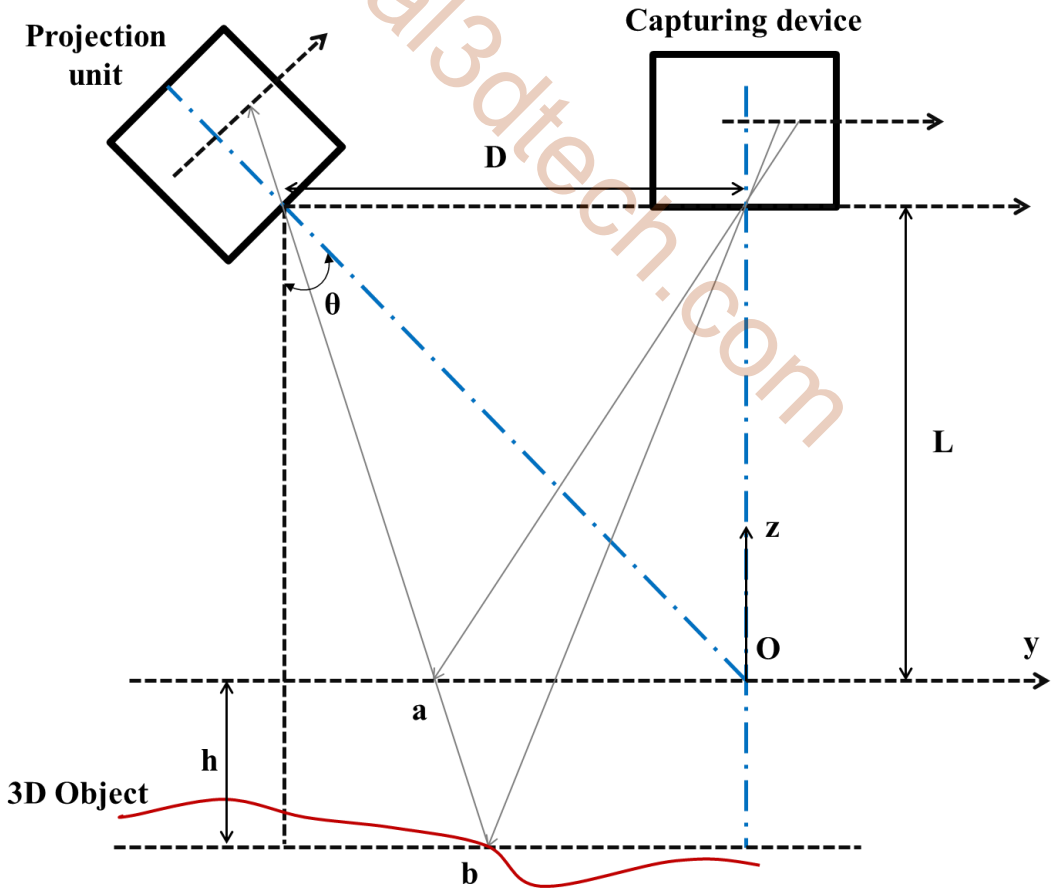

Fig. 11: Geometry relationship of the SMFP model proposed by Takeda et. al.

and generalized models [67-70] that are capable of automatically determining the geometric parameters of the experimental setup even when the camera, projector and object are placed arbitrarily.

2.6 Parameter Estimation (Camera Model)

The height for each pixel obtained from the geometry based model (i.e., from Eqn. 26, 28) lie in the camera image. However, in order to obtain the true coordinates, a relationship is required to establish between a point on the 3D object and a pixel position in the camera image. This process involves a number of geometric parameters also called sensor parameters, since most of parameters relate with optical characteristics, therefore cannot be measured directly. Camera calibration method has been intensively studied in the past and many improvements have been made in recent years [71-72]. A most popular camera calibration theory for photogrammetry and stereo vision was proposed by Zhang and a detailed comparative review of camera calibration methods is described by Salvi et. al. in [73].

The process to obtain the true coordinates can be assumed as rigid-body transformation, perspective projection through pinhole, and radial and tangential distortions. In the rigid-body transformation (rotation plus translation), so called extrinsic parameters and in other processes intrinsic parameters (focal length, principal point, and radial distortion factor) are estimated. When the extrinsic and intrinsic parameters are estimated, the process can be reversed in order to find the object coordinates (X, Y, Z) that correspond to each image pixel (i, j). After that, the estimated parameters are then combined and solved to obtain the desired 3D object coordinates.

2.7 3D Registration and Merging

In order to describe a complete object in 360^{o} view, instead of a single patch, multiple patches are required to be captured. The system which has only one camera, multiple patches are captured from different locations and orientations, and each patch is represented as partially overlapped point cloud data. In order to align all the scanned patches, the surface registration process is performed on different patches with the same coordinate system. Usually, in surface registration, point to point correspondence of the overlapped area is calculated. For this purpose, Iterative Closest Point (ICP) is the most commonly used algorithm [74]. It minimizes the difference between two point clouds using the nearest neighbor search criteria. In this research, we improved the existing 3D registration algorithm for the multi-patches alignment. The registration process involves:

- Curvature calculation at each source point
- Reject irrelevant points
- Recalculate and update point normal
- Check iteration ending criteria
- Comparison of normal vector of source and target surface

After the crucial process of registration, integration of multiple scanned surfaces is required to be performed. This integration process is called Mesh Merging. There can be two types of merging methods in 3D shape measurement which are surface [99-102] and volumetric [103-105] merging. In surface merging method, patches which have been aligned by registration process are merged into one united patch by removing the overlapped regions between patches. In volumetric merging method, regular background grid is constructed and an implicit surface, also called an iso-surface, is extracted by computing the distance map of the background points toward the object surface. In this

voxel based merging, it is necessary to choose an appropriate grid size.

Smaller grid size results in greater detail and dense mesh, but costs greater memory usage, lower frame rates, and greater sensitivity to noise. Larger grid size gives higher frame rates, but the individual splats become more visible. Comparatively, volumetric merging shows good performance than surface merging. However, still there are some weaknesses in the

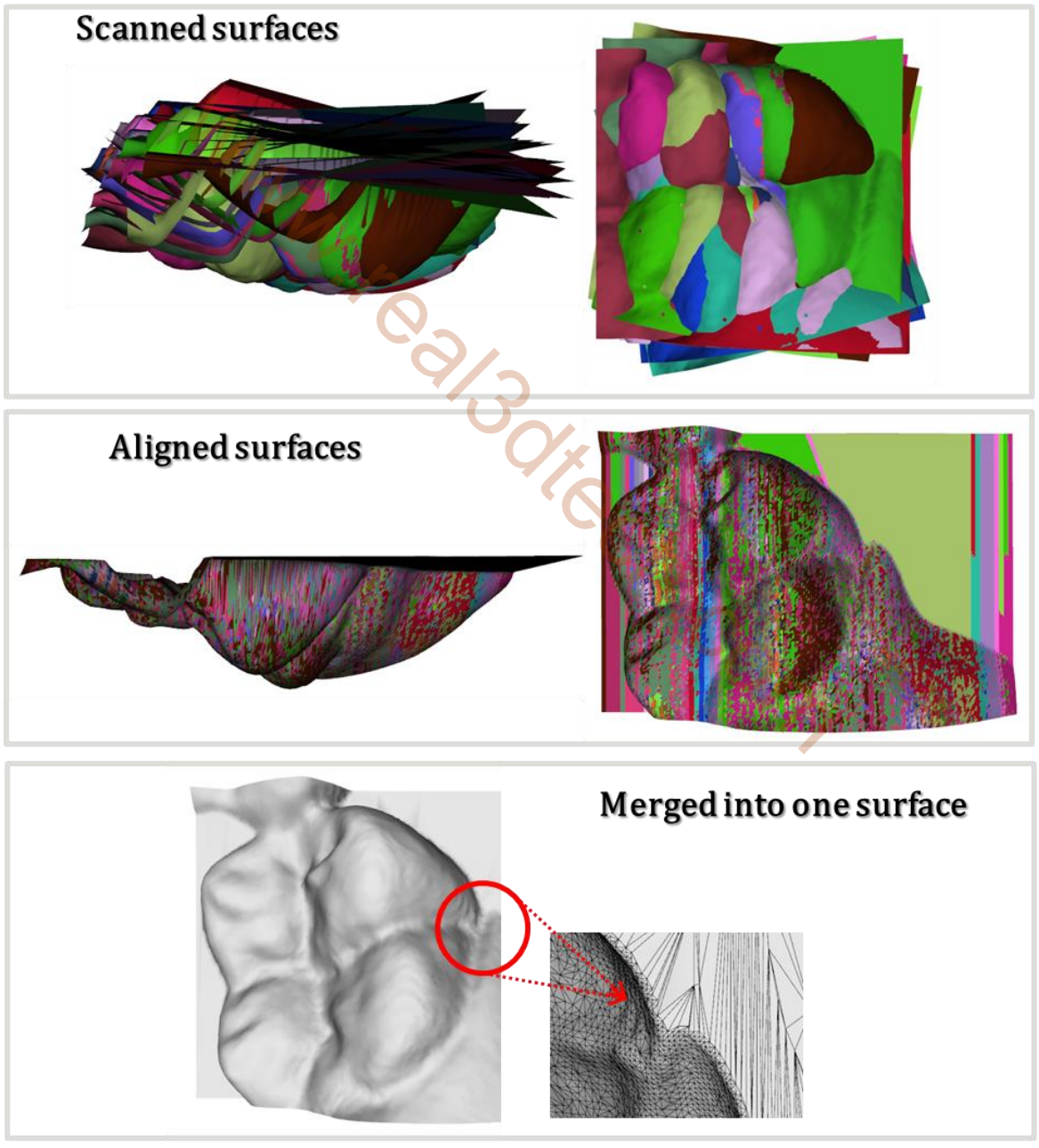

Fig. 12: Registration and merging of twenty eight surface patches in the virtual 3D scanner

volumetric merging that need to be resolved. Fig. 12 demonstrates an example of registration process and volumetric merging, figure shows twenty eight surface patches are aligned using registration algorithm and merged using volumetric merging. The experiments were performed in our proposed real-time virtual 3D scanner.

2.8 Surface Denoising and Smoothing Methods

Smoothing algorithms are important and have a long history in the field of geometry processing. There can be two general goals to perform smoothing algorithms, the first goal is denoising the measured data and second is to design high-quality fair surfaces. Usually, scanned meshes acquired by 3D measurement devices contain high frequency noise. The smoothing algorithms smooth out these artifacts in such a way that the global shape i.e., the low frequency component and specific surface features like sharp edges and corners, is preserved. Numerous research have been done and many algorithms have been proposed such as classical Laplacian filtering [75-76], the mean curvature flow, bilaplacian smoothing flow, and the Taubin approach [77-80]. However, when Laplacian filter applied to a noisy surface, significant shape distortion and surface shrinkage may result in addition to noise removal. In order to overcome the shrinkage problem, a filtering method was proposed by Taubin with positive and negative damping factors. This method shows good results but still has the problem of distortion of sharp features.

An important issue consists of developing robust algorithms for removing noise with minimal damage caused to geometric features. More efficient methods are also proposed, such as non-iterative feature preserving smoothing [81] based on robust statistics, and an adaptation of bilinear filtering to surface meshes [82].

An advanced version of Laplacian smoothing was introduced by Zhihong et. al. [83].

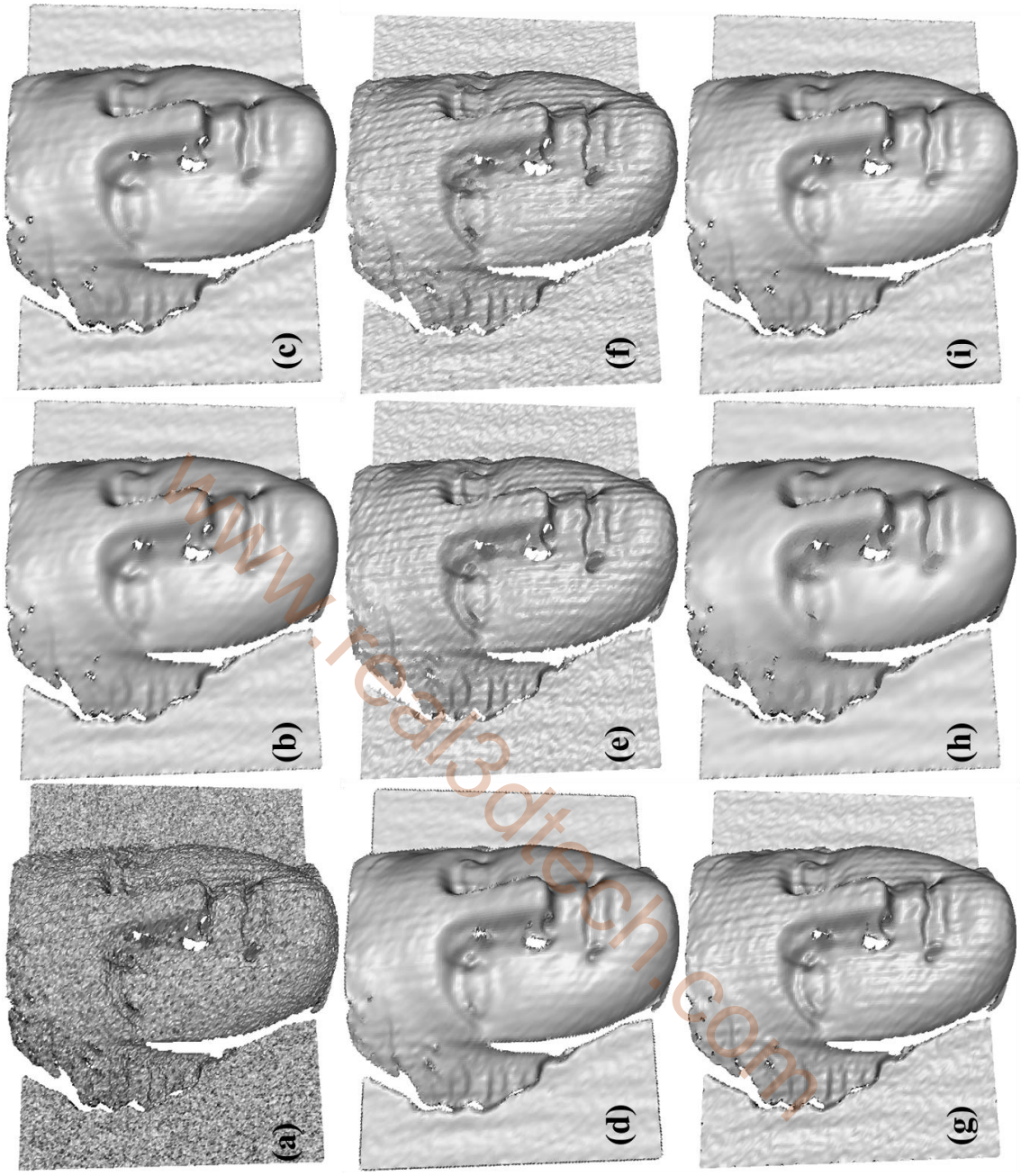

Fig. 13: Comparison results of various smoothing algorithms: (a) shows the reconstructed raw data of a sculpture, (b) gives the result of conventional Laplacian filter with five iterations, (c) presents the result of improved Laplacian smoothing filter with five iterations, (d) depicts the smoothing result of Desbrun's algorithm with five iterations, (e) gives the result of mean filter with fifty iterations, (f) illustrates the result of median filter with fifty iterations, (g) demonstrates the result of the Taubin's filter with ten iterations, (h present the result of two-step fairing algorithm proposed by Belyaev et. al., 2003, and (i) demonstrates the result of SUSAN smoothing.

They extended the SUSAN (smallest univalue segment assimilating nucleus) operator for smoothing noisy 3D shapes approximated by triangle meshes. The main idea of their method is to use the SUSAN operator to robustly remove the outliers in order to obtain a SUSAN area in the neighborhood of each mesh vertex, and then update the mesh vertex position by the so-called umbrella-operator within the SUSAN area.

Some smoothing and fairing filters are implemented with different number of iterations on the reconstructed noisy shape of a sculpture as shown in Fig. 13. The scanned data was acquired by our SMDFP system. Fig. 13 (a) shows the reconstructed raw data of a sculpture, Fig. 13 (b) gives the result of conventional Laplacian filter with five iterations, Fig. 13 (c) presents the result of improved Laplacian smoothing filter with five iterations, Fig. 13 (d) depicts the smoothing result of Desbrun's algorithm with five iterations, Fig. 12 (e) gives the result of mean filter with fifty iterations, Fig. 13 (f) illustrates the result of median filter with fifty iterations, Fig. 13 (g) demonstrates the result of the Taubin's filter with ten iterations, Fig. 13 (h) present the result of two-step fairing algorithm proposed by Belyaev et. al., 2003, and Fig. 13 (i) demonstrates the result of SUSAN smoothing.

2.9 Elimination of Outliers

Outlier can be referenced to points that are out of range and unreliable, long, and thin triangles. In order to perform accurate registration and merging, it is necessary to eliminate outliers before these operations. Outlier algorithm can be operated on point cloud (before triangulation) or on meshes (after triangulation). Some algorithms that work on point clouds and can also be extended to meshes are Range algorithm (it discards out of range points), Statistical removal algorithm (it discards points based to spherical density criteria), Radius outlier algorithm (it discards points based on number of neighbors they have).

Our outlier algorithms operate after triangulation. The adopted elimination criteria are

1. The side angles of a triangle are checked, and if the angle between two edges is less than the predefined threshold angle, that triangle is eliminated. This criterion eliminates all the long and thin triangles.
2. The angle between the face normal of the triangle and projection or view point vector is checked, and if the angle is less than the predefined threshold angle, that triangle is eliminated. This criterion eliminates the wrong oriented or sharp triangles.
3. The number of neighbors of each vertex of a triangle is checked, and if a triangle has less than the predefined threshold number, that triangle is eliminated. This criterion eliminates most of the undesired shells from the mesh.

In all of the above cases, elimination threshold should not be set to be too aggressive. In practice, we currently discard triangles for first and second case in which the smallest angle is less than 10 degrees, and 13 number of neighbors are selected for the third case.

2.10 Summary

Compared with the calibration model, the geometry based models has become more popular because it has more potential to achieve high accurate measurements. Srinivasan et. al. model uses three images with the phase increment of 120^{o} and a mechanical device as a phase shifter which makes this system non-linear, therefore high accurate results become difficult to achieve. On the other hand, phase shifting method with four images with the increment of 90^{o} gives more accurate results; it reduces the inaccurate phase shifts between data frames, more robust against disturbing influences, etc. In order to obtained linear absolute phase map, quality-guided algorithms have many advantages, these algorithms relatively

simple to implement, have low memory overheads, and do not find residues or create branch-cuts. However, the success of this algorithm relies on how good the quality map is. Registration and merging are very important and challenging tasks for any 3D shape measurement system, ICP is the most commonly used algorithm for registration, and comparatively, volumetric merging shows good performance than surface merging.

Chapter 3. Development of a Real-Time Virtual 3D Scanner

This chapter describes the development of a real-time virtual 3D scanner (RTV3DS) that is an ideal platform to verify the capability and performance of the optical scanning methods and systems. In RTV3DS, we created a very similar system model like our 3D IOS, and before finalizing the hardware of the IOS device, we tested the complete scanning procedure that involved in the intraoral scanning.

3.1 Introduction

Real-time virtual 3D scanner is a high resolution DFP technology based virtual scanner that scans virtual or CAD objects in the virtual environment. It performs projection of computer generated fringe patterns onto the virtual 3D object, images capturing, point cloud acquisition, reconstruction, color texturing, and display processes, simultaneously. The virtual system comprises a virtual camera, a virtual projector, and a virtual reference plane. All the virtual parameters can be adjusted according to the real-world 3D shape measurement system. In order to scan a virtual object in real-time, the fringe pattern images are generated by the phase-shifting algorithm, projected onto the virtual object through a virtual projector, the real-time switched images are captured by a virtual camera, and the 3D shape of the object from deformed fringe patterns is then extracted and displayed. All processes are performed instantaneously and quickly in real-time.

The difference between the virtual scanner and the real-world 3D scanner is that the geometric relationship between the camera and the projector is precisely defined in the virtual setup that is extremely difficult in the real-world scanner. Therefore, 3D coordinates acquisition, reconstruction, and display processes become very simplified and precise in the virtual setup. Fig. 14 shows the GUI and setup of the real-time virtual 3d scanner in

which a virtual camera, a virtual projector, a virtual reference plane, and a CAD object are rendered.

3.2 Principle and Theory

The basic principle of the virtual scanning is, first view and light projection matrices are computed, second the texture matrix can be obtained by multiplying the scale-bias matrix with the both known matrices, and finally the texture parameters are adjusted using the texture mapping technique. Once the projected fringe pattern images are captured by the virtual camera, the phase can be obtained by establishing a relationship between 2D image and a 3D object coordinates using a triangulation procedure.

Projective texture mapping (PTM) is a method of texture mapping described in [106] that allows the texture image to be projected onto the object as if by a slide projector. Assume that the texture is being projected onto the object by a slide projector which has most of the same properties that cameras have such as viewing transform that transforms world coordinates into projector space coordinates, and a projection transform that maps the projector view volume to clip coordinates. After that, the scale and bias is applied for a simple range mapping typically [0, 1] for each coordinate.

In order to assign texture coordinates for PTM, OpenGL provides a texture coordinate generation subroutine called *glTexGeni* [107]. It simple generates texture coordinates using the vertex position in eye space with *GL_EYE_LINEAR*. Object and eye linear are two types are commonly useful for PTM. In these types each component of the texture coordinate is computed by evaluating a plane equation at the vertex position. To compute the *eye linear texgen* homogenous matrix M_e in OpenGL, following relation can be utilized.

$$M_e = \begin{bmatrix} 0.5 & 0 & 0 & 0 \\ 0 & 0.5 & 0 & 0 \\ 0 & 0 & 0.5 & 0 \\ 0.5 & 0.5 & 0.5 & 1.0 \end{bmatrix}_{bias\ from[-1,1]to[0,1]} M_l M_v \tag{30}$$

where M_l and M_v are the light projection homogeneous matrix and light view homogenous matrix, respectively.

3.3 Phase Shifting in Virtual Scanner

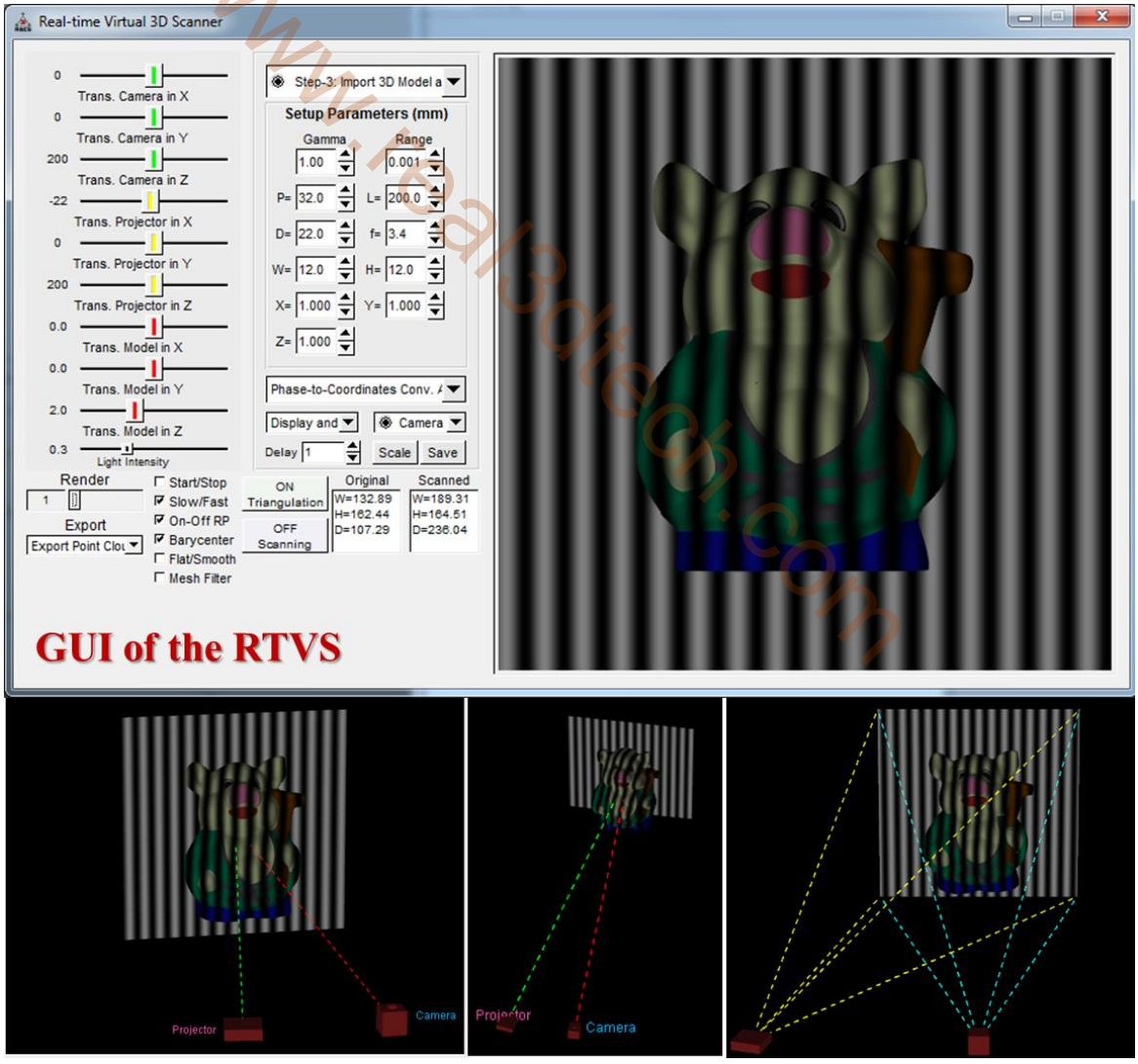

Fig. 14: GUI and views from different angles of the RTV3DS

Due to virtual and digital nature of the fringe patterns, there is no significant effect of phase-shift error on phase-shifting method. The system setup is precisely defined and if we want to analyze different real-world situations, we can easily test and experiment in this setup. For example in case of our 3D IOS: what will happen and what results will be produced if we add noise in the fringe pattern or in the scene, what will be the effect on the reconstructed model if we project rotated fringe patterns, how can we get the same effect on the fringe pattern as the defocused real-world projector, what results can we get if we add lens distortions?, etc. These kinds of fringe analysis help a lot in the improvement of the optical scanning device.

Currently, 3-step, 4-step, and 5-step phase-shifted methods can be simulated in the RTV3DS; however, 6-step, 7-step, 18-step, etc. can also be easily added in the future.

In order to unwrap the wrapped phase map, different algorithms along with residues filters are added and tested in the RTV3DS. Currently, quality-guided, multi-level quality guided, flood-fill, simple linear, and one-dimensional phase unwrapping algorithms are added and other algorithms can be easily added anytime in the future.

3.4 Phase-to-Coordination Conversion

After the continuous phase map is obtained, the coordinates of the points on the object surface must be calculated. Therefore, a conversion is required from the phase map to object's coordinates, which can be done by triangulation method. In this virtual setup, several phase-to-coordinate conversion algorithms can be tested and verified because due to the virtual nature of the system, accurate and precise parameters can be adjusted into the mathematical equations. All four cases which are explained in Chapter 3 are analyzed and

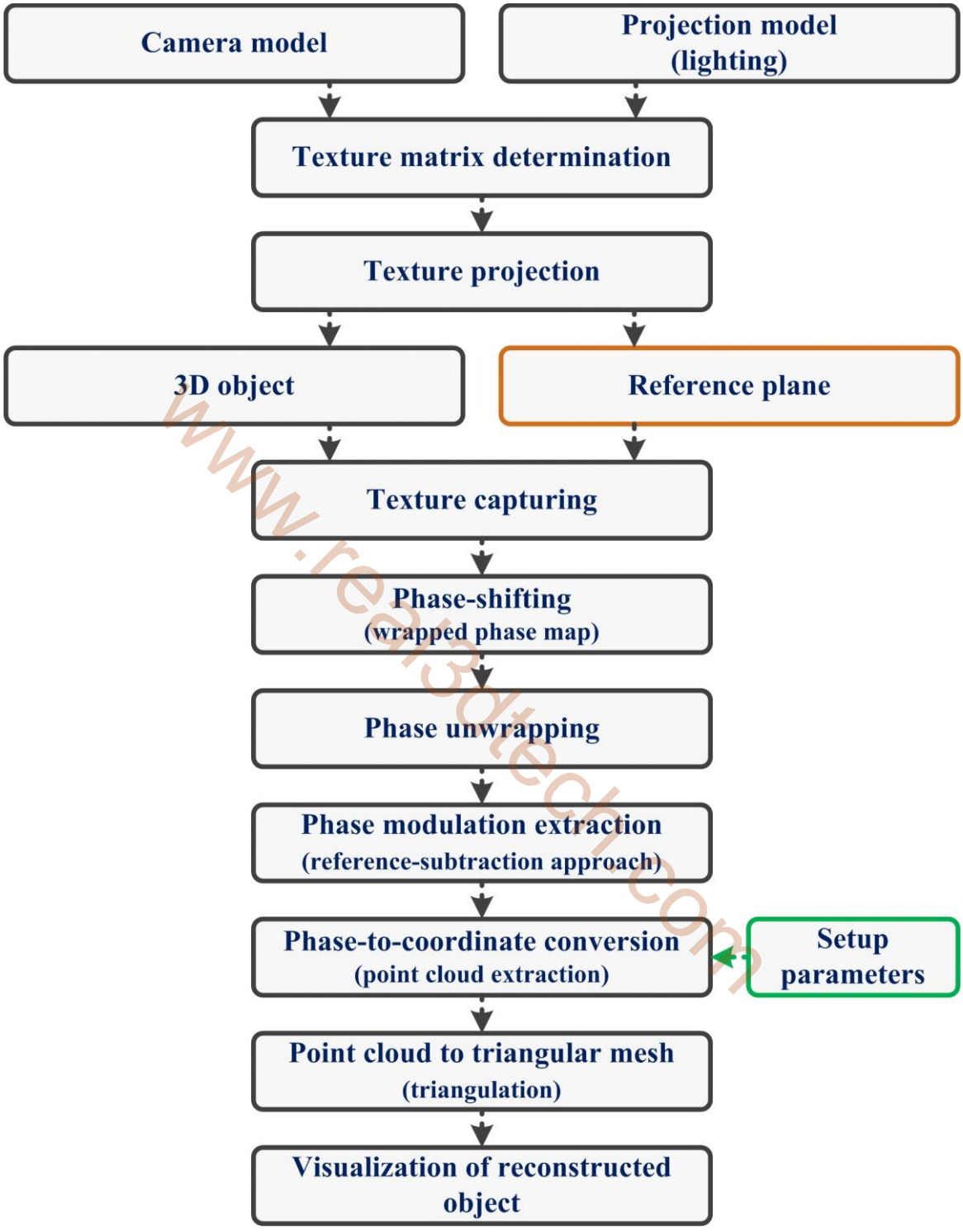

Fig. 15: Virtual system: flow chart of the relationship of algorithms involved in real-time virtual 3D scanner

tested in RTV3DS and results are also presented. Other proposed mathematical models can also be added in the future; however, currently six algorithms can be implemented in real-time.

3.5 Color Texture Acquisition

3D measurement systems are used increasingly to acquire digital models of objects for virtual reality, animation, and ecommerce applications for which the central concerns are efficient representation for interactivity and high visual quality. New techniques were proposed by Fausto et. al. [98] for reconstructing high-quality textures from multiple scans. However, in this dissertation, we focus on the single scan texture capturing and take advantage of pixel-by-pixel phase retrieval using phase-shifting algorithm to realize simultaneous color texture acquisition. Once the wrapped value of the specific pixel is retrieved, we compute the color map simultaneously from the captured color images using the follow equations.

$$C^R(i,j) = \frac{1}{n}\sum_{n=1}^{n} I_n^R(i,j) / I_{factor} \tag{31}$$

$$C^G(i,j) = \frac{1}{n}\sum_{n=1}^{n} I_n^G(i,j) / I_{factor} \tag{32}$$

$$C^B(i,j) = \frac{1}{n}\sum_{n=1}^{n} I_n^B(i,j) / I_{factor} \tag{33}$$

where $C^R, C^{G,}, C^B$ are the red, green, and blue components of the (*i*, *j*) pixel of the color map, respectively, I_n^R, I_n^G, I_n^B are the red, green, and blue components of the (*i*, *j*) pixel of

the n^{th} phase-shifted image, respectively, n is the total number of phase-shifting images, and I_{factor} is the constant intensity factor value which is usually the average intensity 127.5.

3.6 Experiments

The implementation process of the virtual system can be realized in Fig. 15 that presents a flow chart of the relationship of algorithms involved in real-time virtual 3D scanner. Various experimental measurements were conducted to perform the real-time 3D

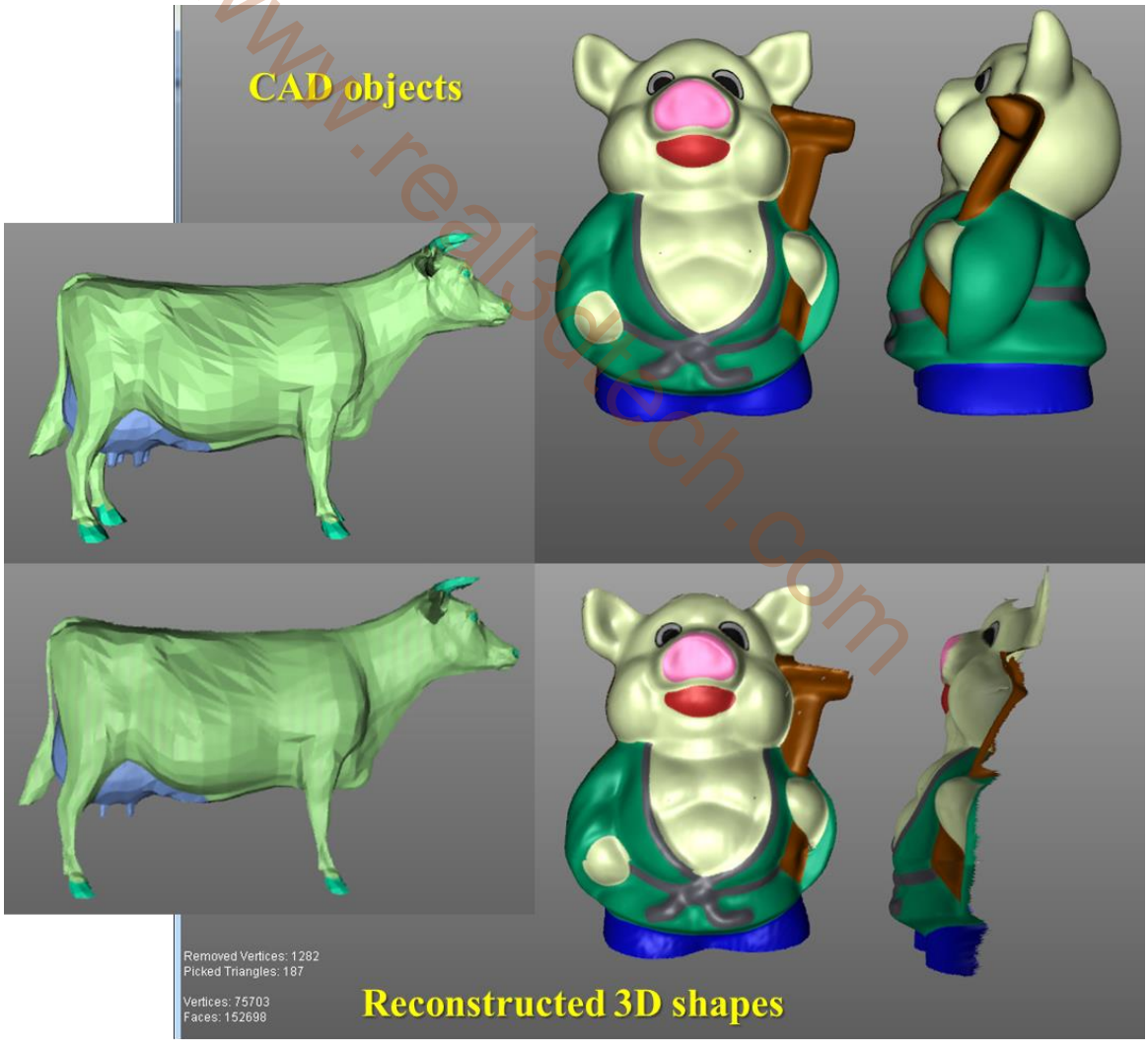

Fig. 16: Virtual measurements: two CAD objects are scanned with texture and color information using the real-time virtual 3D scanner

shape measurements to verify the performance and capability of the used algorithms in the development of IOS device. The 3D measurement results of many shapes using the developed RTV3DS and some of the methods that are discussed in this dissertation are shown in Fig. 16-18. All the illustrations demonstrate reconstructed shapes of CAD objects with and without color texture.

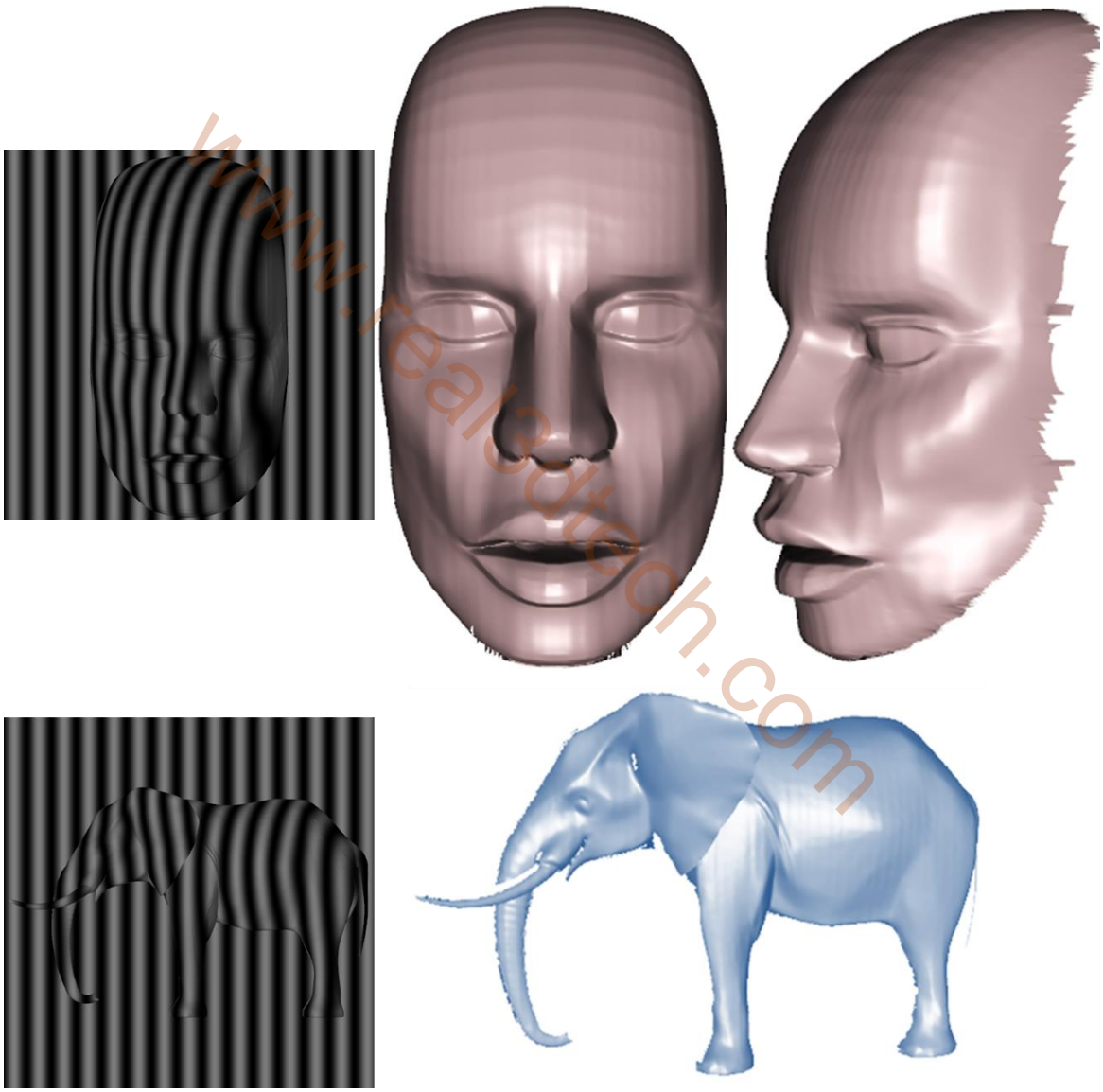

Fig. 17: Virtual measurements: fringe patterns onto the CAD objects and reconstructed 3D shapes. (The lines or specific patterns onto the above shape are from the CAD object not from the scanned data.)

Fig. 18: Virtual measurements: Cad objects with reference planes (before patterns projection), fringe patterns onto the CAD objects (after patterns projection), and reconstructed 3D shapes

3.7 Summary

The virtual 3D scanner that presented in this chapter will be very effective in the future development, and performance and comparison analysis of new 3D shape measurement systems. RTV3DS is a high resolution DFP technology based virtual scanner that scans virtual/CAD objects in the virtual environment. Currently, 3-step, 4-step, and 5-step phase-shifted methods can be simulated in the RTV3DS; however, 6-step, 7-step, and 11-step, can also be easily added in the future in order to achieve more accurate results.

Chapter 4. Analysis and performance comparison of Mathematical 3D Scanning System Models

Practically, there is not a specific optical system model for SMFP system, but the system setup can be represented in four ways. In this chapter, four geometric models of SMFP system are evaluated based on collimating and non-collimating (perspective) projections. Analysis and performance comparison of the phase-to-coordinate relation for all four models is presented. Two nonlinear system models are proposed to obtain the accurate 3D shape for collimating illumination based systems. Finally, the results are presented and chosen the best configuration for the IOS device.

4.1 Introduction

In fringe projection technique, the fringe pattern is projected onto the object and obtained the height of an object from deformed fringe image, which is modulated by the object surface. However, there is not a specific optical system setup for projecting and capturing the fringe patterns, but the system setup can be represented in four cases.

- **Case-1:** The camera is aligned with the axis of the object and a perspective projector projects fringe patterns onto the object by having some distance from the optical axis of the camera.
- **Case-2:** The perspective projector is aligned with the axis of the object and a camera captures deformed fringe pattern images by having some distance from the optical axis of the projector.
- **Case-3:** The collimating illuminative device (i. e., LED, laser) is aligned with the axis of the object and a camera captures the deformed fringe strips by having some distance

from the optical axis of the illuminating device.

- **Case-4:** The camera is aligned with the axis of the object and a collimating illuminative device projects the series of parallel fringe strips onto the object by having some distance from the optical axis of the camera.

In this dissertation, all four cases are examined and evaluated by using our proposed real-time virtual 3D scanner which is very similar to the real-world fringe projection based 3D shape measurement system. In the virtual scanner, accurate system parameters can be easily determined that are difficult to obtain by direct measurements. These parameters are required by the phase-to-coordinate conversion algorithm for the calculation of the object coordinates. A number of techniques have been proposed for reconstruction of 3D shape using the perspective projection [1]. On the other hand, use of collimating illumination results in a phase map that is different from the use of perspective projection due to the change in pitch of the projected pattern onto the object, thus different dimensional information of the object. Furthermore, when the imaging index is not aligned with the axis of the object then the relationship between (X, Y) coordinates of the object and the imaging index (i, j) becomes nonlinear. Therefore, we cannot implement the same mathematical model on all mentioned cases. Therefore, rigorous models are required to acquire the accurate dimensional information of an object for the perspective projection as well as for the collimating illumination cases. This dissertation proposed new system models for 3rd and 4th cases in order to convert the phase map to accurate X, Y, and Z coordinates of the object.

The wrapped phase map is obtained using the 4-step phase-shifting algorithm and unwrap it using a quality-guided phase unwrapping algorithm. After the continuous phase map is obtained, the coordinates of points on the object surface must be calculated. Therefore, a

conversion is required from the phase map to object's coordinates. As described earlier, there can be four cases to represent the 3D shape measurement system for the reconstruction of 3D shape from the obtained phase map. The mathematical models of four cases are described below.

4.2 Geometric Models

4.2.1 Case - 1

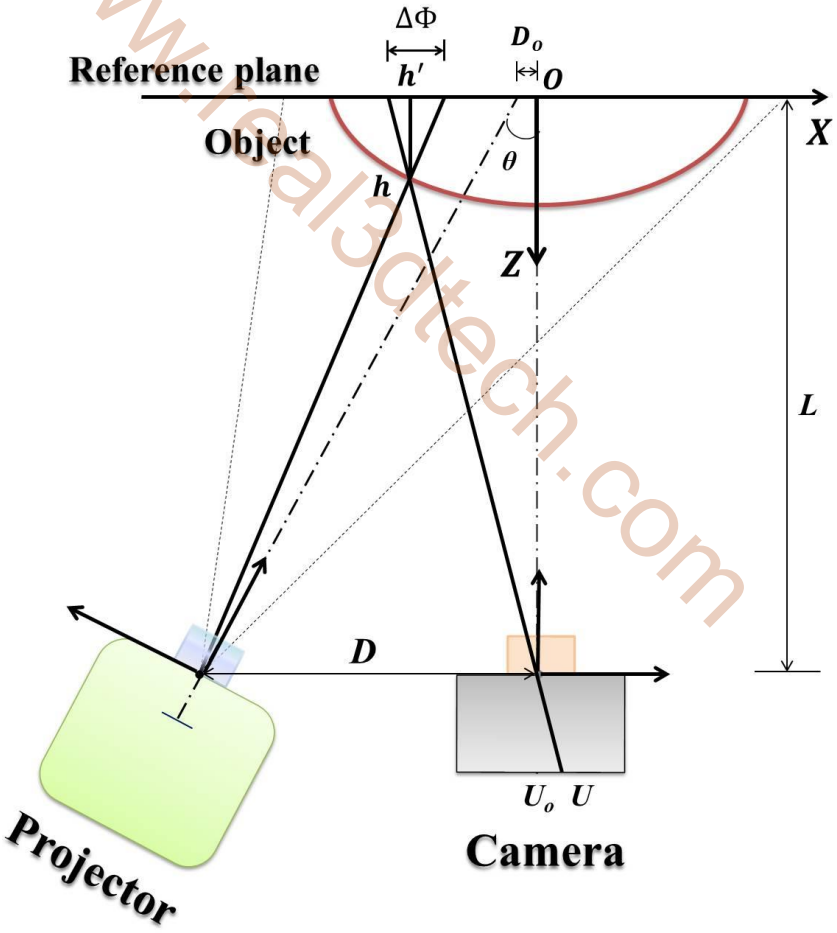

Fig. 19: Phase-to-coordinate conversion: optical geometry of Case-1 for coordinates calculation

In the system model of Case-1, the camera is aligned with the axis of the object and a perspective projector projects phase-shifted fringe patterns onto the object by having distance D from the optical axis of the camera. Fig. 19 illustrates the optical schematic diagram of Case-1 for phase-to-coordinate conversion. The diagram shows the optical geometry relationship of camera and projector corresponding to the reference plane coordinate system. The equation governing the height calculation of the object is written as:

$$Z_h = \overline{hh'} = \frac{\Delta\Phi}{sin\theta} \tag{34}$$

where Z_h is the height profile of the object. From the optical geometry, the corresponding angle θ can be determined by:

$$\theta = \tan^{-1}\left(\frac{D - D_o}{L}\right) \tag{35}$$

where D represents the distance between the entrance pupil of the camera and the exit pupil of the projector, L is the working distance between the reference plane and the origins of camera and projector. It is important to mention here that, in reality, it is approximately impossible to make D_o = 0 (zero) which is the distance between the optical axes of camera and projector on the reference plane. However, it will be assumed to zero in the virtual simulation because the both optical axes of the camera and the projector intersect at O. ΔΦ is the measured phase depth that can be obtained by reference-subtraction approach. Assume the spatial period of the fringe pattern projected on the reference plane is P then ΔΦ can be expressed as follows:

$$\Delta\Phi = \frac{P}{2\pi}\left[\Phi_{obj}(i,j) - \Phi_{ref}(i,j)\right] \tag{36}$$

where Φ_{obj} and Φ_{ref} represent the unwrapped phase maps of an object and reference plane,

respectively. Because the origin of the object's coordinate system is aligned with the origin of the reference plane and the camera, the (X, Y) coordinates of the object can be considered proportional to the imaging index (i, j). Thus the X coordinate of point h can be expressed by:

$$X_h = (U - U_o)\delta \tag{37}$$

and

$$\delta = \frac{W_{screen}}{W_{image}} \tag{38}$$

where U is the any arbitrary image pixel in the horizontal direction, U_o is the origin of the image, W_{screen} is the width of the reference plane in millimeters and W_{image} is the total number of image pixels in the horizontal direction. Similarly, the y coordinate of point h can be written as:

$$Y_h = (V - V_o)\delta' \tag{39}$$

and

$$\delta' = \frac{H_{screen}}{H_{image}} \tag{40}$$

where V is the image pixel in the vertical direction, V_o is the origin of the image, H_{screen} is the height of the reference plane in millimeters, and H_{image} is the total number of image pixels in the vertical direction. Assume the number of image pixels is the same in both horizontal and vertical directions then δ' = δ.

Due to the proportionality of the imaging index (i, j) and the object coordinates (X, Y) of this system model, the geometric relationship to retrieve the height of the object can also be expressed as:

$$Z_h(x,y) = a\left(\Delta\Phi(x,y)\right)^2 + b\left(\Delta\Phi(x,y)\right) + c \tag{41}$$

and

$$Z_h(x,y) = K(x,y)\Delta\Phi(x,y) \tag{42}$$

where a, b, c are the fit parameters and K is the calibration constant for that specific pixel.

4.2.2 Case - 2

In the system model of Case-2, the perspective projector is aligned with the axis of the object and a camera captures the deformed phase-shift fringe pattern images by having distance D from the optical axis of the projector. The optical geometry of Case-2 for phase-to-coordinate conversion is demonstrated in Fig. 20. From the geometry diagram, the object height $\overline{hh'}$ can be calculated using triangulation method. Since, Δ O_PO_ch and Δ hAB are similar, we have:

$$\frac{\overline{O_cO_P}}{\overline{hO_P}} = \frac{\overline{AB}}{\overline{hh'}} \tag{43}$$

$$\frac{D}{L-\overline{hh'}} = \frac{\Delta\Phi}{\overline{hh'}} \tag{44}$$

Thus, the height of the object $\overline{hh'}$ with respect to the reference plane can be written as:

$$Z_h = \overline{hh'} = \frac{L\Delta\Phi}{D+\Delta\Phi} \tag{45}$$

where ΔΦ is the phase depth and can be determined by Eq. 36. As discussed earlier, when the imaging axis is not aligned with the axis of the object, then the captured imaging index (i, j) are no longer proportional to (X, Y) coordinates of the object. Therefore, it is required to calculate the (X, Y) coordinates according to the imaging index (i, j). The X coordinate of the object at A can be written as:

$$X_A = \frac{P}{2\pi}(\Phi_A - \Phi_O) \tag{46}$$

where Φ_A is the unwrapped phase map of the object at point *A* and Φ_O is the unwrapped phase map of the reference plane at point *O*. Since, ΔOO_PA and $\Delta h'hA$ are similar in Fig. 14, we have:

$$\frac{X_A}{L} = \frac{X_A - X_h}{Z_h} \tag{47}$$

Thus, the *X* coordinate of point *h* can be written as:

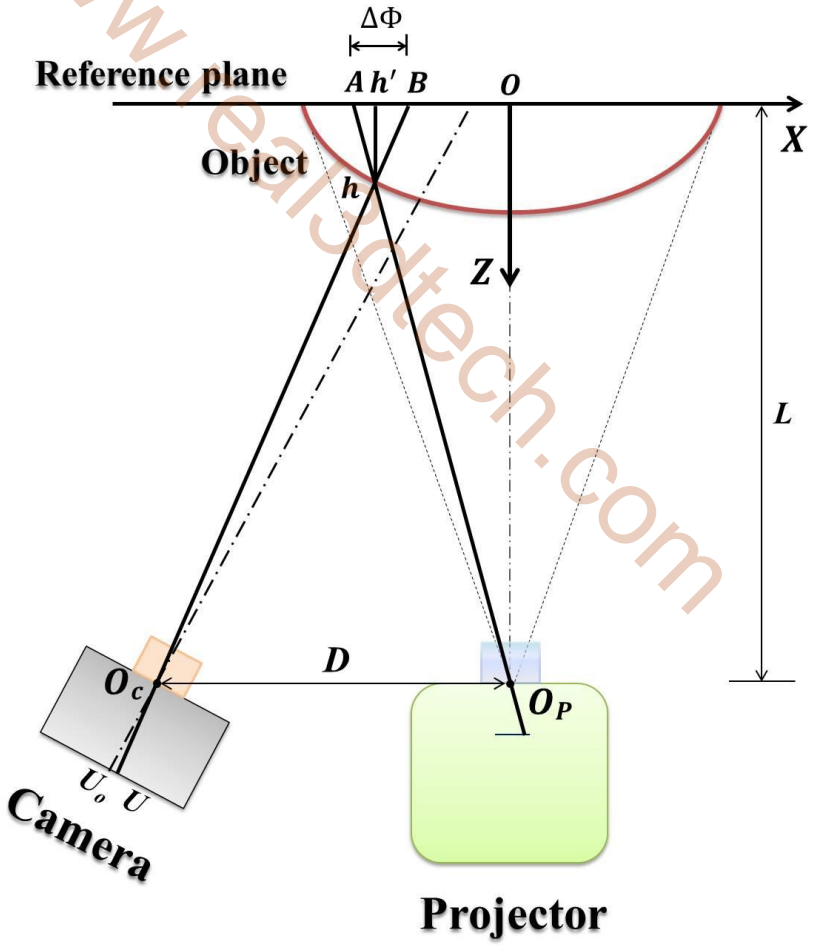

Fig. 20: Phase-to-coordinate conversion: optical geometry of Case-2 for coordinates calculation

$$X_h = X_A\left[1-\frac{Z_h}{L}\right] \tag{48}$$

Since, the vertical fringe patterns are projected onto the object, therefore, the height of the object is independent of the Y_h coordinate. However, Eq. (39) can be used to obtain Y coordinate of the object.

4.2.3 Case - 3

This optical system model is very similar to Case-2 but with the difference of light source. According to system model of Case-3, the collimating illuminative device (usually a laser or LED light source) is aligned with the axis of the object and a camera captures the deformed fringe strips by having distance D from the optical axis of the illuminating device. Since, the system uses collimating illumination, however, the use of collimating illumination results in a phase map that is different than the use of non-collimating projection due to the change in pitch of the projected pattern onto the object, thus different dimensional information of the object. In collimating illumination, the pitch of the strip pattern remains constant despite the distance to the projection unit. It also is believed that when the camera axis does not align with the axis of the object as shown in Fig. 21 which shows the optical geometry of the system for phase-to-coordinate conversion, in this case, the (X, Y) coordinates are not proportional to the imagining index (i, j). Therefore, in order to obtain the accurate 3D shape for this case, a more precise method is required. In the research work of this dissertation, a new nonlinear approach is proposed for Case-3 to obtain the accurate 3D coordinates of the object. The mathematical model for Case-3 is described below.

The laser coordinate system (O_L-X_L, Y_L, Z_L) and camera coordinate system (O_c-X_c, Y_c, Z_c) have origins at the lens O_L and the camera O_c, respectively. The object coordinate system (O-X, Y, Z) located at the intersection point of the laser optical axis and the reference plane. The axes Z_c and Z_L coincide with the optical axes of the camera and laser, respectively, with Y_L parallel to Y, and with Z_L perpendicular to the reference plane. Let us consider a point h on the object profile whose coordinates are (X_h, Y_h, Z_h) with respect to the object

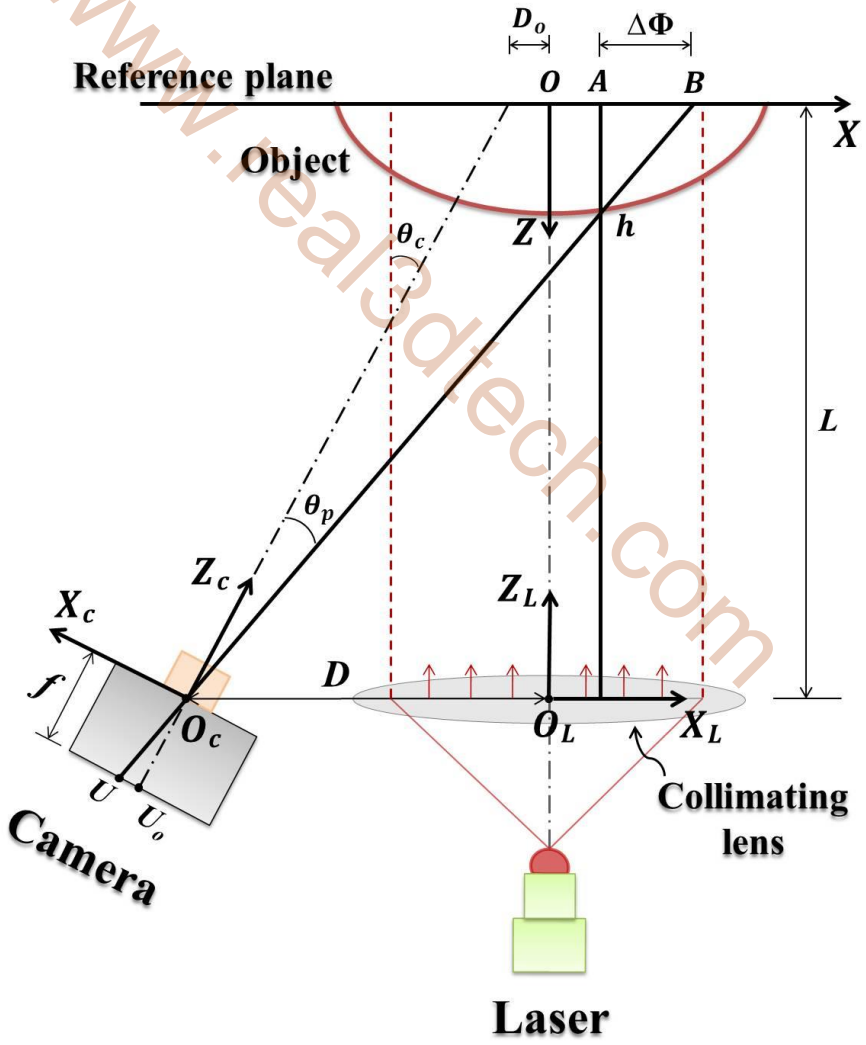

Fig. 21: Phase-to-coordinate conversion: optical geometry of Case-3 for coordinates calculation

coordinate system. With these coordinate systems, the object height is given by:

$$\overline{Ah} = \frac{\Delta\Phi}{\tan(\theta_c + \theta_p)} \tag{49}$$

where $\overline{Ah}$ is the height profile of the object. From the optical setup, the corresponding angles θ_c and θ_p can also be determined for any arbitrary pixel U. These measured angles are related to the optical system parameters as follows:

$$\tan\theta_P = \left(\frac{U - U_o}{f}\right) \tag{50}$$

and

$$\tan\theta_c = \left(\frac{D - D_o}{L}\right) \tag{51}$$

therefore,

$$\tan\left(\theta_c + \theta_p\right) = \left[\frac{L(U - U_o) + f(D - D_o)}{f\,L - (U - U_o)(D - D_o)}\right] \tag{52}$$

where D is the working distance between the origins of the camera coordinate system and the laser coordinate system, D_o is the distance between the optical axes of the camera and laser on the reference plane, L is the working distance between the reference plane and the origins of the camera and laser, f is the focal length of the camera lens, and $\Delta\Phi$ is the measured phase depth that can be obtained by Eq. 36. Finally, the height $\overline{Ah}$ with respect to the reference plane can be written as:

$$Z_h = \overline{Ah} = \Delta\Phi\left[\frac{f\,L - (U - U_o)(D - D_o)}{L(U - U_o) + f(D - D_o)}\right] \tag{53}$$

After determination of Z_h, the calculation for X_h and Y_h for Case-3 is described below.

Since the vertical fringe patterns are projected onto the object, the height of the object is

independent of the Y_h coordinate. Also if the optical axis of the light source is perpendicular to the reference plane in the perspective projection system, then the determination of X_h is greatly simplified. However, in this system model, we are using the same concept of the perspective projection and have developed a geometric relationship for the collimating projection system. Fig. 22 demonstrates the optical geometry relationship to calculate the X coordinate of points h and h' using the collimating projection.

Let Φ_O, $\Phi_{A'}$, and Φ_A represent the unwrapped phase maps at point *O*, *A'*, and *A*, respectively. From Fig. 22, $X_{A'}$ can be determined by:

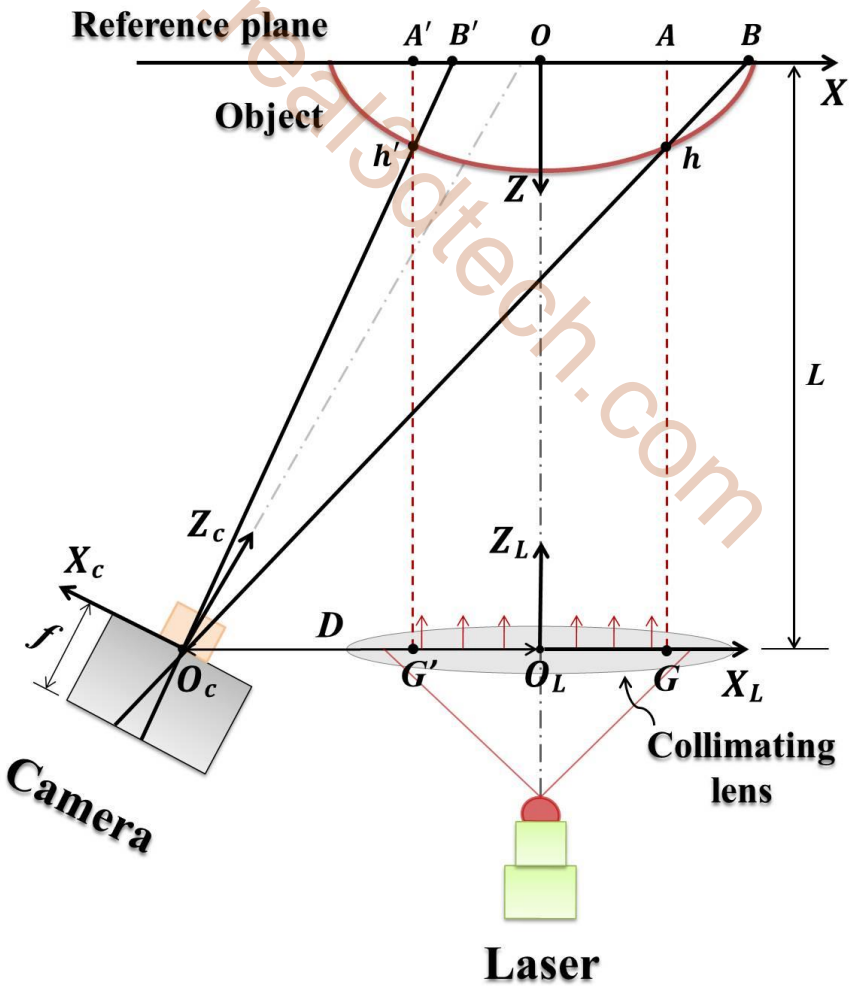

Fig. 22: Phase-to-coordinate conversion: Case-3: geometric diagram to evaluate X_h

$$X_{A'} = \frac{P_R}{2\pi}\left[\Phi_{A'} - \Phi_O\right] \tag{54}$$

where P_R is the pitch of captured phase-shift fringe patterns when X is negative. Since, Δ $h'G'O_c$ and Δ $h'A'B'$ are similar, we have:

$$\frac{\overline{O_cG'}}{\overline{G'A'} - \overline{h'A'}} = \frac{\overline{A'B'}}{\overline{h'A'}} \tag{55}$$

and

$$\frac{D - X_{A'}}{L - Z_h} = \frac{\overline{A'B'}}{Z_h} \tag{56}$$

thus

$$\overline{A'B'} = Z_h\left[\frac{D - X_{A'}}{L - Z_h}\right] \tag{57}$$

where $\overline{A'B'}$ is the calculated phase depth. Now, the difference between measured and calculated phase depths can be written as:

$$\varepsilon_R = \Delta\Phi - \overline{A'B'} \tag{58}$$

Thus, the accurate X coordinate of point h' can be expressed by:

$$X_{h'} = \frac{P}{2\pi}\left[\left(\Phi_{h'} + \varepsilon_R\right) - \Phi_O\right] \tag{59}$$

A similar procedure is followed to evaluate X_h when X is positive. Assume P_L is the pitch of the captured phase-shift fringe patterns when X is positive. Then

$$X_A = \frac{P_L}{2\pi}\left[\Phi_A - \Phi_O\right] \tag{60}$$

Since, Δ hGO_c and Δ hAB are similar, we have:

$$\frac{\overline{O_c G}}{\overline{GA} - \overline{hA}} = \frac{\overline{AB}}{\overline{hA}} \tag{61}$$

and

$$\overline{AB} = Z_h \left[\frac{D + X_A}{L - Z_h} \right] \tag{62}$$

Finally, the X_h coordinate when X is positive can be obtained by

$$\varepsilon_{R'} = \Delta\Phi - \overline{AB} \tag{63}$$

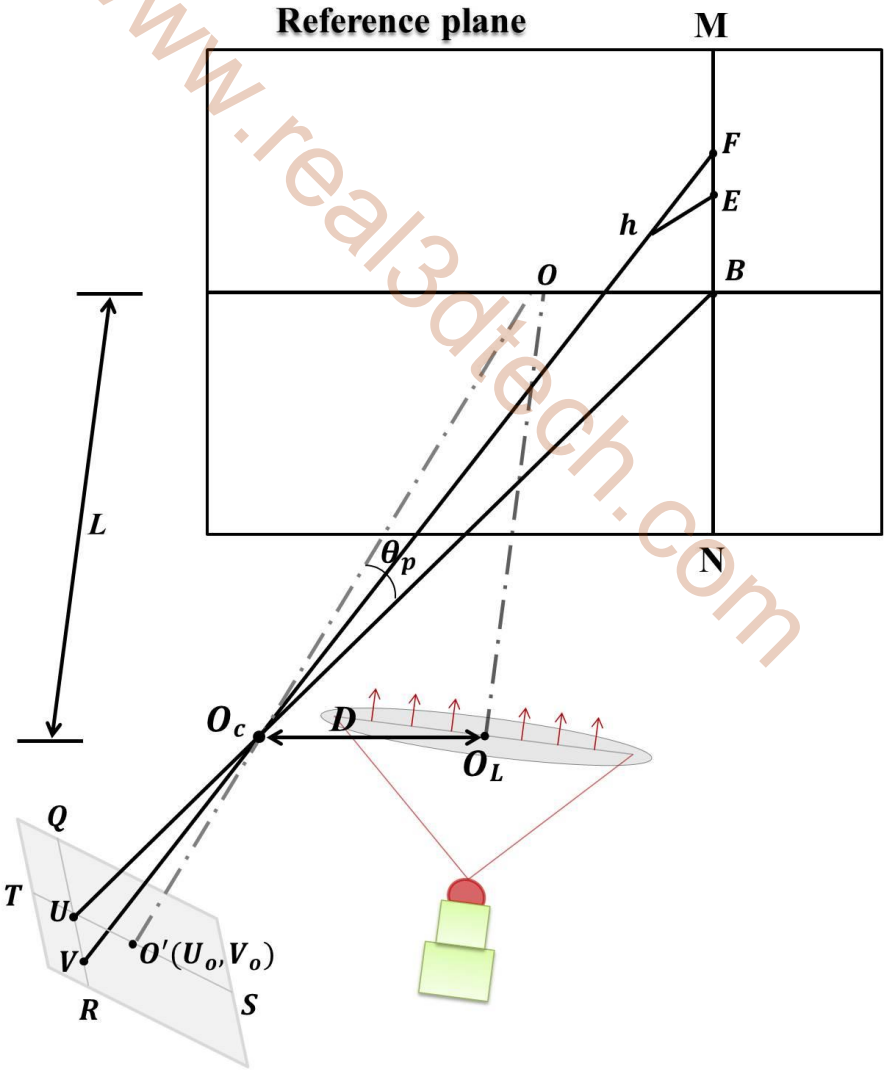

Fig. 23: Phase-to-coordinate conversion: Case-3: geometric diagram to evaluate Y_h

$$X_h = \frac{P}{2\pi}\left[\left(\Phi_h + \varepsilon_{R'}\right) - \Phi_O\right] \tag{64}$$

Fig. 23 demonstrates the optical geometric diagram of the system to evaluate Y_h. Since, the pixel columns are parallel to the Y-axis, the variant viewing width remains constant for pixels in the same pixel column. $\overline{QR}$ is the pixel column indexed by j and $\overline{ST}$ is the pixel column indexed by i. The arbitrary image pixels in the horizontal and vertical directions are denoted by U and V respectively, and $O'(U_o, V_o)$ is the origin of the image. The angle between the optical axes of the camera and the laser is θ_c, and the angle between O_cO and O_cB' is θ_p. Then, from the geometric relation of Fig. 23, $\Delta\, O_cVU$ and $\Delta\, O_cFB$ are similar, and we have:

$$\frac{\overline{VU}}{\overline{O_cU}} = \frac{\overline{FB}}{\overline{O_cB}} \tag{65}$$

and

$$\overline{O_cU} = \frac{\overline{O_cO'}}{\cos\theta_p} = \frac{f}{\cos\theta_p} \tag{66}$$

$$\overline{VU} = V - V_o \tag{67}$$

$$\overline{O_cB} = \frac{L}{\cos(\theta_c + \theta_p)} \tag{68}$$

Thus, Y_F can be expressed as:

$$Y_F = \overline{FB} = \frac{L(V - V_o)\cos\theta_p}{f\cos(\theta_c + \theta_p)} \tag{69}$$

However, $\overline{Ah}$ is perpendicular to the reference plane and $\overline{hG}$ is perpendicular to $\overline{MN}$, so h has the same Y coordinate at point E. Since, $\Delta\, O_cFB$ and $\Delta\, hFE$ are similar, we have:

$$\frac{\overline{FE}}{\overline{hE}} = \frac{\overline{FB}}{\overline{O_c B}} \tag{70}$$

$$\overline{FE} = \left[\frac{Z_h}{L}\right]\overline{FB} \tag{71}$$

Finally, Y_h can be determined by:

$$Y_h = \overline{EB} = \overline{FB} - \overline{FE} = Y_F\left(1 - \frac{Z_h}{L}\right) \tag{72}$$

3.2.4 Case - 4

The system model of Case-4 is very similar to the system model of Case-1 but with the difference of light source. In this case, the camera is aligned with the axis of the object and a collimating illuminative device projects the series of parallel fringe strips onto the object by having distance D from the optical axis of the camera. Fig. 24 depicts the optical geometry diagram for phase-to-coordinate conversion.

The laser coordinate system (O_L-X_L, Y_L, Z_L) and camera coordinate system (O_c-X_c, Y_c, Z_c) are located at the lens O_L and O_c, respectively. The object coordinate system (O-X, Y, Z) located at the intersection point of the camera optical axis and the reference plane. With these coordinate systems, the object height at the point h is given by Eq. 34.

Due to collimating illumination, a rigorous model was required to acquire the accurate dimensional information of the object for this case. In the research work of this dissertation, a new model is proposed for Case-4 to determine the X_h coordinate. Since, vertical fringe patterns are utilized, therefore, Z_h is independent of the Y_h coordinate and the calculation for X_h is described below:

Let Φ_O and Φ_B represent the unwrapped phase maps at point O and B, respectively, and if $X=(U - U_o)\delta$ where δ is the conversion factor from pixels to millimeters then X_B can be

determined by:

$$X_B = \frac{P_R}{2\pi}\left[\Phi_B - \Phi_O\right] \tag{73}$$

where P_R is the pitch of captured phase-shift fringe patterns when X is negative. Since, Δ $hh''O_c$ and Δ $Ah'h$ are similar in Fig. 18, we have:

$$\overline{Ah'} = \frac{\overline{hh''}\,\overline{hh'}}{\overline{OO_c} - \overline{Oh''}} \tag{74}$$

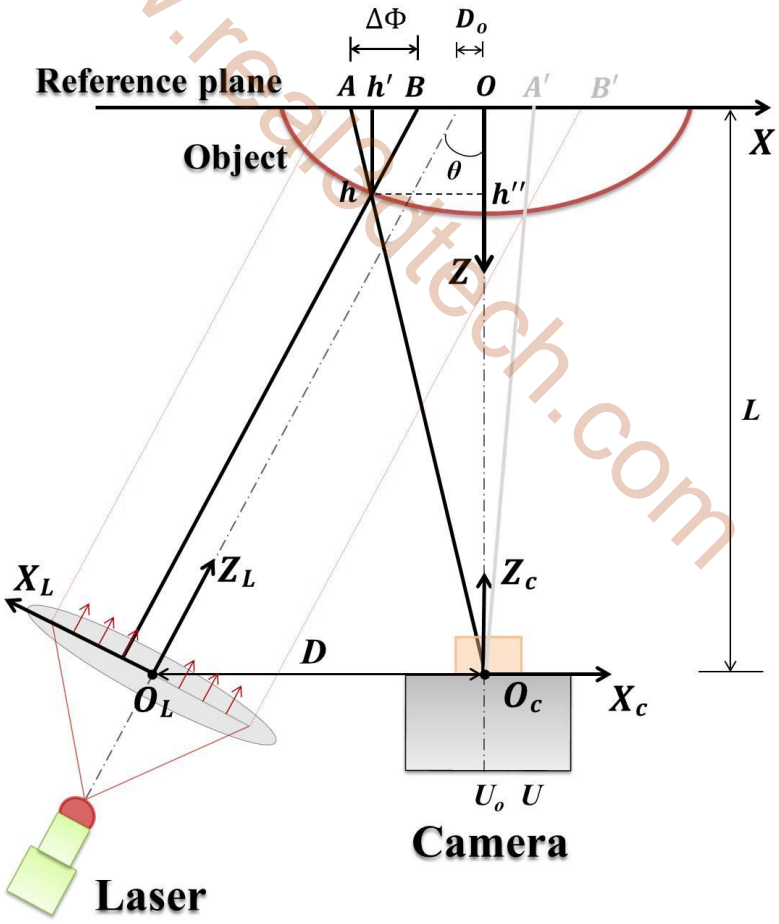

Fig. 24: Phase-to-coordinate conversion: Optical geometry of Case-4 for coordinates calculation

and

$$\overline{h'B} = \overline{hh'}\tan\theta \tag{75}$$

Thus the calculated phase depth $\overline{AB}$ can be determined by:

$$\overline{AB} = \overline{Ah'} + \overline{h'B} \tag{76}$$

Substitute Eqs. (74) and (75) into Eq. (76), we have:

$$\overline{AB} = Z_h\left[\frac{X_B}{L - Z_h} + \tan\theta\right] \tag{77}$$

Now, the difference between measured and calculated phase depths can be written as follow:

$$\varepsilon_R = \Delta\Phi - \overline{AB} \tag{78}$$

where $\Delta\Phi$ is the measured phase depth that can be obtained by Eq. 36. Thus, the accurate X coordinate of point h when X is negative can be expressed by:

$$X_h = \frac{P}{2\pi}\left[\left(\Phi_B + \varepsilon_R\right) - \Phi_O\right] \tag{79}$$

The similar procedure is followed to evaluate the X_h coordinate when X is positive. For that case, the calculated phase depth $\overline{A'B'}$ can be determined by:

$$\overline{A'B'} = Z_h\left[\tan\theta - \frac{X_B}{L - Z_h}\right] \tag{80}$$

4.3 Verification using Computer Simulation

Many simulations in our proposed real-time virtual 3D scanner have been carried out to show the accuracy and effectiveness of all described cases. In our simulation, a half sphere

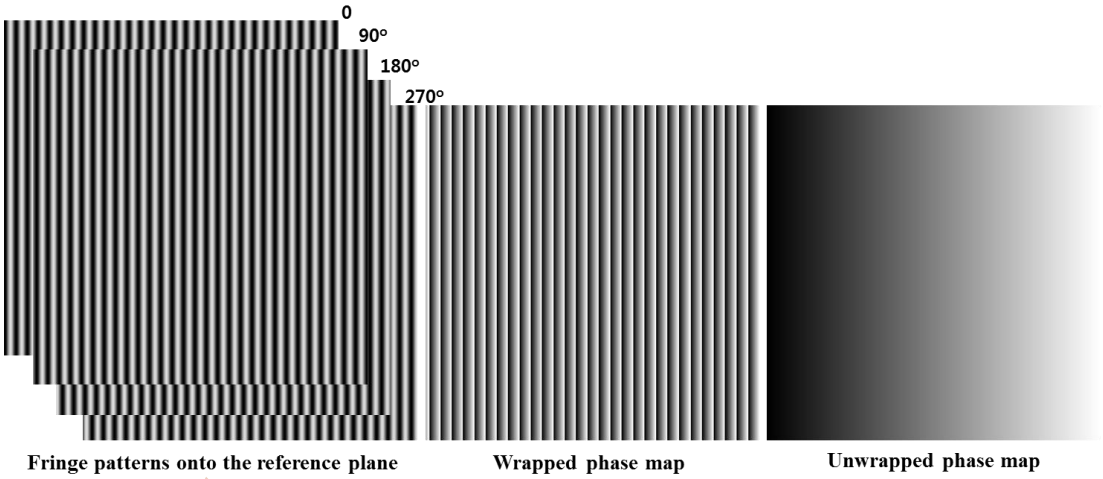

Fig. 25: Computer simulation: (left) 4-step phase shifted fringe patterns onto the plane, (middle) wrapped phase map, (right) unwrapped phase maps

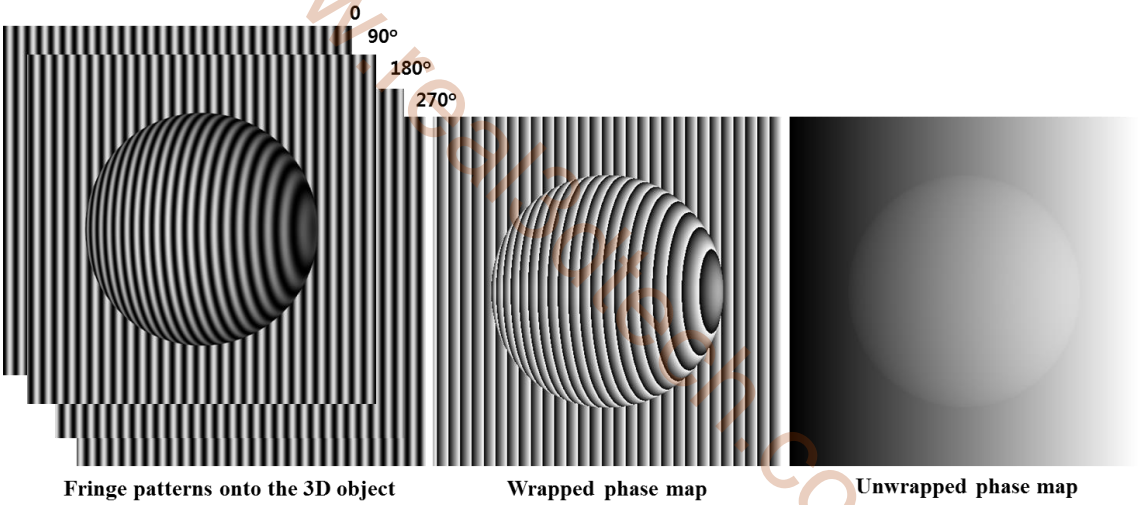

Fig. 26: Computer simulation: (left) 4-step phase shifted fringe patterns onto a half sphere with 4 mm radius, (middle) wrapped phase map, (right) unwrapped phase maps

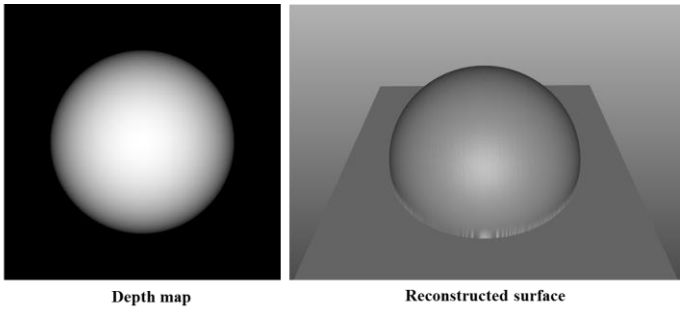

Fig. 27: Computer simulation: (left) depth map extracted from unwrapped phase maps of Fig. 19 and 20 using reference subtraction approach, (right) reconstructed surface from the depth map

with 4 mm radius is adopted, and the resulting parameters are, image size is 512×512 pixels, L=200 mm, D=30 mm, D_o=0 (because of virtual nature), f=973 pixels, P=0.438 mm, P_R=0.137 mm, and P_L=0.356 mm. All the virtual parameters are adjusted according to the real-world 3D scanning system. In order to scan a virtual object in real-time, the fringe pattern images are generated by the 4-step phase-shifting algorithm, projected onto the object through a virtual projector, the real-time switched images are captured by a virtual camera, and the 3D shape of the object from deformed fringe patterns is then extracted and displayed. All processes are performed instantaneously in real-time. It is also important to note here that the captured phase-shift fringe pattern images must be anti-aliased in the virtual environment for the accurate unwrapped phase map. Therefore, to obtain anti-aliased images, multisampling texture technique was utilized. Furthermore, Fig. 25 illustrates the 4-step phase shifted images and wrapped and unwrapped phase maps of the virtual reference plane, Fig. 26 demonstrates four computer generated fringe patterns projected onto the half sphere, and the wrapped and unwrapped phase maps, the phase difference or phase depth which is extracted from reference and object unwrapped phase maps using reference-subtraction approach and reconstructed surface can be seen in Fig. 27.

First various experiments were conducted to verify the accuracy of Case-1. The cross-sections of the reconstructed 3D half sphere and the graphical comparisons between the theoretical and the measured one can be observed in Fig. 28(a) and (c), respectively. For this case, the unwrapped phase map is considered to be proportional to the 3D shape. The root mean square (RMS) difference was 0.001 mm that is negligible. The second of Case-2 was implemented, and results are shown in Fig. 28(b) and (d) and RMS difference was found to be 0.0015 mm. Since, the Case-1 and Case-2 use non-collimating projections,

the determination of an object coordinates was greatly simplified, and the obtained results were satisfactory. On the other hand, if we use the same mathematical models of Case-1 and Case-2 over Case-4 and Case-3, respectively, the results are demonstrated in Fig. 29. Fig. 29(a) and (c) represent the results of Case-3 by using Eqs. (39), (43), and (48). Fig. 29(b) and (d) demonstrate the results of Case-4 by using Eqs. (34), (37) and (39). The tilted shape profile or nonlinear distortion can be observed in illustrations due to the collimating effect on captured phase-shifted fringe pattern images. Because of this reason, it was required to develop new mathematical models for Case-3 and Case-4 to overcome the shape tilting issue. However, we can see in Fig. 29(e-h), our proposed methods can have better reconstruction accuracy. The cross-section of 3D half sphere and the comparison between the theoretical and the measured one by using our proposed model of Case-3 can be illustrated in Fig. 29(e) and (g), respectively. The RMS of Case-3 was found to be 0.0018 mm. Fig. 29(f) and (h) show the cross-section of 3D shape and the comparison by using the proposed model of Case-4. The RMS difference between the theoretical and the

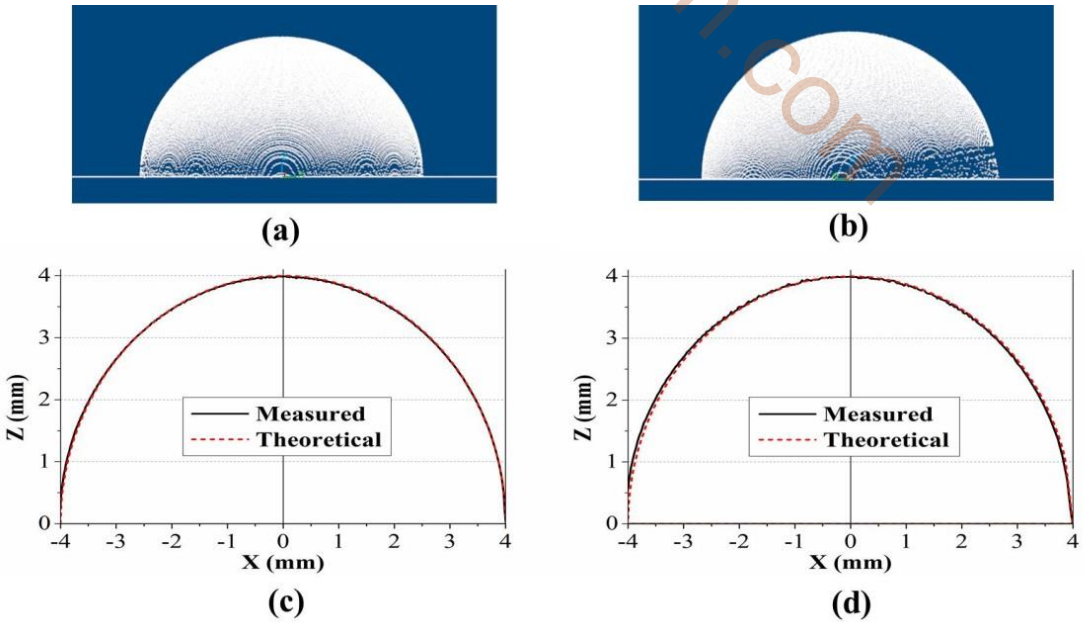

Fig. 28: Reconstruction results of Case-1 and Case-2: the comparison results of the 256th row

measured one was 0.0013 mm. In addition, the reconstructed surface of the half sphere with and without color gradient and software (Graphics User Interface) GUI is presented in Fig. 30. Furthermore, different 3D CAD objects were measured in the virtual environment

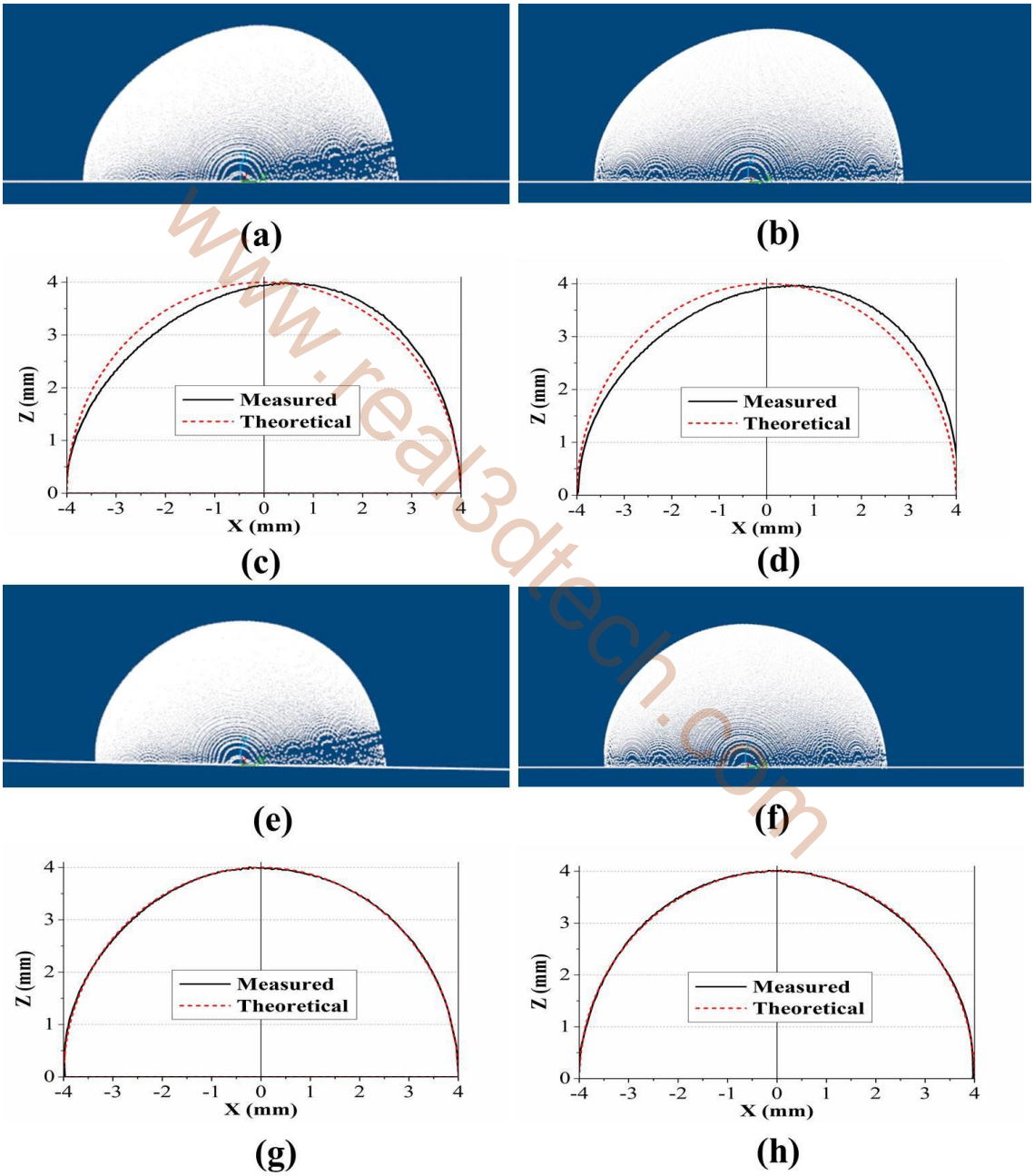

Fig. 29: Reconstruction results of Case-3 and Case-4: the comparison results of the 256th row

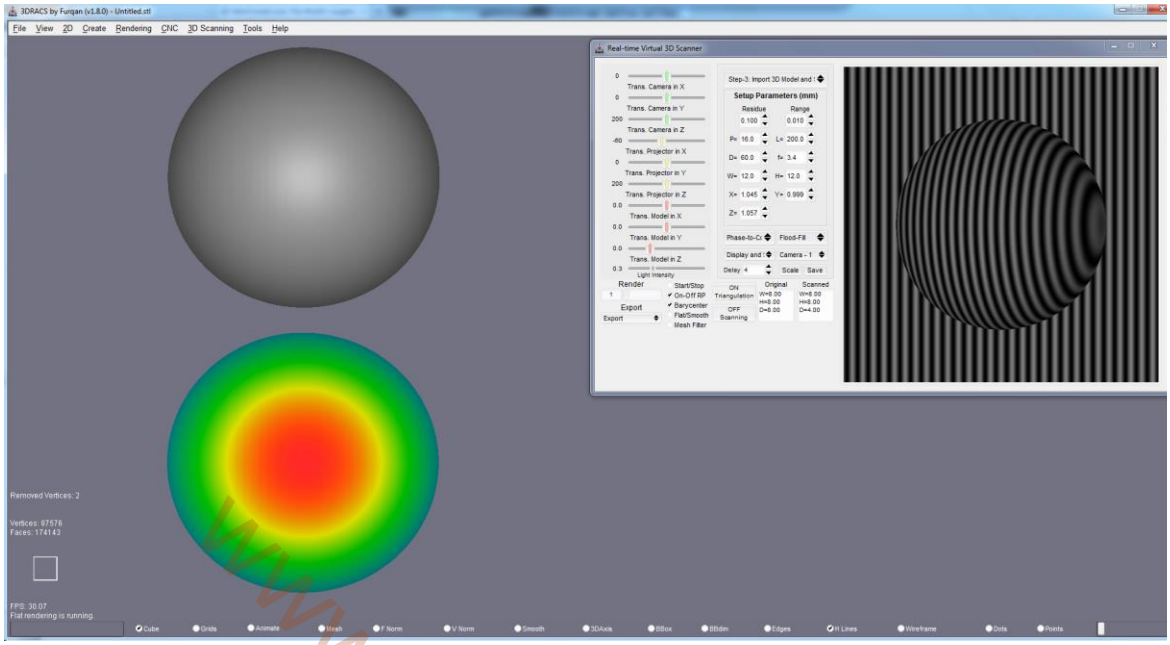

Fig. 30: Reconstructed surface of the half sphere with and without color gradient and GUI of the software

Fig. 31: Virtual measurement of a human face, a duck, and a sculpture

using the proposed models and results are shown in Fig. 31. All experimental results of virtual simulation verify the accuracy and effectiveness of proposed system models to determine the accurate coordinates of the object profile.

4.4 Verification using Optical Setup

Optical experiments in the study of Case-3 and Case-4 have also been carried out to test the accuracy of proposed system models for the determination of accurate object coordinates. The experimental measurement was conducted on an accurate spherical jig with known dimensions using our proposed 3D intraoral scanning system and has presented in Chapter-6. Optical experiments in the study of Case-1 and Case-2 were also carried out using our proposed SMDFP system. The experimental reconstruction was conducted on an accurate step-jig with known dimensions and satisfactory results were obtained. The detailed results are described in Chapter-5.

4.5 Summary

In this chapter, four geometric models of 3D shape measurement systems are examined and evaluated based on collimating and non-collimating projections. The geometric relationship between the camera and the light source device can be precisely defined in the virtual setup. Therefore, a real-time virtual 3D scanning system is used to verify the accuracy and effectiveness of all cases. The four-step phase-shifting algorithm is used to obtain the wrapped phase map that has advantages over various algorithms. To obtain the continuous phase map, quality-guided phase unwrapping algorithm is used. Two system models based on collimating illumination are proposed for calculating the x, y, and z coordinates of the object profile. Experimental results demonstrate that Case-1 has higher reconstruction accuracy than the other cases because the unwrapped phase map is considered to be proportional to the 3D shape for this case. The results of the reconstructed shape are demonstrated, and the observed RMS difference is 0.001 mm which can be neglected. Reconstruction results of Case-2, Case-3, and Case-4 are also presented and the

observed RMS differences are 0.0015, 0.0018, and 0.0013, respectively.

Due to the restriction of size and a collimating lens, there are not many options to configure the system model of the IOS device, therefore, Case-3 is chosen for the system model of IOS device which is tested and verified in this chapter.

Chapter 5. Analysis of Scanning Methodology using Shape Measurement based on Digital Fringe Projection System

This chapter presents a SMDFP system which is capable of performing small and large scale measurements in real-time and can be applied to various applications. In this system, all techniques that we have presented and implemented in the earlier chapters are utilized with the addition of real-time capturing of digital fringe patterns. We will also verify the effectiveness of all the involved algorithms and methods in the development of IOS device using the optical SMDFP system.

5.1 Introduction

In DFP technique, the fringe patterns are generated by a computer, projected through a digital display device such as DLP projector or LCD projector onto the object and obtained the height of an object from deformed fringe images, which are modulated by the object surface. In the research work of this dissertation, a SMDFP system is developed which utilizes a digital CCD camera (THORLABS DCC1645C) with an image resolution of 1280×1024, and the pixel size is 3.6 μm × 3.6 μm. The digital fringe patterns generated and switched by our computer software and projected though LG HS200 DLP projector. The both hardware and software is presented in Fig. 32 which shows the system setup and a measured surface model in the display screen of the software.

5.2 Phase Shifting in Optical System

Since a real-time 3D surface contouring by DMD projection of a color encoded digital fringe pattern whose RGB components comprise three phase-shifted at $2\pi/3$ fringe patterns

is already tested in [97], and also in [7], they deeply focused on real-time 3D shape measurement techniques and introduced 3-step and modified 2+1 phase-shifting techniques

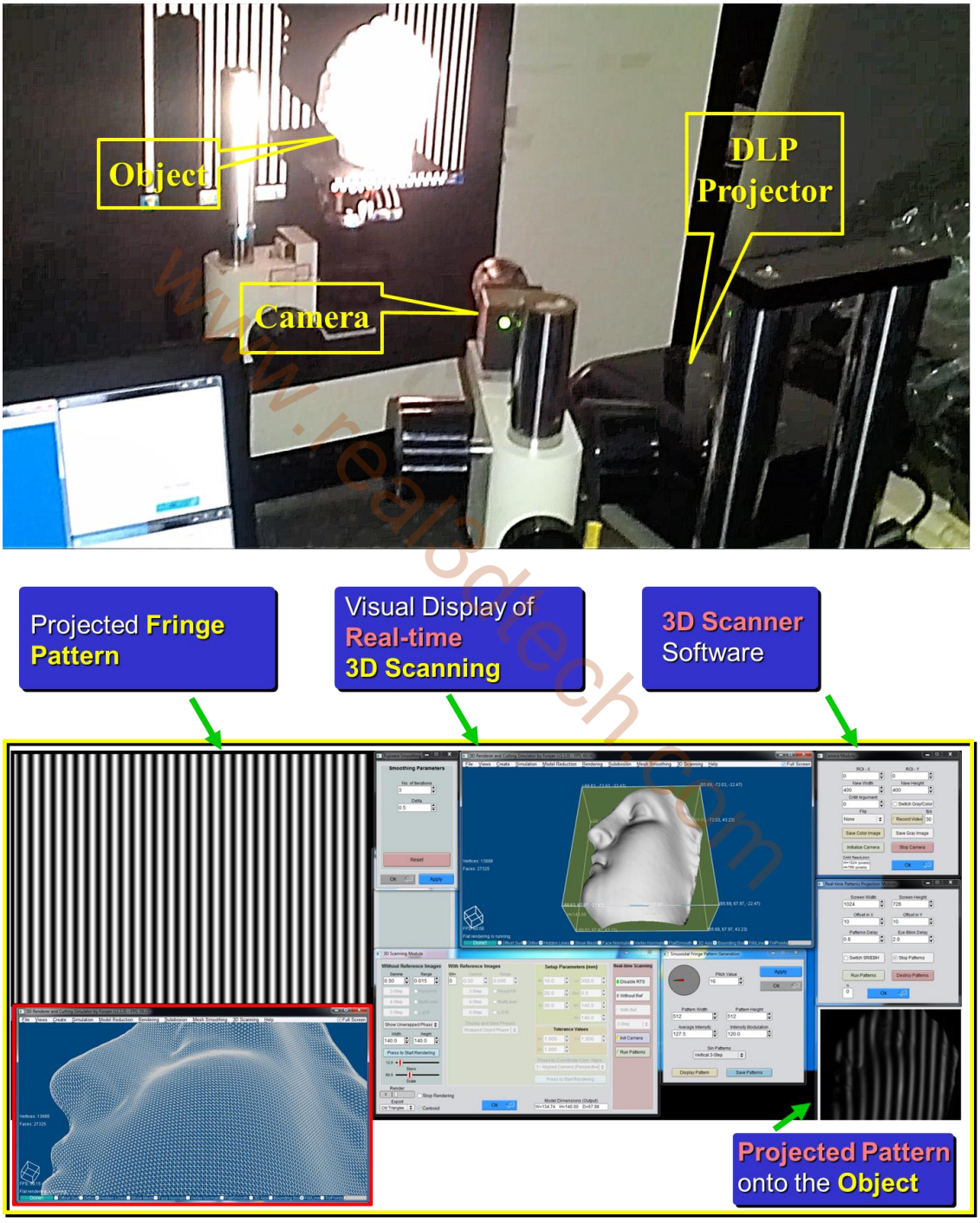

Fig. 32: Hardware setup of the SMDFP system: a sculpture object is being measured and displayed in the display screen of the software

for getting high-speed acquisition. However, in the research work of this dissertation, we focus on the accuracy instead of developing a high-speed 3D acquisition system since high-speed measurement required costly high-speed hardware. Therefore, we used the four-step phase-shifting method which gives us four 512x512 images within < 0.4 seconds with multi-threading and parallel processing. In that case, we can reconstruct 300K points in < 0.5 seconds in one frame. In addition, the developed software is also capable of performing 3D measurements using 3-step and 5-step methods.

5.3 Real-time Fringe Projection and Acquisition

In order to do real-time 3D shape measurement, fringe pattern images must be captured rapidly, 3D reconstruction must be performed quickly, and the reconstructed 3D shapes must be displayed instantaneously in real time. Hence, the coordinate acquisition, reconstruction, and display processes must be completed simultaneously and quickly. In this research we developed a unique way to switch the fringe images because they must be switched and projected rapidly so that they can be captured in a short period of time. Switching of fringe images that is controlled by computer software is similar like a slide show of pictures in which one picture displays after a particular time interval. In order to capture switched image accurately, the camera is perfectly synchronized with the switching speed. However, switching and capturing of fringe images are limited by the graphics card, projection speed, and refresh frequency of the camera. The time delay of switching and capturing images are introduced that can be adjusted in the real-time 3D reconstruction, and for any low or high speed camera, the delay can be increased or decreased for perfect results.

On account of the fact that due to digital fringe generation nature, there is no significant

effect of phase-shift error on DFP and phase-shifting method. However, following issues need to be considered for accurate 3D shape measurement in real-time.

- The refresh frequency of the imaging device.
- The switching speed of fringe images.
- The data transfer from the imaging device to the host computer.

5.4 System Calibration

5.4.1 Calibration Using Computer Simulation

Many simulations have been carried out to show the accuracy of the developed system. In our simulation, an accurate jig with known dimensions is adopted that can be seen in Fig. 33. Simulation was carried out in the real-time virtual 3D scanner and results are presented in Fig. 34-36. Fig. 34 illustrates the real-time virtual 3d scanner in which a virtual jig is reconstructed and displayed. Fig. 35 demonstrates four computer generated fringe patterns projected onto the jig, the wrapped phase map, the unwrapped phase map, and the phase modulation. The graphical comparisons between the theoretical and the measured cross-sections can be observed in Fig. 36. The root mean square (RMS) difference was found to be 0.001 mm. In addition, different shapes with complex profiles are measured and the results are presented in Fig. 37 that shows the reconstructed shapes with alignment accuracy which means that there is no tilt in the reconstructed shapes.

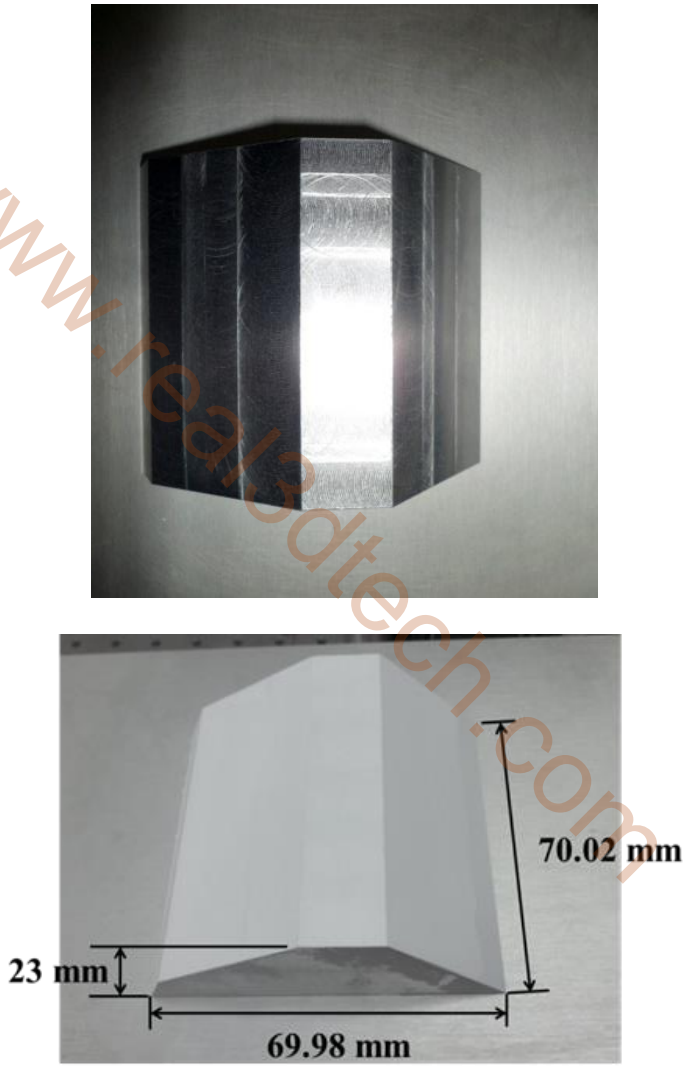

Fig. 33: Machined and painted calibration jig with known dimensions

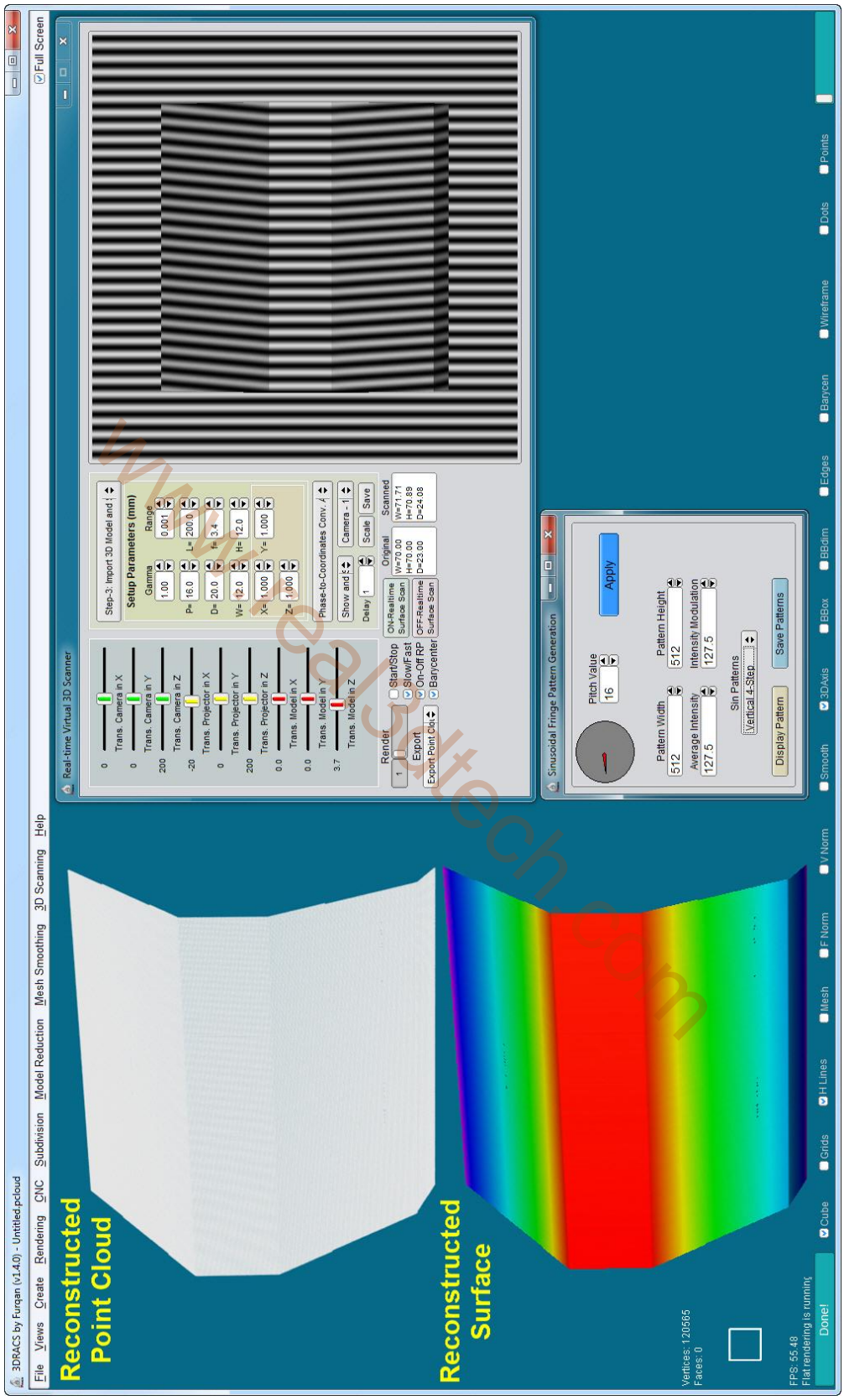

Fig. 34: A virtual jig is reconstructed and displayed in real-time virtual 3D scanner

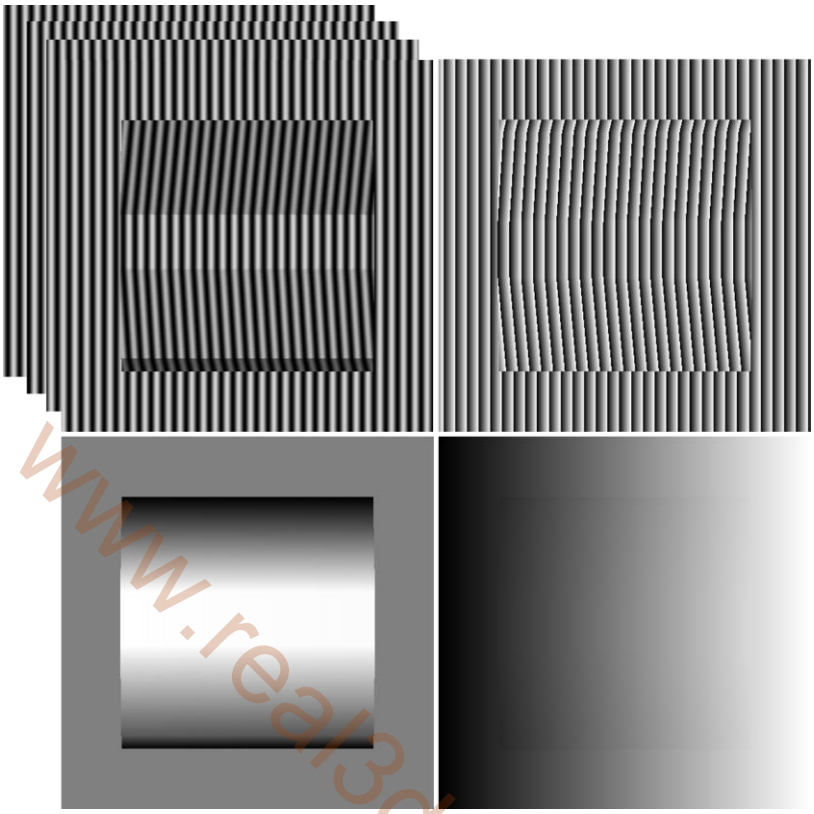

Fig. 35: A virtual jig is reconstructed and displayed in the real-time virtual 3D scanner

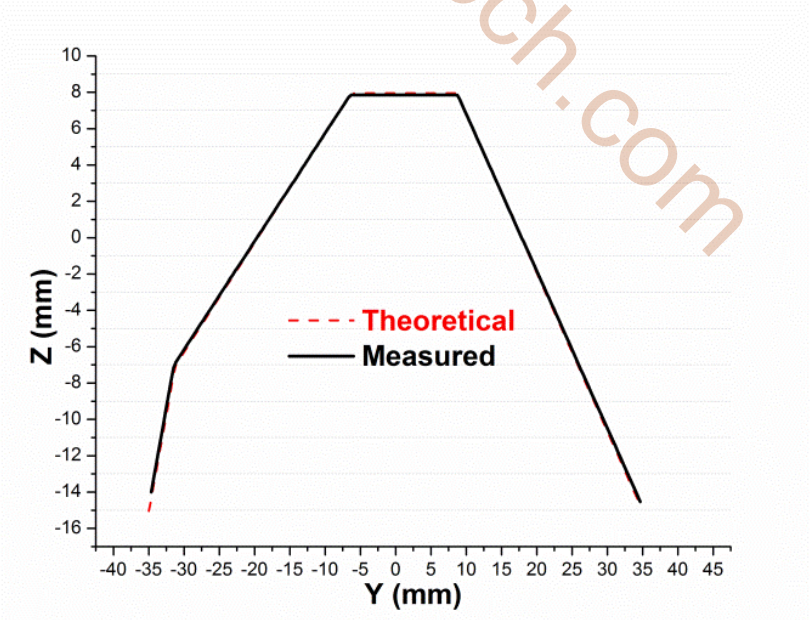

Fig. 36: Virtual 3D measurement: reconstruction result of the calibration jig (the comparison results of the 256th row)

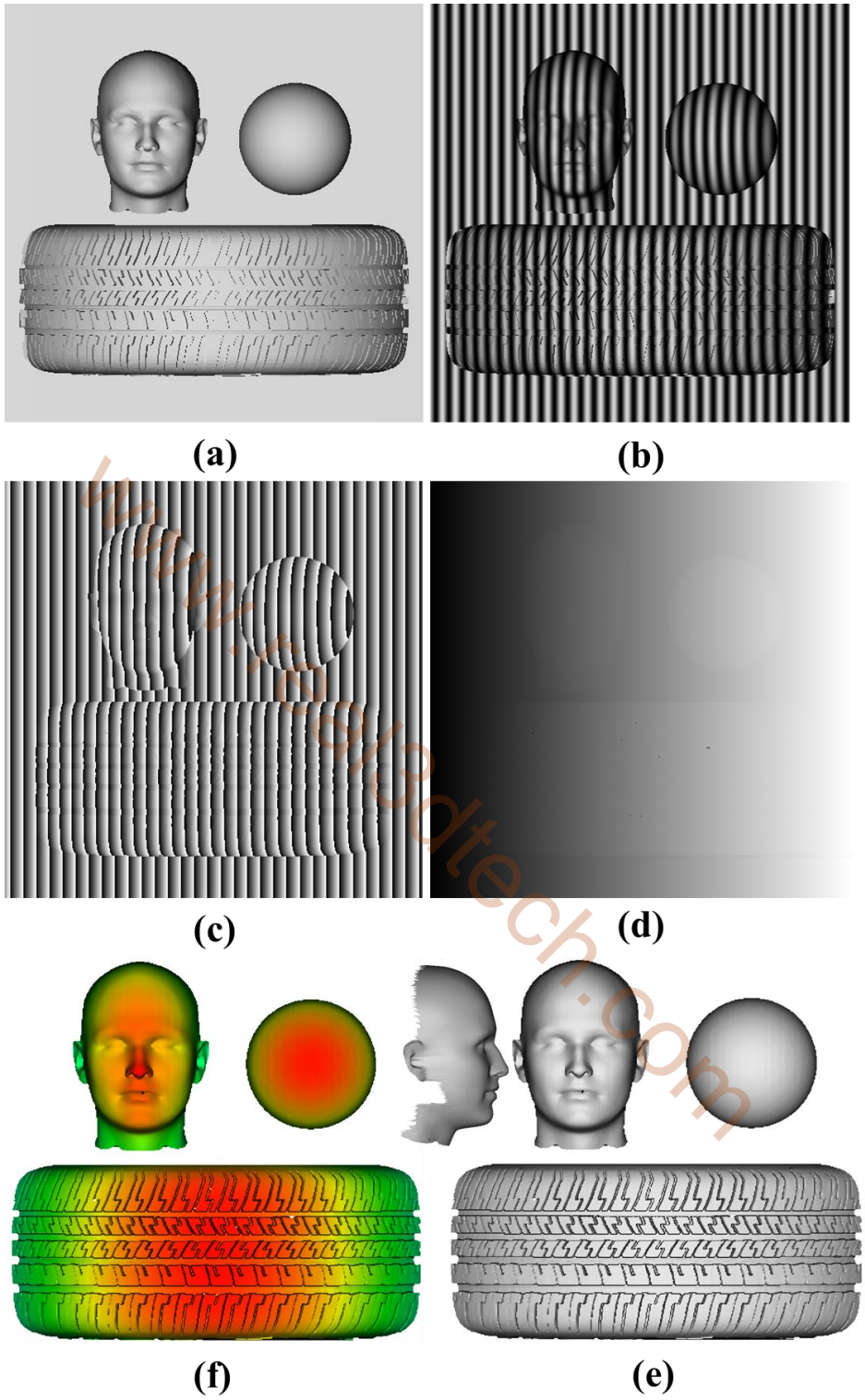

Fig. 37: Virtual 3D measurement: (a) 3D CAD models of different shapes, (b) projected fringe pattern onto the objects, (c) wrapped phase, (d) unwrapped phase, (e) reconstructed shapes, (f) colorized reconstructed shapes

5.4.2 Calibration of the Optical System

In order to calibrate the accuracy and demonstrate the capability of the system, the experimental measurement was first conducted on a flat board with the size 300 mm × 300 mm for the plane measurement. For each measurement, the RMS of the point-to-surface distance between the measured points and the fitted plane was obtained and the maximum error was ±0.036 mm. After that two standard shapes (sphere and cylinder) were measured and compared the measured diameters with their original values in order to estimate the system measurement error. Finally, optical experiments were conducted on an accurate jig with known dimensions, the hardware of the system being measuring the calibration jib can be seen in Fig. 38 and one of the measurement results is illustrated in Fig. 39. It shows one of the four fringe images, wrapped phase, unwrapped phase, and reconstructed surface

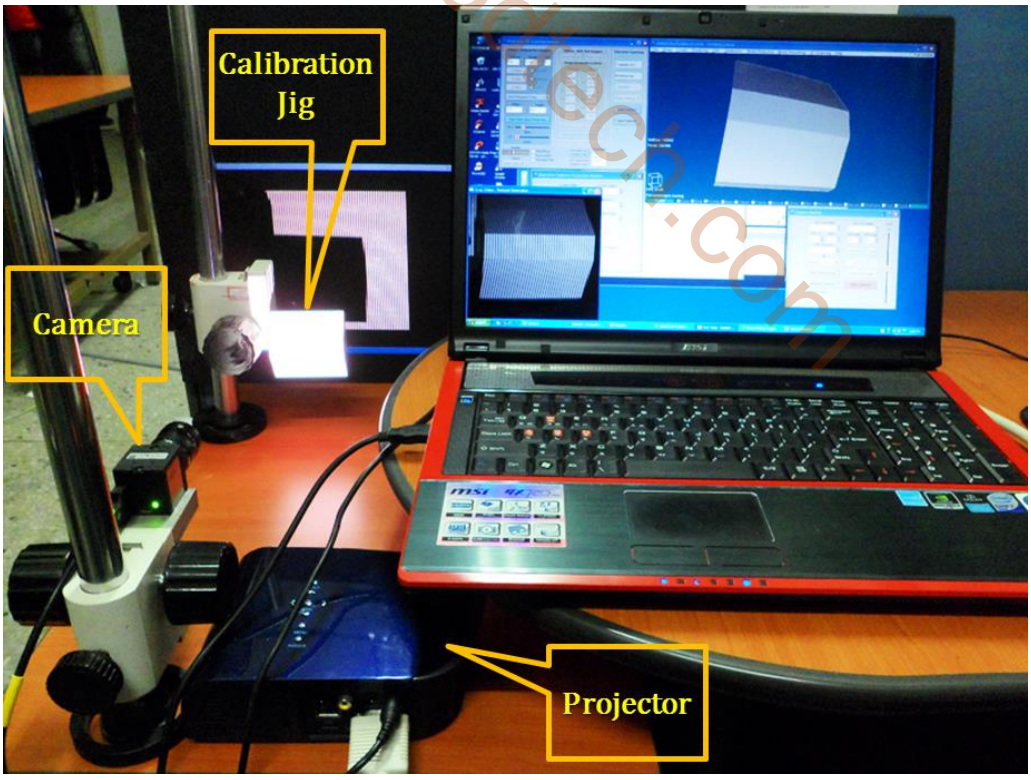

Fig. 38: Optical system setup for 3D measurement of calibration jig

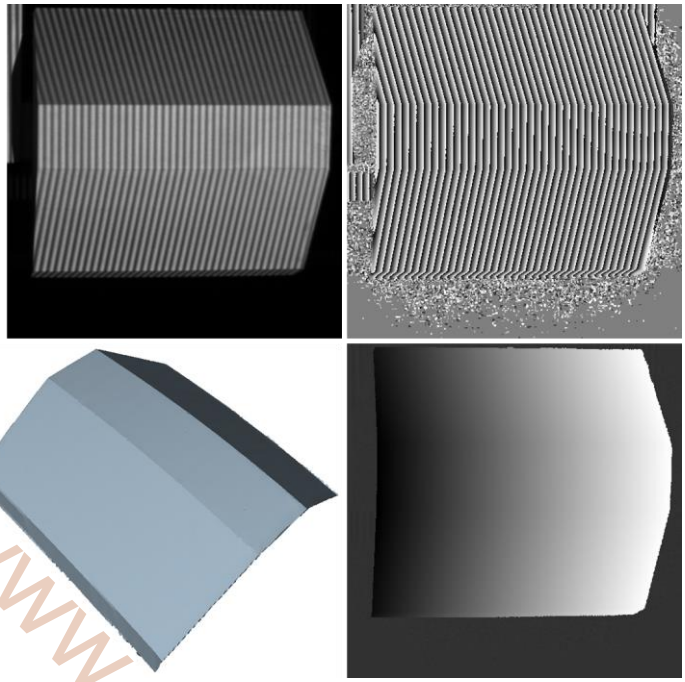

Fig. 39: Optical system calibration: one of the four fringe pattern image (upper left), wrapped phase map (upper right), unwrapped phase map (lower right), and reconstructed surface (lower left).

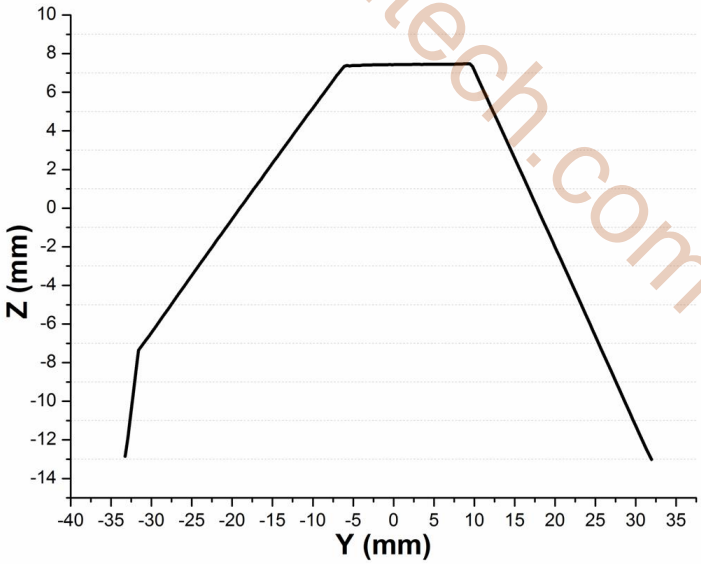

Fig. 40: Optical measurement results of the calibration jig: The result of the 256th row.

of the jig. The accuracy of the 3D reconstructed shape can be observed in Fig. 40 by realizing the profile of the jig. We obtained the measurement error within 0.041 mm.

5.5 Optical Experiments

Various experimental measurements were also conducted to perform the real-time 3D shape measurements to verify the capability of the system in an open and large scale environment. The implementation process of the optical measurement can be realized in Fig. 41 that presents a flow chart of the relationship of algorithms involved in SMDFP. The 3D measurement results of many shapes using the developed optical system are shown in Fig. 42-46. All the illustrations demonstrate reconstructed shapes of real-world objects with and without color texture. The four-step phase shifting method was utilized with SUSAN and Two-step noise reduction filters. The noise reduction filters refine the outer surface of the scanned object and improve its quality.

Fig. 42 presents the reconstructed shapes of small plastic toys (blue teddy bear and pink pig) with color textures, wireframe cross-sections and one of the four fringe patterns of both shapes can also be seen in the figure. Fig. 43 demonstrates the reconstructed shapes of complex surfaces of different physical objects (plaster model of human jaw, human hand, and paper coffee cup) with and without color information. Fig. 44 gives the reconstructed shapes of shiny and diffused plaster models. A shiny surface of a plaster jaw model with color information, wireframe cross-section, and one of the four fringe patterns is shown in the figure. The other two models were reconstructed from diffused plaster surfaces.

Fig. 45 illustrates the reconstructed shapes of human faces with black and white texture information. The upper 3D shape contains 210K triangles and the lower 3D shape contains 235K triangles. Finally, a human hand is being reconstructed in real-time and displayed in Fig. 46. The camera capturing window displays one of the four phase-shifting fringe patterns. The object was reconstructed, displayed with color texture

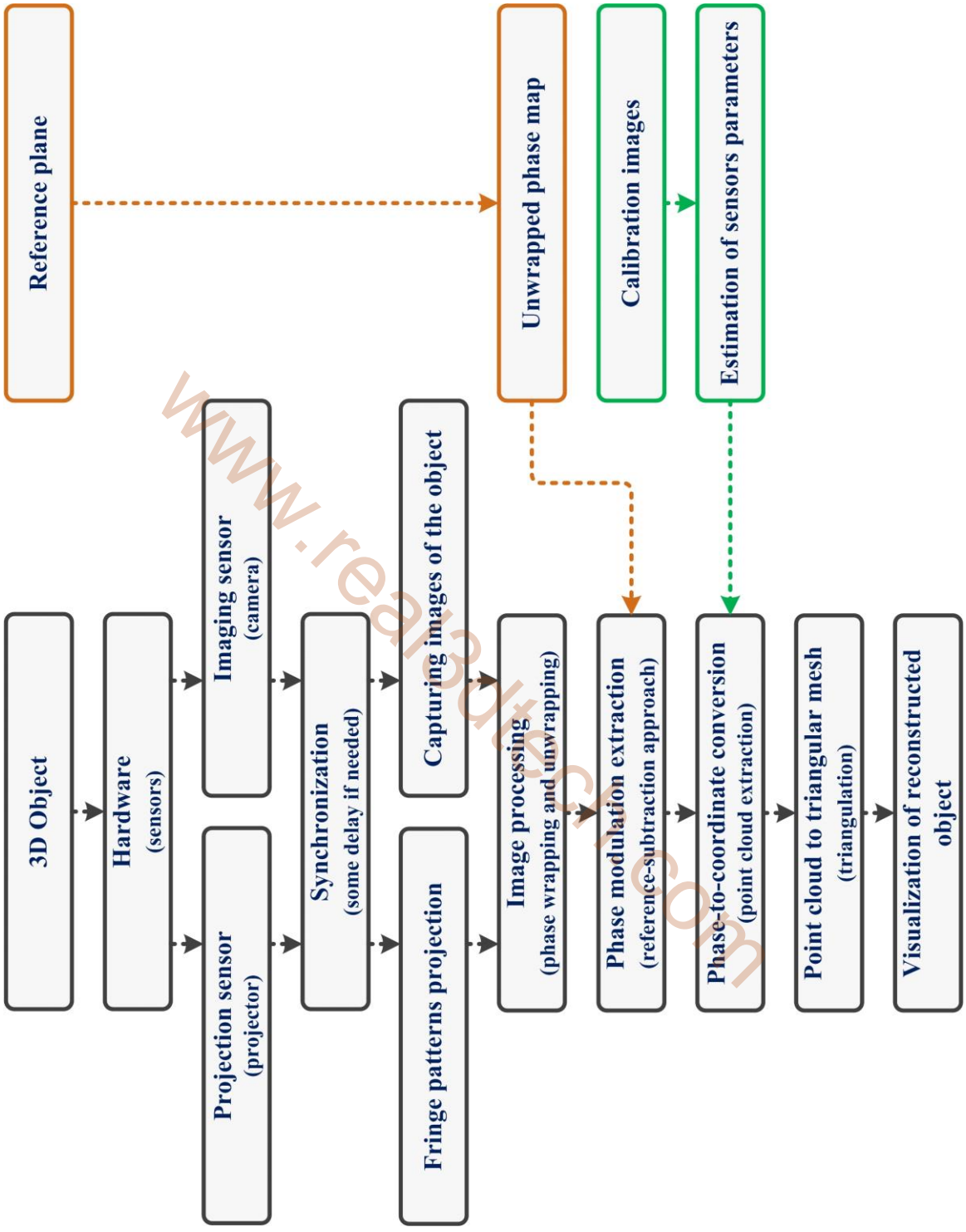

Fig. 41: Optical system: Flow chart of the measurement process involved in SMDFP system

information, and updated, simultaneously. The dense point cloud can also be seen in the

figure. One scan was obtained in less than one second with more than 200K triangles.

The reconstructed results indicate that our system has good performance for 3D shape measurement.

Fig. 42: Optical measurements: reconstructed shapes of small plastic toys (blue teddy bear and pink pig) with color textures, wireframe cross-sections and one of the four fringe patterns of both shapes

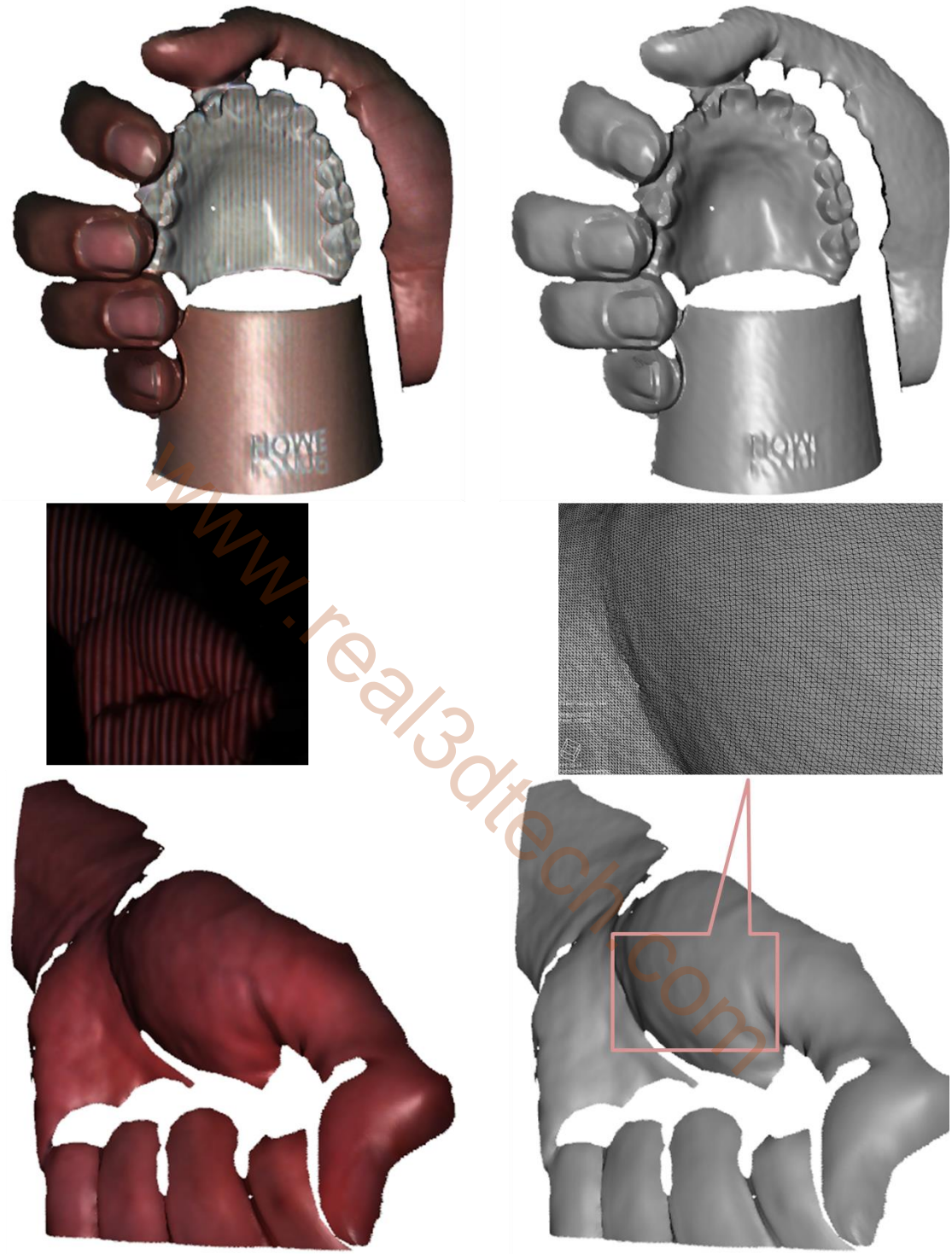

Fig. 43: Optical measurements: reconstructed shapes of complex surfaces of different physical objects (plaster model of human jaw, human hand, and paper coffee cup) with and without color information

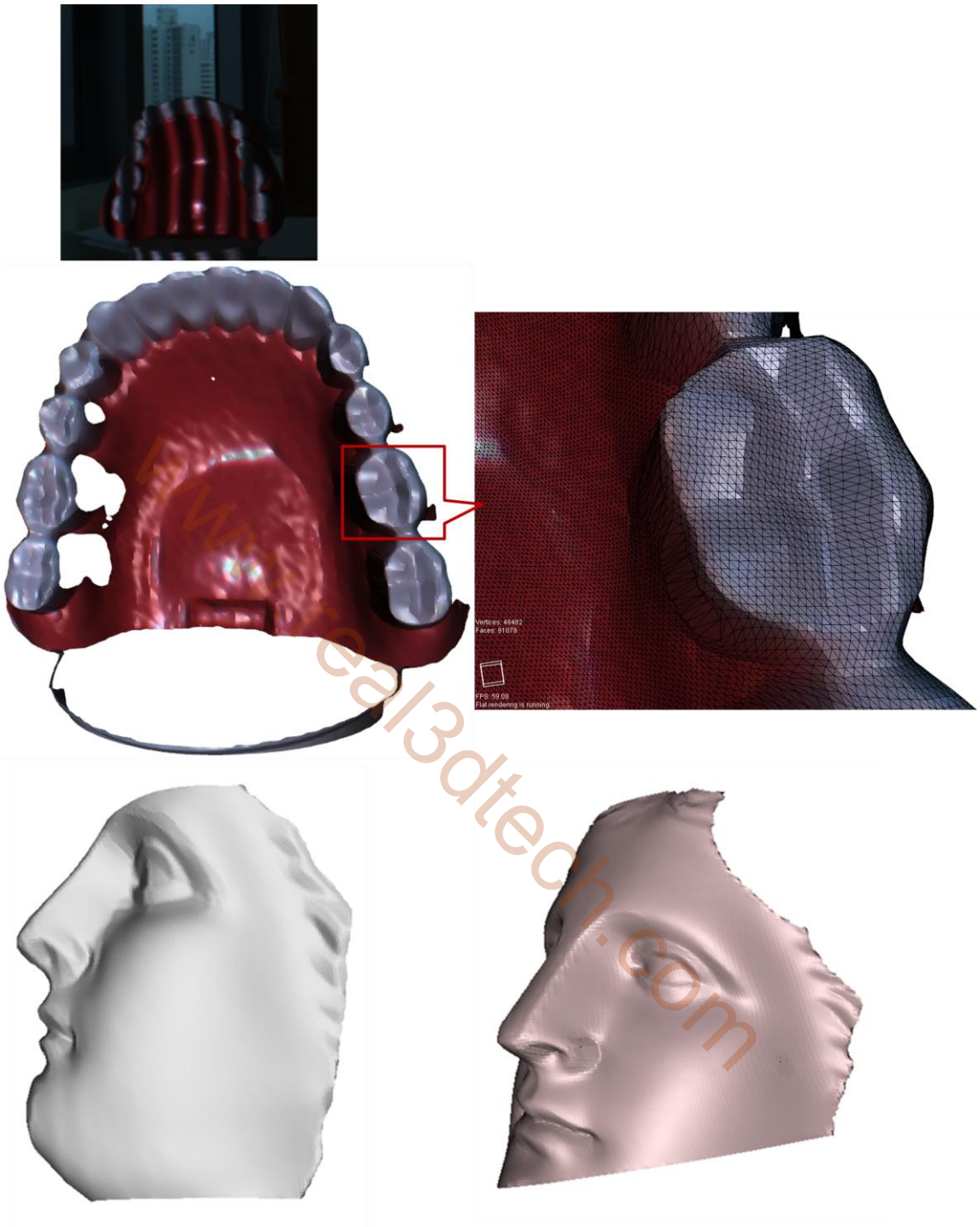

Fig. 44: Optical measurements: reconstructed shapes of shiny and diffused plaster models. A shiny surface of a plaster jaw model with color information, wireframe cross-section, and one of the four fringe patterns is shown in the figure. The other two models were reconstructed from diffused plaster surfaces.

Fig. 45: Optical measurements: reconstructed shapes of human faces with black and white texture information. The upper 3D shape contains 210K triangles and the lower 3D shape contains 235K triangles.

Fig. 46: Optical measurements: a human hand is being reconstructed in real-time and displayed. The camera capturing window displays one of the four phase-shifting fringe patterns. The object was reconstructed, displayed with color texture information, and updated, simultaneously. The dense point cloud can also be seen in the figure. One scan was obtained in less than one second with more than 200K triangles.

5.6 Summary

A DFP based 3D shape measurement system is presented in this chapter. The experimental measurements of various shapes were carried out to verify the capability and performance of the proposed system. The developed system is capable of performing small and large scale measurements in real-time and can be applied to various applications. The measuring results of the calibrated shapes indicate that the measurement error is less than 0.041 mm with a variability of ±0.036 mm for our system. From measurement results, it can be concluded that the developed system and adopted methodology are effective in obtaining 3D surface profiles for industrial applications, especially in the reverse engineering. And it can also be observed that our adopted methods and algorithms for the development of IOS device are effective and can give reasonable good results.

Chapter 6. Development of an Intraoral Scanner

This chapter gives the development procedure of the 3D intraoral scanner. The proposed idea of 3D intraoral scanning device for dentistry can be seen in Fig. 47. A robot arm is also developed in order to automate the intraoral scanning.

6.1 Introduction

Due to the restrictions of size and volume on the 3D scanner for dental applications, it is not easy to perform non-contact profile scanning in the mouth cavity and there are not so many 3D profile measurement tools designed specifically for narrow spaces, for example, to scan the tooth shape of a human jaw. Some existing intraoral scanners adopted non-contact optical technologies such as structured light interferometry and phase shifting, active and passive stereovision, confocal microscopy, triangulation, photogrammetry, and optical coherence tomography. The CEREC™ (Ceramic Reconstruction) system provides a 3D tooth-form scanner for measurement in the mouth cavity [84]. In earlier system, the sinusoidal fringe pattern is projected onto the tooth surface in the mouth cavity using the

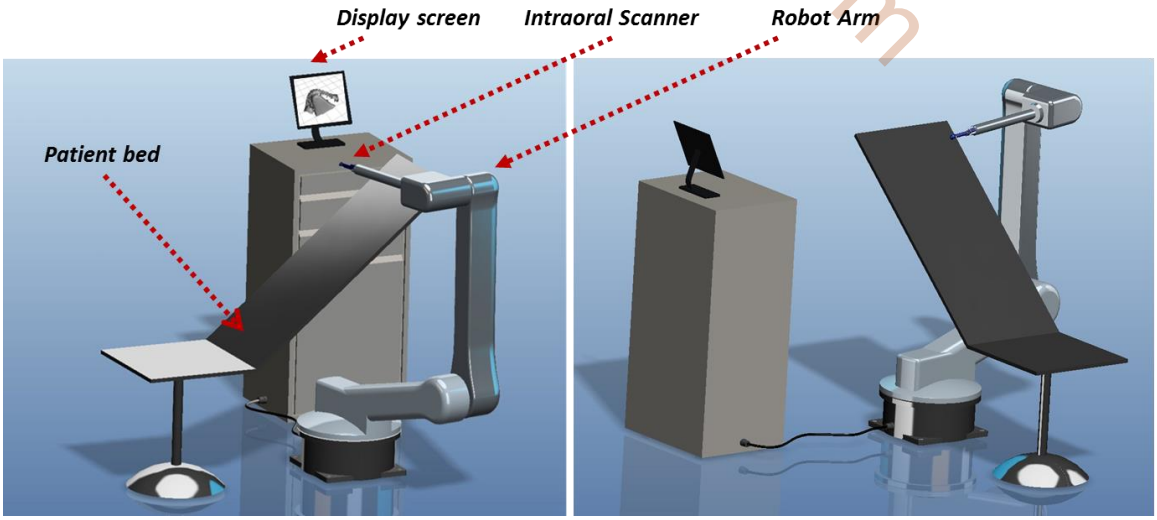

Fig. 47: An idea for 3D intraoral scanning system

structured light infrared laser ray; the latest version employs blue light-emitting diodes (LEDs). The phase-shifting technique is used for the measurement of the tooth profile. Afterward, the depth of the tooth profile is obtained from deformed fringe patterns. Furthermore, Liang et al. proposed a 3D surface profilometer with a miniaturized probe using the digital fringe projection (DFP) principle [85]. They utilized coherent image fibers and a digital micro-mirror device (DMD) chip as the structured fringe generator. Riehemann et al. presented an intraoral 3D scanner for the registration of dental surfaces directly inside the patient's mouth that works on the principle of phase correlated fringe projection. They used a projection path that consists of the projection optics and of the illumination optics with a light-emitting diode as light source illuminating the Liquid Crystal on Silicon (LCoS) display [21]. Furthermore, some existing intraoral scanning devices for restorative dentistry are described below.

The Lava™ Chairside Oral Scanner was officially launched in 2008. The product has introduced an entirely new method of capturing 3D data based on the principle of active wavefront sampling with structured light projection. This scanning system provides an active three-dimensional imaging system that includes an off-axis rotating aperture element placed either in the illumination path or in the imaging path of an optical apparatus. The product allows capturing 3D data in a video sequence and models the data in real time (approximately 20 3D datasets per second). After the preparation of the tooth and gingival retraction, the entire arch is dried and lightly dusted with powder to locate reference points for the scanner [87].

IOS FastScan system is based on the principle of active triangulation according to Schleimpflug imaging principle with sheet of light projection. The Scheimpflug principle is a geometric rule that describes the orientation of the plane of focus of an optical system

wherein the lens plane is not parallel to the image plane [88].

Densys3d system employs the principle of active stereophotogrammetry with structured light projection. The intraoral scene is illuminated by a 2D array of structured illumination points. 3D models are obtained from the single image by triangulation with a stored image of the structured illumination onto a reference surface such as a plane [89].

DPI-3D is an accordion fringe interferometry (AFI) principle based intraoral imaging system. AFI employs light from two point sources to illuminate an object with an interference fringe pattern. A high precision digital camera is used to record the curvature of the fringes. The degree of apparent fringe curvature coupled with the known geometry between the camera and laser source enable the AFI algorithms to digitize the surface of the object being scanned [90]. However, most intraoral scanners are passing the prototype testing phase and only some devices are currently available on the market. Most of them are largely under development; accuracy is still needed to be improved in current scanners [91].

The research work of this dissertation presents the development procedure of a 3D intraoral scanner based on structured light fringe projection technology. In this research work, three devices are developed with different hardware. In the first device, piezoelectric transducer (PZT) is utilized in order to move the grating with fringe patterns. Second device replaced PZT with the voice coil actuator (VCA) in order to obtain accurate phase shifts as well as gain the stability of the device. Third device is the improved version of the second hardware in term of design, specifications, and accuracy.

6.2 Intraoral Scanning Device

First device is based on PZT and collimating illumination for the measurement of tooth

profiles in the mouth cavity. The proposed scanning device comprises a laser diode (LD) beam, a micro charge-coupled device (CCD) for capturing the dental images, a grating for producing the series of parallel fringe strips, a PZT for phase shifting the interferogram, a set of optical lenses, and a Polhemus device sensor. Note that instead of computer generated phase-shifting fringe strips, the fringe strips are produced by the grating and PZT graticule. The structured light of the fringe pattern of the laser beam is projected onto the shape of the tooth. The CCD imaging device captures the projected patterns which are modulated by the tooth profile and then transmitted to the host computer for image processing, reconstruction of the depth of the tooth shape, display, and so forth. The phase shifts of the projected fringe patterns are controlled by the PZT that expands or contracts with an externally applied voltage. If the applied voltage varies smoothly, a phase-shift of a desired form or series of steps can be produced. Furthermore, considering the small volume and light weight of the proposed scanner, this system is capable of measuring the 3D profile in a narrow space environment.

6.2.1 Optical System Architecture

A structured light pattern which is a series of parallel fringes produced by the grating projects onto the surface of the tooth through a LD beam, a circular LD module which acting as a red-light illuminator emits a laser beam with a circular profile from the LD itself. Afterwards, phase shifts are measured by the PZT with good precision, the fringe pattern is reflected by the surface of the tooth and passes through a mirror, and then a prism directs the light onto the CCD sensor. The CCD camera is used to record the phase-shifted fringe images. Finally, the phase-to-coordinate calculation technique can be employed for coordinate acquisition of the object profile. Fig. 48 shows the hardware and

software architecture of the proposed optical 3D measurement system. It has three sections left, middle, and right. Right section describes the hardware of the system in which phase-shifting fringe strips are produced, projected onto the object, and captured. Once the images are captured, image processing techniques such as phase wrapping, phase unwrapping, and coordinate acquisition are employed in the middle section. The laser/PZT control module controls the illumination of the LD and the motion of the PZT. The step motion of the PZT translation is also controlled by the control module which influences the real-time speed of the scanner. Decreasing the PZT step interval increases the speed of the scanner. It is important to mention here that the reciprocating motion of the PZT and the obtained phase shifts are not proportional due to the mechanical nature of the PZT transducer. Therefore, the calibration of the PZT for accurate phase shift is a critical and challenging issue if good measurement results are to be obtained using phase shifting interferometry (PSI). Finally, the scanned point cloud is further processed, converted into surfaces, and display in the left section.

6.2.2 Hardware Design of the Optical System

Fig. 49 demonstrates the system architecture, optical hardware, and CAD design model of the developed device. A set of optical lenses is utilized, which are designed for light coupling and filtering. A collimating automatic double lens is used for straightening the fringe pattern produced by the graticule after the LD beam passes through the set of optical lenses. A 90^{o} optical reflector mirror is used for guiding light onto the surface, and a 90^{o} prism is utilized to guide the reflected light patterns by optical mirror to the CCD sensor. The camera is a digital CCD camera (THORLABS DCC1645C) with an image resolution of 1280×1024, and the pixel size is 3.6 µm [92]. The projected fringe pattern area on the

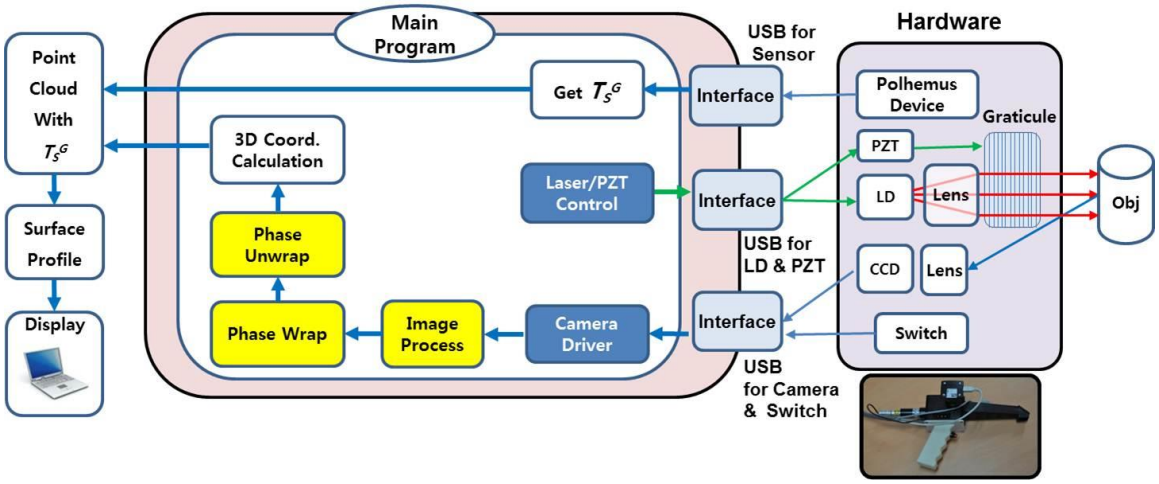

Fig. 48: Architecture of the optical IOS device

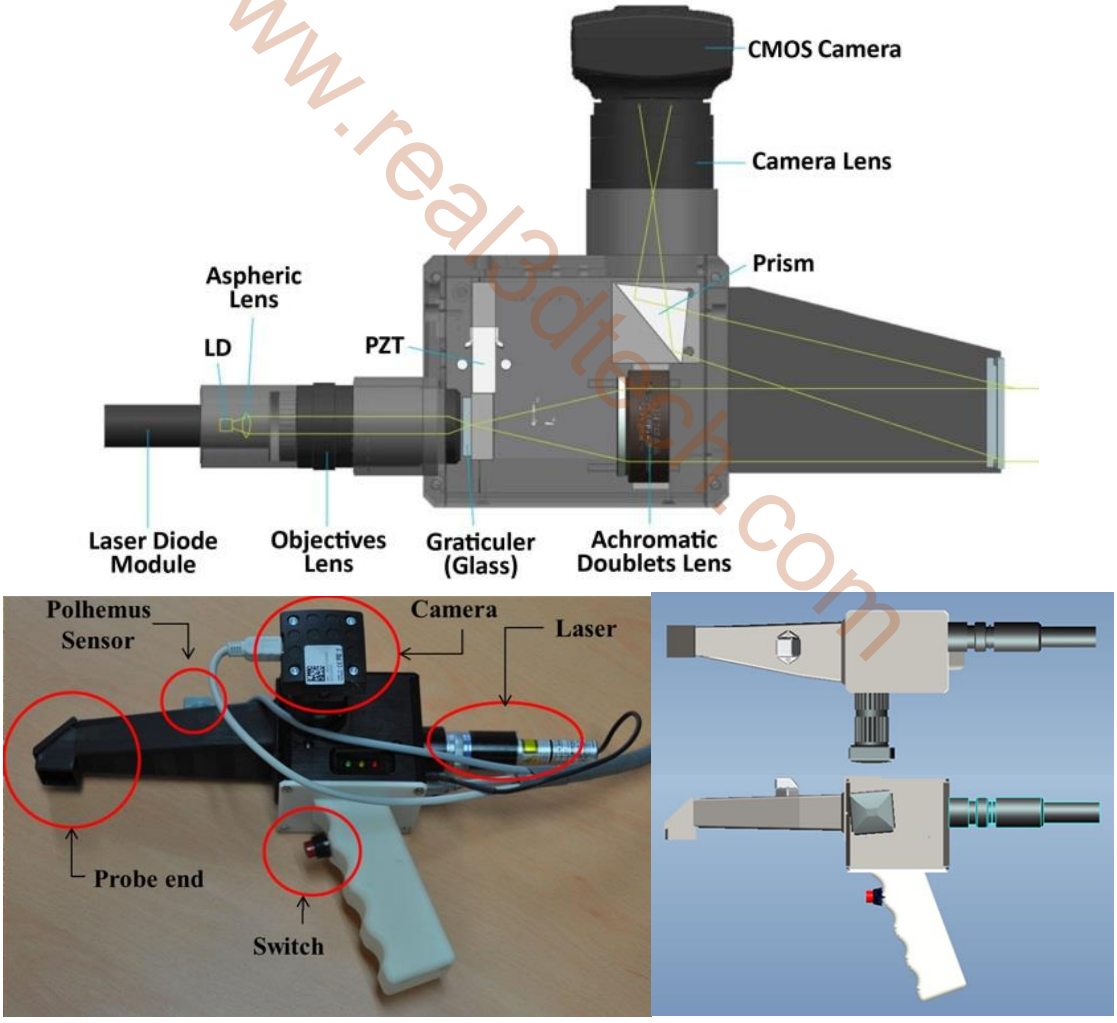

Fig. 49: IOS device: (top) internal design of the optical device, (bottom left) optical hardware, (bottom right) CAD design of the device

object profile is defined according to the probe end and only the central 512×512 pixel region is chosen as the frame size. The number of fringes generated by the graticule is 30 fringes per image. The laser diode module (Lanics Laser Electronics LM-6535MR, 658nm) combines laser diode technology, three element lens optics, and sophisticated electronics within a slim and light aluminum anodized housing [93]. The length of the LD module is 72 mm; its diameter is 14 mm. Furthermore, the probe length was minimized to keep the scanner body as compact as possible for the convenience of dentists and their clients. The probe which has to be inserted into the mouth has a section of about 24 × 24 mm and a length of 148 mm. The housing is fabricated with rapid prototype material; however, any metal or plastic material can be used as the construction material.

6.2.3 Phase Shifting in Intraoral Scanning

In order to perform the 3D measurement, the phase needs to be retrieved from the projected fringe images. Among the described algorithms in Chapter-2, the most common four-step phase-shifting algorithm with quality-guided phase unwrapping algorithm is adopted. A comprehensive discussion about the analysis of the four-step phase-shifting algorithm with PZT transducers is given in [94-95]. Due to mechanical nature of the PZT transducer, it is assumed that the phase shift between two adjacent fringe patterns is not constant if the wavelength change is directly proportional to the time. The relationship between phase shifts and the PZT translation becomes nonlinear. Therefore, by experimental evaluation, Fig. 50 shows the nonlinear relationship between the PZT steps and obtained phase shifts, and Table 1 describes the phase shifts for four image patterns according to the PZT translation. However, the nonlinearity of the PZT can be neglected

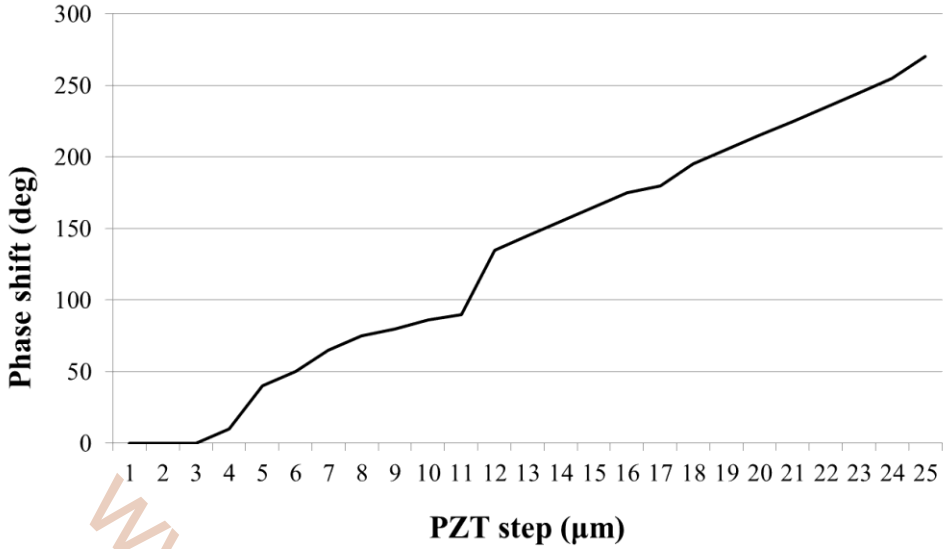

Fig. 50: Relationship between PZT step motion and obtained phase shifts

Table 1 Obtained phase shifts from PZT step motion

PZT step(μm)	*Phase shift (deg)*
5	0
11	90
17	180
25	270

(assuming that the nonlinearity of the PZT is small enough) even though the phase shift algorithms for phase calculation requires a constant phase shift (ideally). If the nonlinearity is large, then this problem can introduce a considerable error in the measurement but by calibrating the PZT for proper phase shift can reduce the nonlinear error. Yeou-Yen et. al [12]. describes some practical methods to calibrate the phase shifter in PSI and they proposed a numerical method that can provide a better repeatability with a standard deviation of ~0.046^{o}.

6.2.4 Coordinate Calculations

As can be seen in Fig. 15, the collimating illuminative device (red light laser) is aligned

with the axis of the object and a camera captures the deformed fringe strips by having some distance from the optical axis of the illuminating device. As we have proposed a mathematical model for Case-3 in Chapter-3, in this case, the (X, Y) coordinates are not proportional to the imagining index (i, j). Therefore, in order to obtain the accurate 3D shape for this case, a nonlinear approach is proposed for the collimating illumination system and the measurement results can be seen in Fig. 23.

6.2.5 Optical Experiments using Intraoral Scanner

Optical experiments have been carried out to test the feasibility of the developed system. The system was first calibrated by considering the PZT phase-shifts, lens distortion, and camera lens parameters to obtain accurate projected fringe patterns. From various experiments, it was observed that after 4 μm of PZT travel, it starts to produce phase shifts; therefore, the first 4 μm were not used during the phase-shift process. The second observation relevant to the PZT was that it works in discrete time steps, which means that some real-time frames have to be skipped in order to obtain a 1-μm translation. In our experiments, the time-interval was set to 20 ms to obtain a 1-μm translation of the PZT.

The experimental measurement was first conducted on an accurate spherical jig with

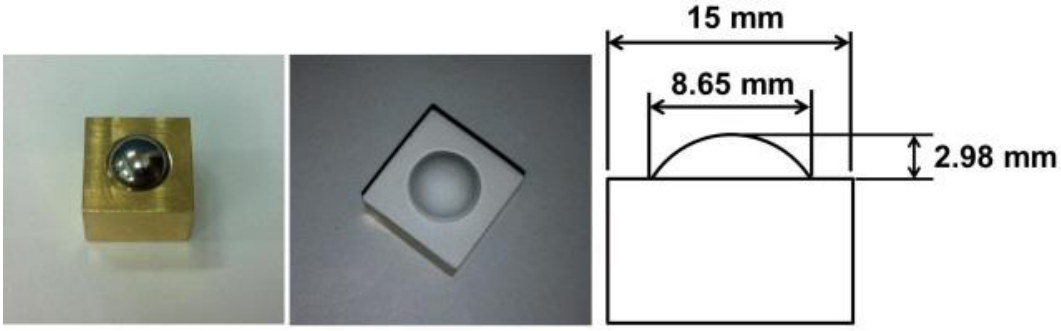

Fig. 51: Calibration jig: (left) spherical steel ball with a cube, (middle) coated jig, (right) dimensions of the jig

known dimensions in order to calibrate the accuracy and demonstrate the capability of the system. Fig. 51 shows the spherical steel ball with a cube, coated jig, and the jig with dimensions. The phase-shifted stripe patterns were generated and projected onto the calibration jig as shown in Fig. 52. Once the images were captured by the camera, the wrapped and unwrapped phase maps were obtained by using the described methods with

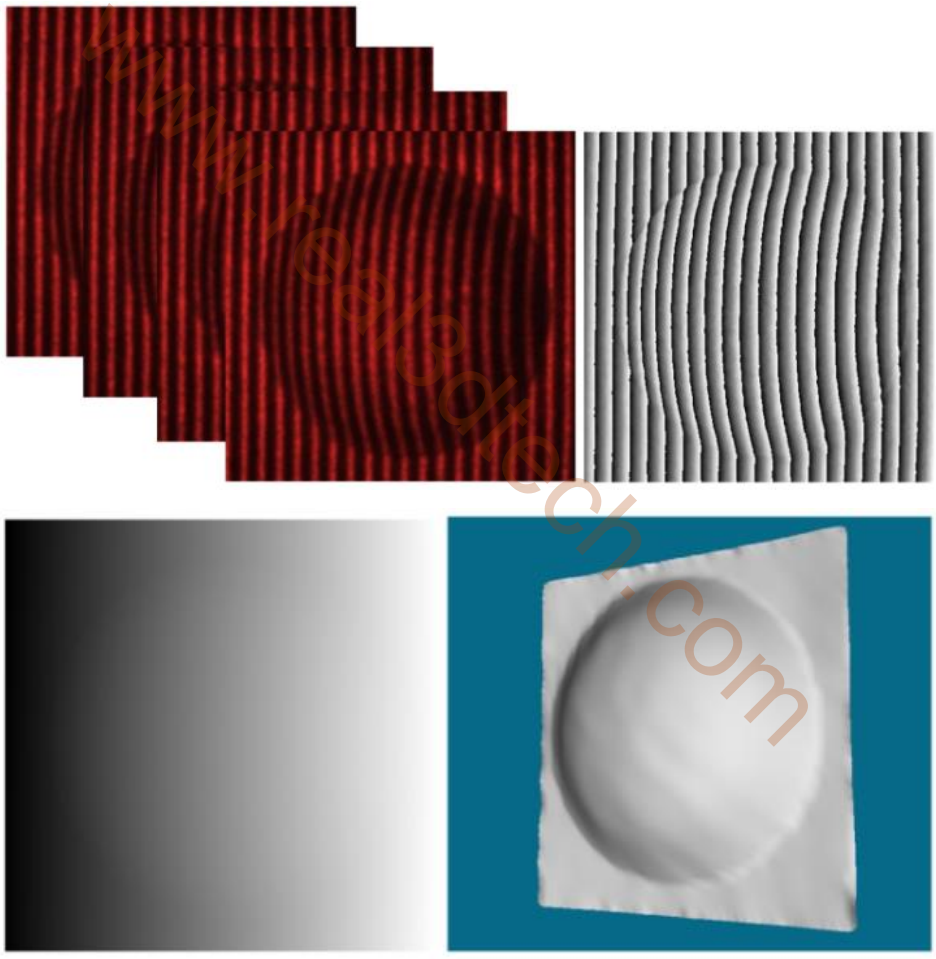

Fig. 52: Optical measurement results of the calibration jig: (top left) Fringe patterns generated by the optical system, (top right) wrapped phase map, (bottom left) unwrapped phase map, (bottom right) reconstructed 3D surface model

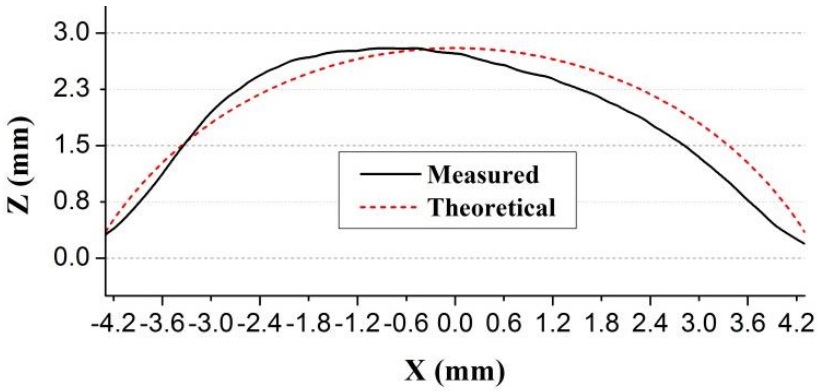

Fig. 53: Comparison between the reconstructed 3D shape and the theoretical one: without using our method

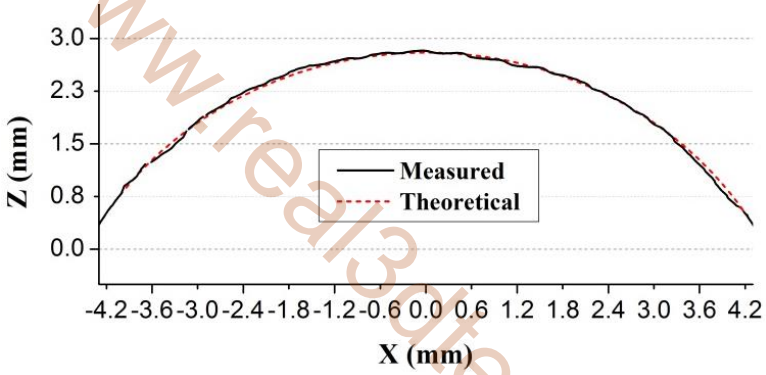

(b)

Fig. 54: Comparison between the reconstructed 3D shape and the theoretical one: with using our method

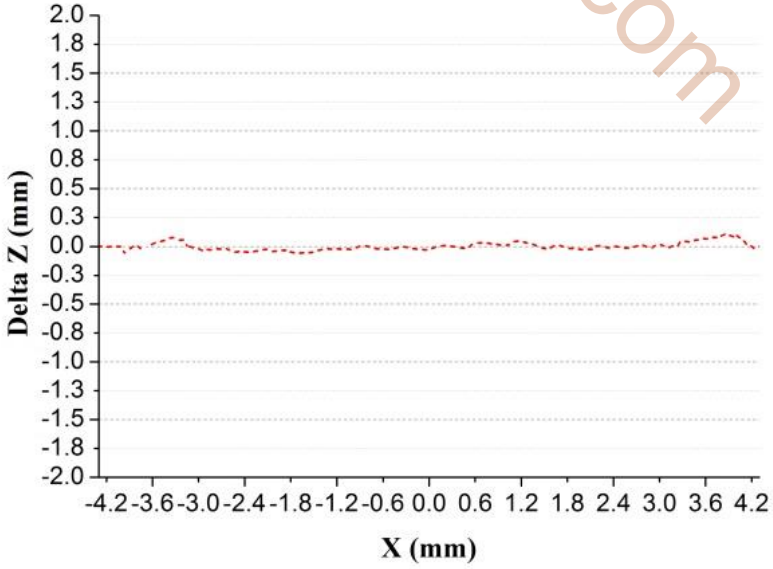

Fig. 55: Depth difference [RMS: 0.035 mm]

low-pass and medium-pass filtering, after that, the coordinate acquisition, reconstruction, and display processes were performed, and final reconstructed shape can be seen in Fig. 52 (Bottom right). The accuracy of the 3D reconstructed shape can be observed in Fig. 53-54 by realizing the profile of the spherical jig. Fig. 53 shows the reconstructed shape profile without using our method and Fig. 54 demonstrates the results of the proposed method. In addition, the difference between the measured jig and the theoretical sphere can also be observed in Fig. 55. The maximum measured error of the spherical jig profile was found to be ±0.07 mm, and the RMS difference was found to be 0.035 mm. The errors may occur because of the nonlinear intensity variation or non-uniform distribution of illumination on the captured images and inaccurate phase shifts. To overcome this problem, the intensities of the patterns and PZT calibration need to be optimized in future. However, it is noteworthy that the proposed method for Case-3 corrects the shape tilting issue based on a nonlinear phase-to-coordinate relation under collimating illumination, and it provides a rigorous theoretical base for the practical applications of fringe projection profilometry.

Optical experiments in the study of Case-3 and Case-4 have also been carried out to test the accuracy of proposed methods for the determination of accurate object coordinates. The experimental measurement was conducted on an accurate spherical jig with known dimensions using our proposed fringe projection based intraoral scanning system and it was observed that the proposed methods correct the shape tilting issue based on a nonlinear phase-to-height relation under collimating illumination, and it provides a rigorous theoretical base for the practical applications of fringe projection profilometry.

In order to verify Case-4, we used the same system but with the rotated spherical jig along Y-axis. By doing this, we can easily achieve the system setup similar to Case-4. Results were found to be similar to simulation results. The optical experimental results also verify

the accuracy and effectiveness of our developed approaches for Case-3 and Case-4.

An experimental measurement was also conducted to perform the intraoral dental profile measurement to verify the capability of the system within a narrow space. The 3D measurement results of the dental model using the developed system are shown in Fig. 56. Using the developed system software, Fig. 56 shows the scanned object of a dental tooth. It demonstrates one of the phase-shifted fringe patterns, wrapped and unwrapped phase maps, and the reconstructed surface of the 3D shape. The teeth measurements were made without powdering of the teeth. The one sample scan was obtained in <1 sec. The experimental results verify the effectiveness of the developed system within a narrow space and it can also be applied to various microscale measurement applications.

6.2.6 Discussion and Issues

There are several issues observed and analyzed in the 1st IOS device and are discussed as follows:

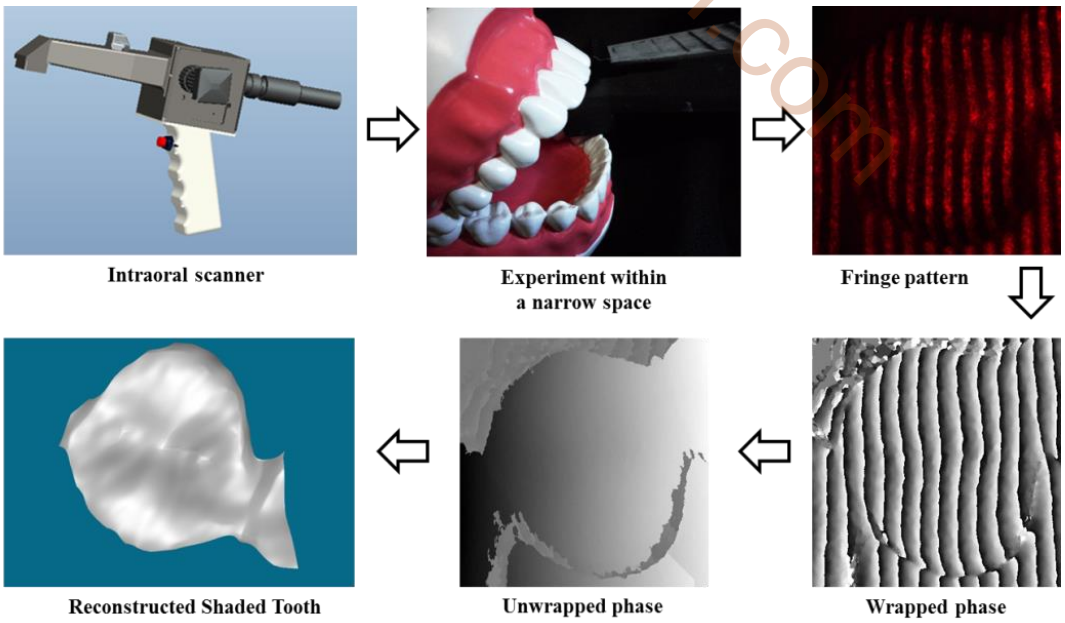

Fig. 56: Reconstruction results of 3D intraoral dental profile measurement within a narrow space

Light Source: For better results in the fringe projection technique, fringe patterns must be cleared and noise free, but in case of a microscale hardware it may difficult to control

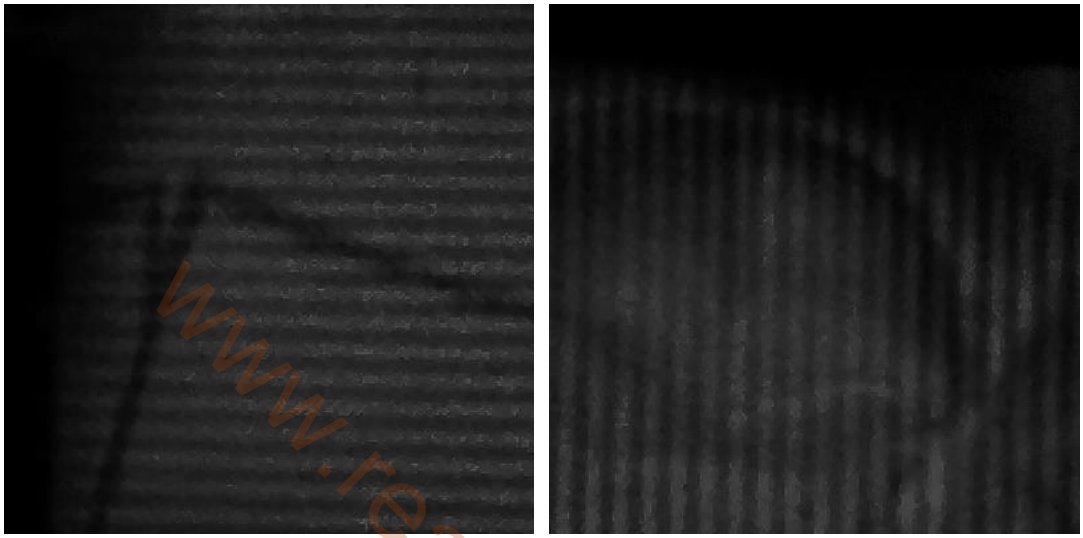

Fig. 57: Captured fringe pattern images using the 1st IOS device

Fig. 58: 1st IOS device on a fixed platform

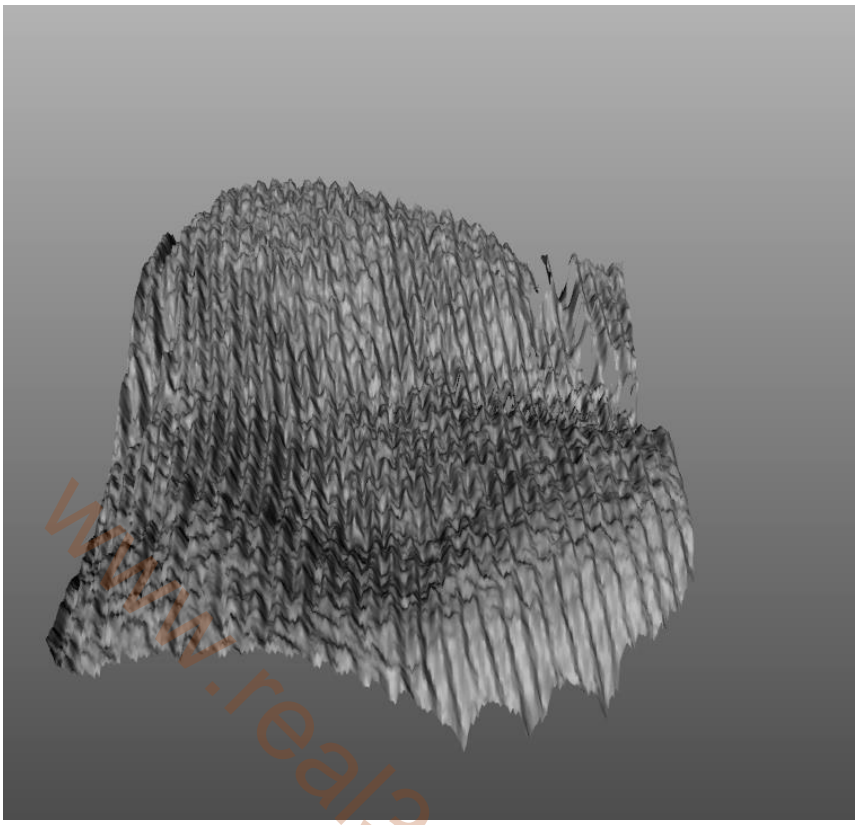

Fig. 59: Optical measurement results of a tooth shape with inaccurate phase-shifts

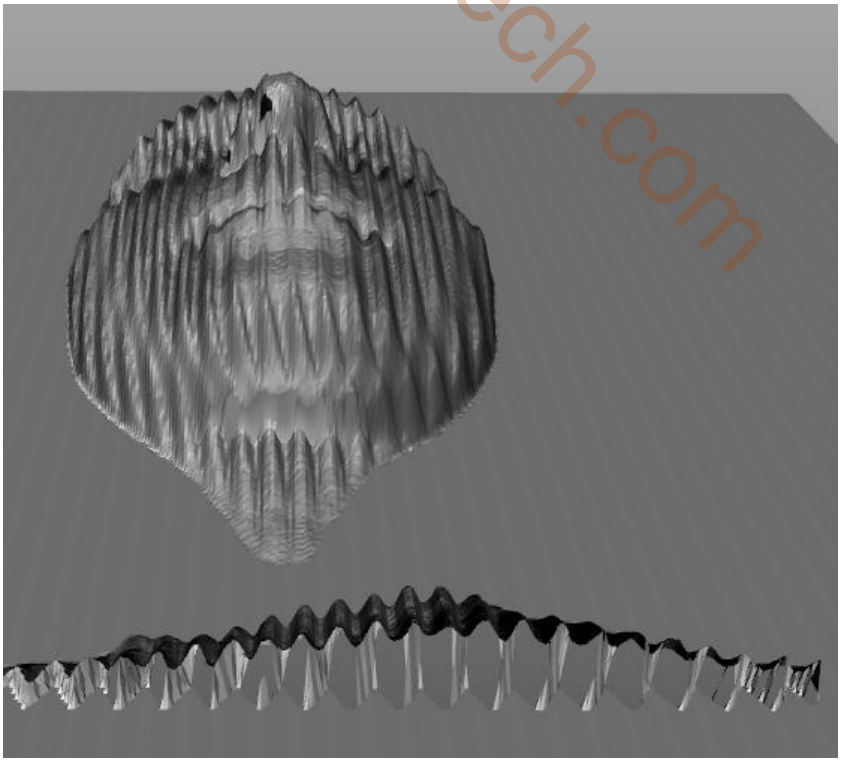

Fig. 60: Simulation results with the same setup of Fig. 39

supplied voltage to laser which create some random noise in the image. As a result, the object cannot be illuminated well and desired results cannot be achieved. Fig. 57 shows fringe pattern images which was captured during the test of the 1st IOS device. In order to overcome this issue, laser and its control was carefully analyzed and upgraded in the 2nd IOS device.

Camera Control: In order to get high quality and fast capturing of fringe pattern images, camera must be fast, high quality lenses must be used, and focus of the camera must be controllable. Incorrect focus and low quality lenses may lead to some worse results. On the software side, camera control must be properly configured in term of sharpness, gamma, brightness, contrast, and auto-exposure. In our observation, camera calibration is also a hard and time consuming process because if brightness or focus of the camera is changed, we may need to perform again the whole calibration process and configuration of the camera parameters.

PZT: The results presented in the above section were achieved with a fixed system setup which means that the device and the object were still and fixed at one platform as shown in Fig. 58. This is because of PZT sensitivity to gravity force. PZT moves the grating in too and fro motion and if the PZT angle is changed where it needs to move up and down, it stucks and does not move further. Improper supplied voltage to PZT might be an issue. So, in our observation, the core function in the fringe projection profilometry performs by the PZT which is accurate phase-shifts, however it is very difficult to obtain accurate linear phase-shifts with a non-linear device. An example is presented in Fig. 59 in which scanned surface of the tooth profile is shows with saw tooth like jumps in the image. The same situation is simulated in our virtual scanner with the same fringe pitch and found the same saw tooth like jumps as shows in Fig. 60. We observed that it is very difficult to solve all

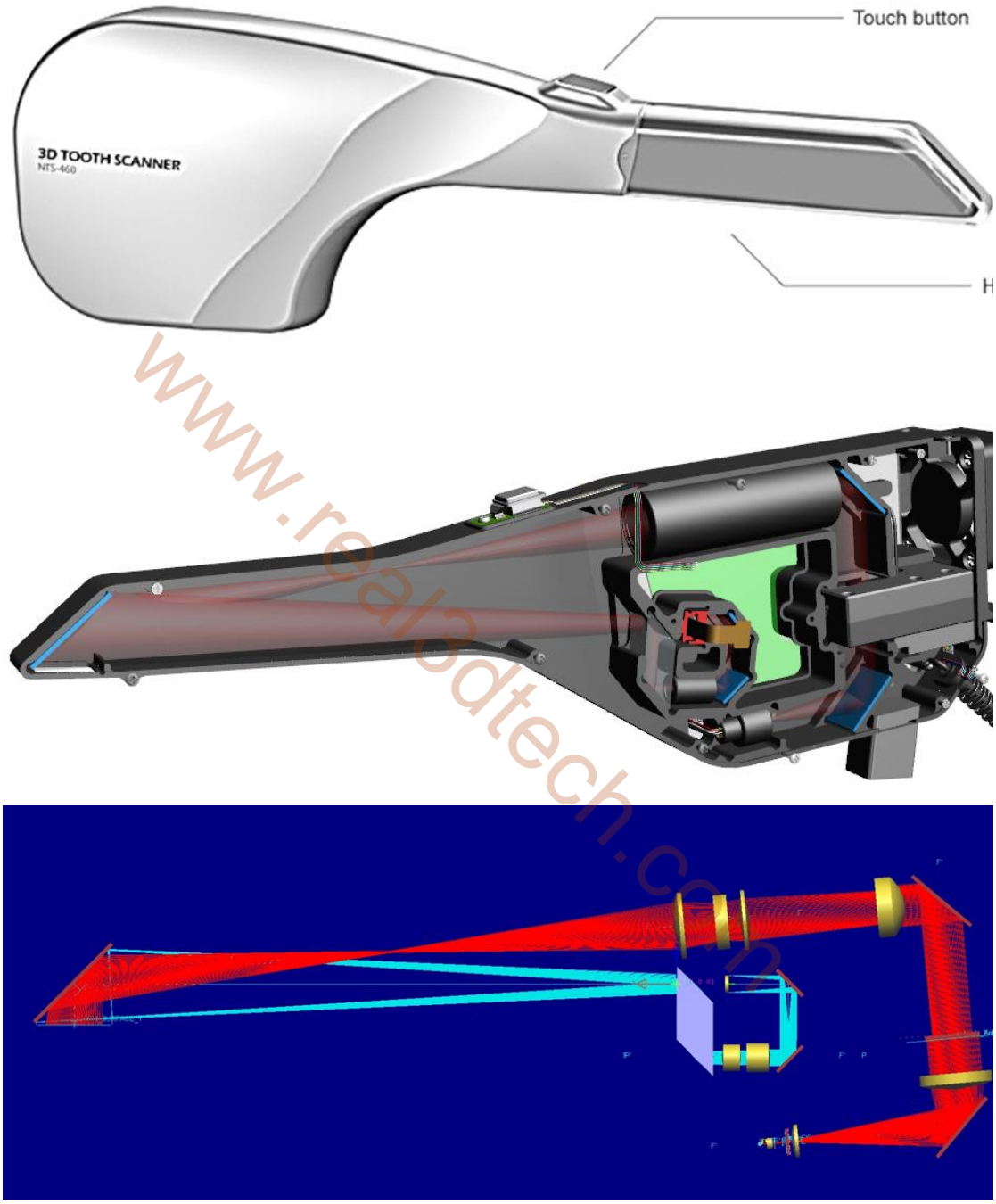

Fig. 61: CAD and optical design of the final IOS device

the issues relevant to PZT such as calibration, stability, sensitivity, jammed situation, improper voltages, etc. Therefore, in the 2nd version of the IOS device the PZT is replaced with a AVM-Series VCA which is more stable and accurate than the PZT.

Grating: Use of grating with wrong pitch of the fringe patterns may also lead to wrong direction. We have performed several experiments with grating fringe pitch of 200 mm, 298 mm, 300 mm, 400 mm, 500 mm, and 600 mm. Small fringe pitch can produce the high resolution with more detailed point cloud data, however a small error in the phase-shifts create large changes in the scanned data, and there may be impossible to remove the random noise from the image without disturbing the fringe patterns in the image. From experiments, we found that the grating fringe with pitch width 400 mm produces more accurate results and we have adopted it in the 3rd version of the IOS device.

Based on the observation from the first IOS device, we designed the second version of the IOS device with completely a new idea in term of hardware. In the second version most of the issues were resolved that were creating problems in accuracy of the scanned data. However, there were still some issues in the second version, therefore, much improved version of the IOS device was developed which will be discussed in the next sections.

6.3 Improved IOS Device

The third and final version of the IOS device was designed with some improvements such as hardware temperature control, visible high power LED as a new light source, and angle between the sensor and laser ray. The LED is a HL6501MG 0.65 μm band AlGaInP laser diode with a multi-quantum well (MQW) structure. The CAD and optical design of the final IOS device can be illustrated in Fig. 61. In this version, the probe height is little increased from 20 mm to 23 mm due to increasing the angle between sensor and laser ray

from 5^{o} to 10^{o} degree. Now, the probe which has to be inserted into the mouth becomes about 19.50 × 23 mm and a length of 83.01 mm.

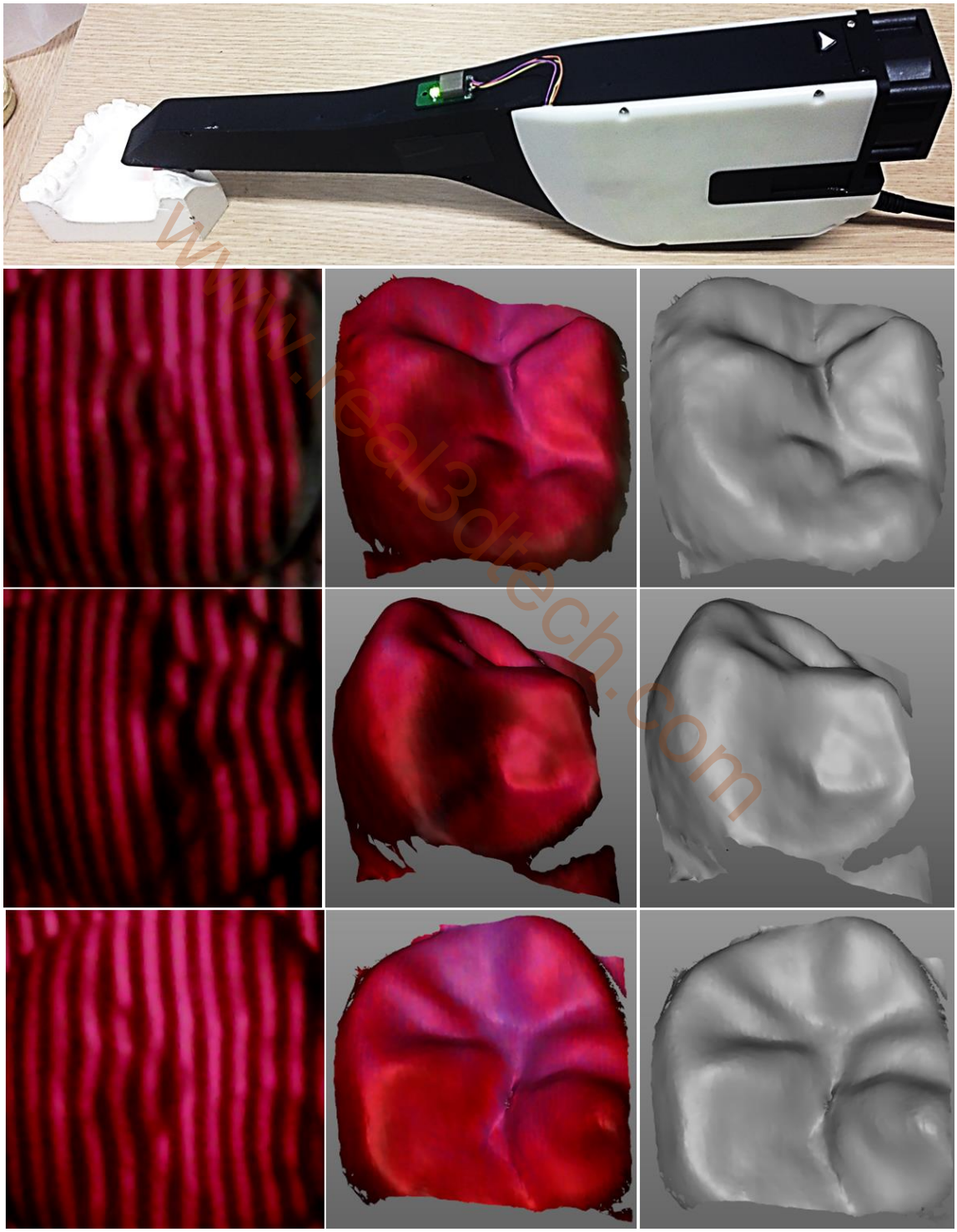

Fig. 62: Hardware of the final IOS device and optical measurement results

Optical experiments have been carried out onto various tooth models and results are demonstrated in Fig. 62, which shows one of the fringe patterns and the reconstructed 3D shapes with texture and without texture. The reconstruction accuracy of this version is reasonable with the overall stability of the device, particularly graticule movement through VCA. The four images were captured in 0.5 sec and one sample scan was obtained in <1 sec. The measurement procedure is based on point-and-click system in which the 3D surfaces should be scanned with at least a one-third overlap of the adjoining surface. The registration of the neighboring surfaces will then occur on the basis of overlap surfaces. In order to perform multiple scans for measuring the full jaw, we developed an auto-robot-arm that performs the intraoral scanning automatically. The implementation of the scanning process can be realized in Fig. 63 that depicts a flow chart of the steps involved in 3D scanning using 3rd IOS device.

6.4 Articulated Robot Arm

The description of the articulated robot arm is as follows:

When a dentist conducts 3D measurement by holding the intraoral scanner, the hand shaking could create unexpected results, and it could also be harmful for the dental patient. Therefore, it is needed to develop an automatic system that should perform the scanning operation automatically.

In order to scan a complete tooth profiles including occlusal, lip, and tongue, minimum two scans will be required from two different orientations as shown in Fig. 64 which describes the schematic diagram for articulated robot arm to perform intraoral scanning in the mouth cavity. Therefore, multiple scans should be performed from different views and all scans must be registered together in a common coordinate system.

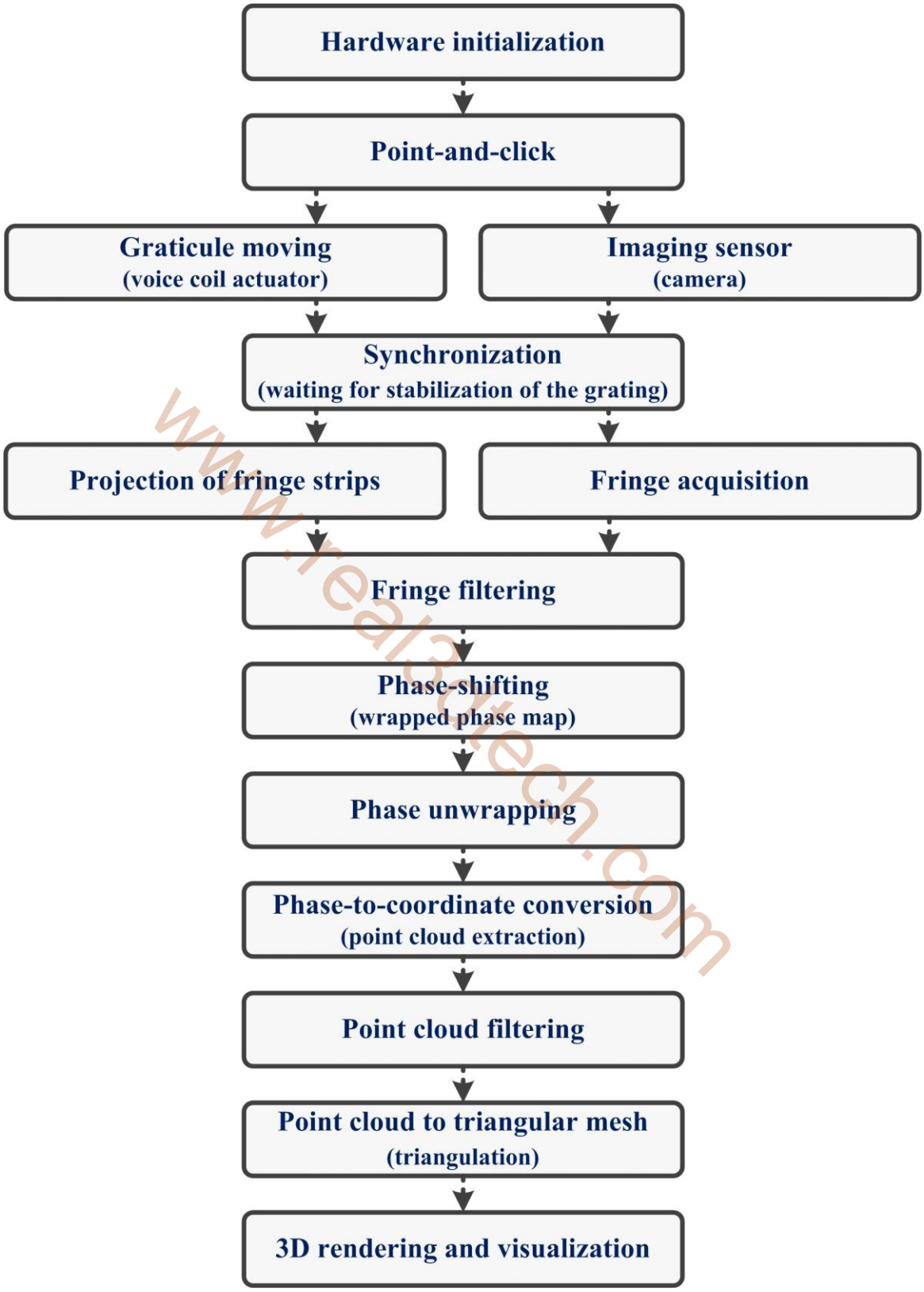

Fig. 63: IOS system: flow chart of the steps involved in 3D scanning using 3rd IOS device

On the basis of above assumptions, an articulated robot arm is developed which is very

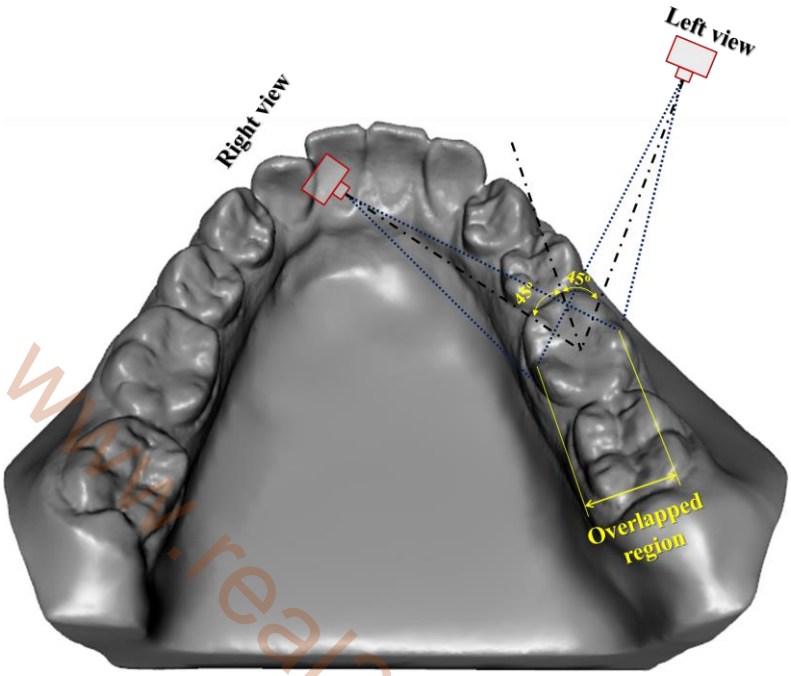

Fig. 64: Schematic diagram for articulated robot arm to perform intraoral scanning in the mouth cavity: two views of a tooth are captured from left and right orientations. The angle between two views is 45^{o} degree.

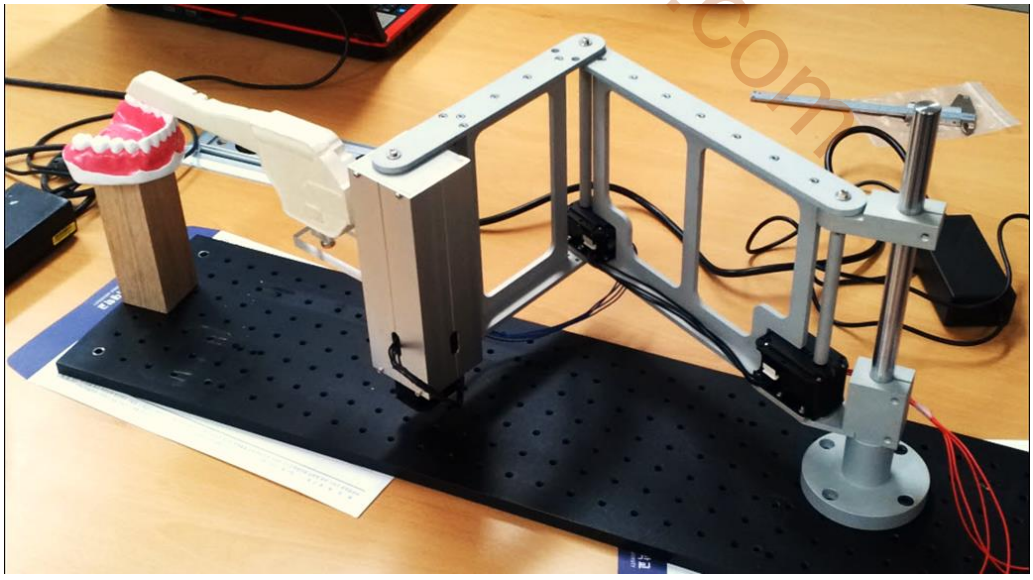

Fig. 65: Blue print and hardware of the articulated robot arm

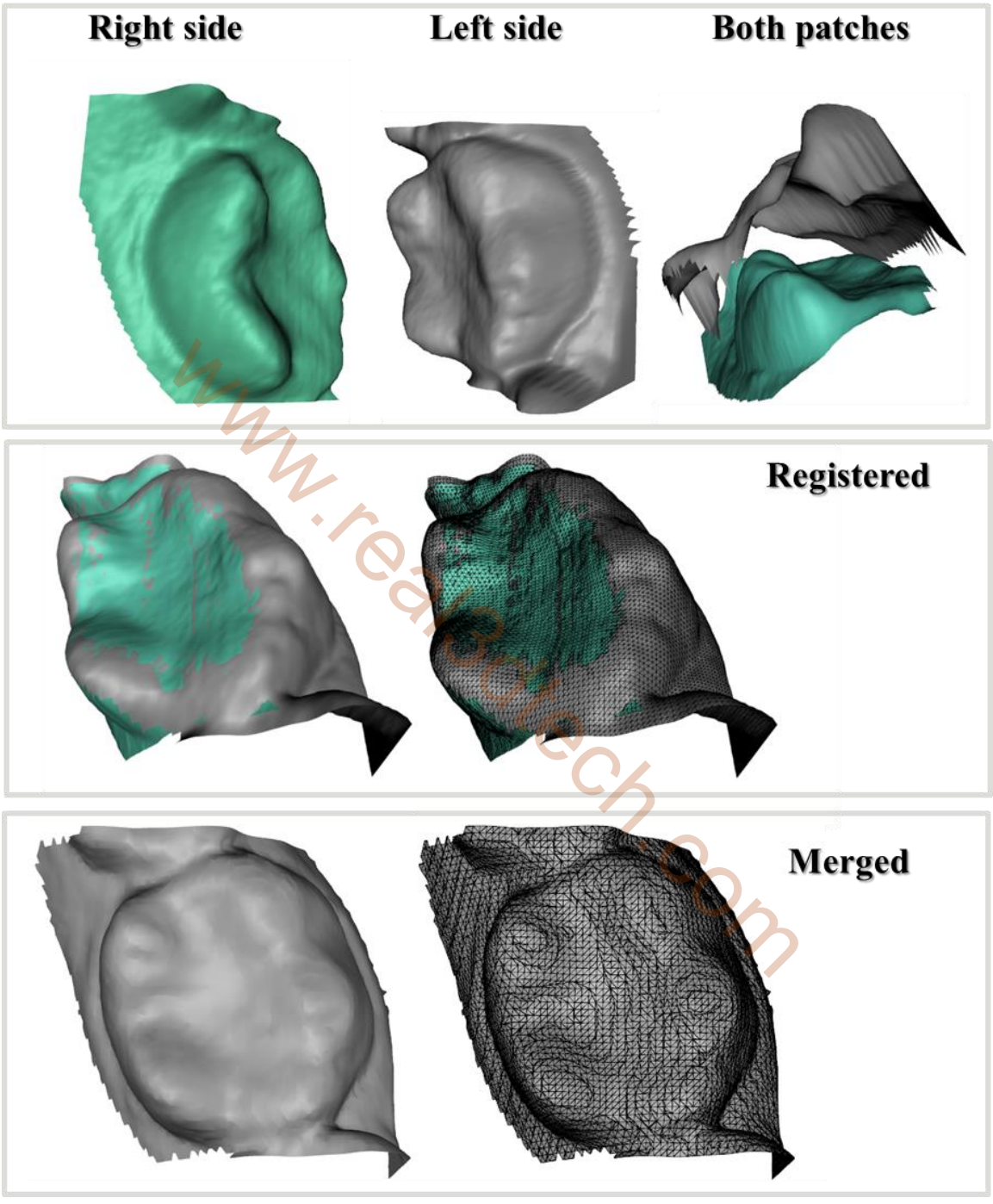

Fig. 66: Two surface patches of a tooth model is scanned from two views with 45^{o} degree angle, registered, and merged them in our virtual 3D scanner

similar to a 3-links robot arm. Fig. 65 shows the hardware of the 5-axis articulated robot

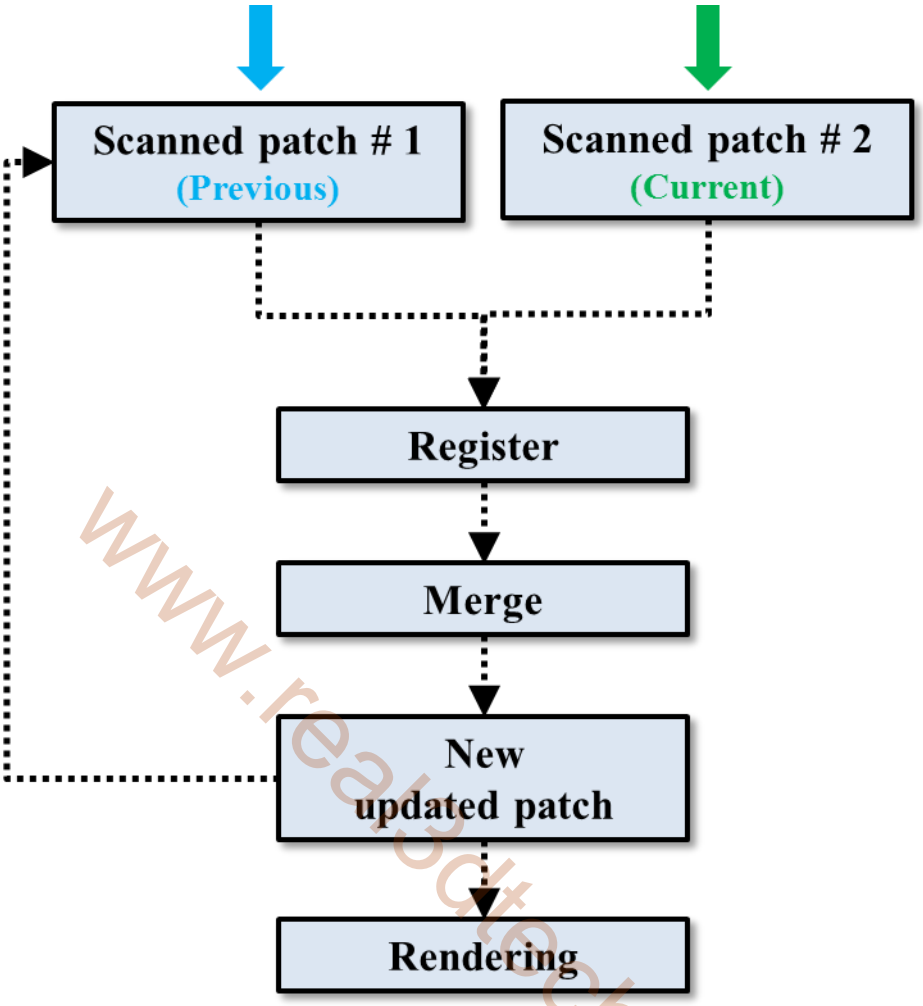

Fig. 67: Multi-patch scanning: flow chart of the multi-patches scanning with registration and merging

arm (4 axes for rotation and 1 axis for linear transformation). Since the robot arm uses motors for transformation, therefore, forward and inverse kinematics are needed to be calculated in order to know the position and poses of the scanner. Since the robot arm is in the developing stage and involves some issues such as stability, sensitivity, and accuracy of the device. However, the optical experiments are performed with the current condition of the device and are presented in the next section.

6.5 Registration and Merging

Articulated robot arm is used in order to transform the scanned point cloud data from camera coordinate system to common or global coordinate system which is important for the registration process. The robot arm will scan each tooth minimum two times from two different views because 1/3 area should be overlapped for the registration algorithm.

First, virtual simulation is performed using the same setup and captured two views from left and right side of the tooth model and performed registration and merging on both surface patches in order to test and verify the algorithms. The virtual experimental results can be seen in Fig. 66. After that, optical experiments have been carried out onto the dental models using the 3rd IOS device and the robot arm. The robot arm points intraoral scanner's probe-end to the desired tooth and rotates 45^{o} degree to capture the left and right views of the tooth profile. Since, the robot arm is in the developing stage and several issues involved in the process of capturing multi-patches, therefore, future research should focus on the multi-patches registration by using the articulated robot arm.

The implementation of the multi-patches scanning is presented in Fig. 67 that describes a flow chart of the steps involved in the multi-patches scanning with registration and merging processes.

6.6 Summary

In this chapter, the development of a 3D intraoral scanning system has been presented. The experimental results show that the developed system is capable of performing microscale measurements and can be applied to various applications. However, the calibration of the PZT for accurate phase shifts is a critical and challenging issue if good measurement results are to be obtained using PSI. Therefore, PZT was replaced in the 2nd

and 3rd device with a VCA in order to obtain more accurate phase shifts and stabilize movement of the graticule. 2nd and 3rd versions of the IOS device were developed based on the observation from the 1st IOS device. In the second version most of the issues were resolved that were creating problems in accuracy of the scanned data. However, there were still some issues in the second version, therefore a 3rd IOS device was developed that solved most of the scanning issues. In order to perform multiple scans for measuring the full jaw, a 5-axis articulated robot arm is developed that performs the intraoral scanning automatically. Furthermore, the proposed phase-to-coordinate conversion method based on collimating illumination for calculating the x, y, and z coordinates of the object profile was tested. The proposed method corrects the shape tilting issue based on a nonlinear phase-to-coordinate relation under collimating illumination. In addition, Table 2 can be considered for the short comparison between some existing intraoral scanners.

Table 2 Comparison of intraoral scanners

Intraoral Scanner	Working Principle	Illumination Source	Imaging Type	Coating	Output Format	Commercially available
CEREC™	Active triangulation and confocal microscopy	Visible blue light	Multiple images	Yea	Landlord	Available
Lava™	Active wavefront sampling	Pulsating visible blue light	Video	Yes	Landlord	Available
IOS FastScan	Active triangulation and Schleimpflug principle	Laser	3 images	Yes	STL	Not available
Densys3d	Active Stereophotogrammetry	Visible light	2 images	Not disclosed	ASCII	Not available
DPI-3D	Accordion fringe interferometry (AFI)	Two point source laser	Multiple images	None	Not disclosed	Not available
Our Scanner	Fringe pattern interferometry	Single point source laser	4 images	Yes	STL	Not available

Chapter 7. Conclusions

This dissertation presents two mathematical system models Case-3 and Case-4 for SMFP for calculating the x, y, and z coordinates of the object profile. The new models give more accurate mathematical representation of the systems, thus improving the shape measurement accuracy. The proposed models correct the shape tilting issue based on a nonlinear phase-to-coordinate relation under collimating illumination, and provide a rigorous theoretical base for the practical applications of fringe projection profilometry. Virtual and optical measurements are performed in order to verify the performance of the models and results are also presented which show that the proposed models can have better reconstruction accuracy under collimating illumination.

This dissertation presents a detailed development procedure of a 3D intraoral scanner based on structured light fringe projection technology. Three IOS devices were developed with different hardware. In the first device, PZT was utilized in order to move the graticule for phase shifting. Second device replaced PZT with the VCA in order to obtain accurate phase shifts as well as gain the stability of the device. Third device was the improved version of the second hardware in term of design, specifications, and accuracy. A complete flow of methods and algorithms were discussed that involved in the development of an IOS device. From measurement results, it can be concluded that the developed system and adopted methodology are effective in obtaining 3D surface profiles in a microscale environment.

This dissertation presents a development procedure of a SMDFP system which is capable of performing small and large scale measurements in real-time and can be applied to

various applications. The measurement method can be switched between various phase-shifting methods such as 3-Step, 4-Step, and 5-Step, and it can be easily extended to 11 or 18 images in order to achieve high accurate results. The system uses only a one camera and a projector which can be a very effective low cost 3D SMDFP system for many industrial applications.

This dissertation presents a real-time virtual 3D scanner based on DFP which will be very effective in the future development of new algorithms, and performance analysis of new 3D shape measurement systems. A detailed development procedure for the development of RTV3DS is discussed and results are also presented. Various algorithms for phase-shifting, phase unwrapping, phase-to-coordination, etc. are added in the system and can be easily extended in the future.

The important contribution of this dissertation is the development of a 3D scanning software which is capable of performing 3D virtual and optical scanning in real-time, and also an extensible points and mesh processing system. Many algorithms relevant to 3D scanning was written and added to the software that will be very advantageous for the future research on the development of 3D shape measurement systems.

3D shape measurement is becoming increasingly important in many industrial applications, e.g. precision shape measurement for production control, reverse engineering, volume measurement, skin surface measurement for cosmetics and medicine, body shape measurement, intraoral dental measurement, forensic science inspections, microscale measurements, and entertainment, etc. The research results reported in this dissertation can be used to develop new methods, algorithms, and improve the performance of existing 3D shape measurement systems to ensure their wide spread use in industry.

The new mathematical models presented in this dissertation provide a rigorous theoretical base for the practical applications of fringe projection profilometry, thus improving the shape measurement accuracy.

There are not so many 3D profile measurement tools designed specifically for tooth profiles, and due to the restrictions of size and volume on the 3D scanner for dental applications, it was not easy to perform non-contact profile scanning in the mouth cavity. This dissertation presented a detailed development procedure of a 3D intraoral scanning device that could solve some of the issues associated with cast production, and it could also provide a digital workflow with digital output data. The presented intraoral scanner is a very effective addition in the industry of dentistry and we believe that this research will open a new way to develop such micro-scale devices.

This dissertation also presented a low-cost real-time 3D SMDFP system that uses only one camera and a projector, and can be applied to various industrial applications for small and large scale measurements. We believe that the low cost of the systems ensures the wide deployment of this technique in industry.

Improvement in IOS device: The calibration of the PZT or VCA for accurate phase shift is a critical and challenging issue if good measurement results are to be obtained using PSI. Therefore, future work should address the improvement of phase-shifter.

The hardware of the IOS device works fine for the current setup; however, there is still room for improvement in the device to achieve better performance.

The articulated robot arm designed for the automation intraoral dental scanning may not be a perfect solution for this task, therefore, it is desired to seek for other ideas and methods which are easier to develop, handle, and operate.

In this dissertation, a point-and-click IOS device is developed which may have some disadvantages over the video-scanners, therefore, in the future studies video-scanner should be developed that register multiple 3D images in real-time.

Improvement in SMDFP system: The developed system uses reference-subtraction approach in order to remove carriers for phase-to-coordinate conversion which is time consuming and not preferable for many situations. Therefore, it is desired to seek for other non-linear methods which should provide better performance and easiness in the calibration process.

In this dissertation, full body or 360^{o} shape information was not performed and discussed for SMDFP system; however, future work should focus on the new ideas and methods to develop such a system. There can be two ways, one is to rotate an object or a scanning device and the other is to use multiple systems. Both are challenging tasks for the future studies.

References

1. Gorthi, S. S., Rastogi, P., “Fringe projection techniques: whither we are?,” Opt. Lasers Eng. Vol. 48, pp. 133-140, 2010.
2. Mark L. Kimber, “Development of a Virtually Calibrated Projection Moiré Interferometry Technique Capable of Inaccessible Surface Measurements,” 2004.
3. Huntley, J. M., "Optical shape measurement technology - past, present, and future," Proc. SPIE 4076, pp. 162-173, 2000.
4. Chen, L., Huang, C., “Miniaturized 3D surface profilometer using digital fringe projection,” Meas. Sci. Techn. Vol. 16, No. 5, pp. 1061-1068, 2005.
5. Moore, C. J., Burton, D. R., Skydan, O., Sharrock, P. J., Lalor, M., “3D body surface measurement and display in radiotherapy part I: Technology of structured light surface sensing,” Proc. Int. Confe. Medical Information Visualisation - BioMedical Visualisation (1691277), pp. 97-102. 2006.
6. Chen, X., Xi, J. t., Jiang, T., Jin, Y., “Research and development of an accurate 3D shape measurement system based on fringe projection: Model analysis and performance evaluation”, Precision Engineering, Vol. 32, pp. 215–221, 2008.
7. Zhang, S., “Recent progresses on real-time 3D shape measurement using digital fringe projection techniques,” Opt. Lasers Eng. Vol. 48, pp. 149–158, 2010.
8. Furqan U., Gun S. L., Kang P., “Development of a Real-time 3D Intraoral Scanner based on Fringe-Projection Technique,” Transactions of the Society of CAD/CAM Engineers, Vol. 17, No. 3, pp.156-163, 2012.
9. Furqan U., Gun S. L., Kang P., “Analysis and Performance Comparison of 3D Measurement Systems based on Fringe Projection Profilometry,” 2012 International Conference on Information Science and Applications, pp. 62-67, 23-25 May 2012.

10. Shouhong T., Tucson, AZ., “Non-linear phase shift calibration for interferometric measurement of multi surfaces,” US Patent No. 6856405 B2, Feb. 15, 2005.
11. Hui D., Xiangnan W., Jianqi L., Xianli L., “Online calibration of PZT driven fiber Fabry–Perot filter nonlinearity using FBG array and PSO algorithm,” Measurement, Vol. 42, pp. 1059-1064, 2009.
12. Yeou Y., Cheng and James C. Wyant, “Phase shifter calibration in phase-shifting interferometry,” Applied Optics, Vol. 24, No. 18, 1985.
13. K. Kinnstaetter, A. W. Lohmann, J. Schwider, and N. Streibl, “Accuracy of phase shifting interferometry,” Appl. Opt. 27, 5082–5089, 1988.
14. C. P. Brophy, “Effect of intensity error correlation on the computed phase of phase-shifting interferometry,” J. Opt. Soc. Am.A7, 537–541, 1990.
15. L. A. Selberg, “Interferometer accuracy and precision,” in Optical Fabrication and Testing, D. R. Campbell, C.W. Johnson, and M. Lorenzen, eds., Proc. Soc. Photo-Opt. Instrum. Eng.1400, 24–32, 1990.
16. P. de Groot, “Predicting the effects of vibration in phase shifting interferometry,” in Optical Fabrication and Testing Workshop, Vol. 13. of 1994 OSA Technical Digest Series-1 Optical Society of America, Washington, D.C., 19942, pp. 189–192.
17. Rusinkiewicz, S., Hall-Holt, O., Levoy, M., “Realtime 3D model acquisition,” In Proceedings of Siggraph, pp. 438-446, July 2002.
18. Huang, P. S., Zhang, C., Chiang, F., “High-speed 3-D shape measurement based on digital fringe projection,” Opt. Eng. Vol. 42, No. 1, pp. 163-168, 2003.
19. Guan, C., Hassebrook, L. G., Lau, D. L., “Real-time 3-D data acquisition for augmented reality man and machine interfacing,” Visualization of Temporal and Spatial Data for Civilian and Defense Applications V, SPIE’s AeroSense, Vol. 5097,

A-5, 2003.

20. Koninckx, T. P., Gool, L. V., “Real-time range acquisition by adaptive structured light,” IEEE Trans. Pattern Analy. Mach. Intell., Vol. 28, No. 3, pp. 432-445, 2006.
21. Breuckmann, B., Halbauer, F., Klaas, E., Kube, M., “3D-metrologies for industrial applications,” In Proceedings of SPIE 3102, pages 20–29, 1997.
22. Wicher, J., Meer, V. D., Andriessen, F. S., Wismeijer, D., Ren, Y., “Application of Intra-Oral Dental Scanners in the Digital Workflow of Implantology,” PLoS ONE, Vol. 7, No. 8, August 2012.
23. Riehemann, S., Palme, M., Kuehmstedt, P., Grossmann, C., Notni, G., Hintersehr, J., “Microdisplay-Based Intraoral 3D Scanner for Dentistry,” Journal of Display Technology, Vol. 7, No. 3, pp. 151-155, 2011.
24. Hart DP., Lammerding J., Rohaly J., “ 3-D Imaging System,” US Patent 2004/0155975 A1, Aug 12, 2004.
25. Trissel RG., “Polarizing multiplexer and methods for intra-oral scanning,” US Patent 2007/0047079 A1, Mar 01, 2007.
26. Ernst MM., Neta U., Cohen C., Geffen M., “Three-dimensional modeling of the oral cavity,” US Patent 2008/0273773 A1; Nov 6, 2008.
27. Dillon RF., Zhao B., Judell NHK., “Intra-oral three-dimensional imaging system,” International Publication WO 2009/058656 A1, May 7, 2009.
28. Silvia L., Giordano F., Ari K., Michele C., Lapo G., Luciano B., “A Comparative Analysis Of Intraoral 3d Digital Scanners For Restorative Dentistry,” The Internet Journal of Medical Technology, Vol. 5, No. 1, 2011.
29. E. Hu and Y. He., “Surface profile measurement of moving objects by using an improved π phase-shifting Fourier transform profilometry,” Optics and Lasers in

Engineering, 47(1):57-61, 2009.

30. M. T. K. Takeda M, Mutoh, “Fourier transform profilometry for the automatic measurement of 3-D object shapes,” Appl. Opt, 22:3977–3982, 1983.
31. H. M. Yue, X.Y. Su, and Y.Z. Liu. “Fourier transform profilometry based on composite structured light pattern,” Optics and Laser Technology, 39(6):1170–1175, 2007.
32. L. Zhang, B. Curless, and SM Seitz. “Rapid shape acquisition using color structured light and multi-pass dynamic programming,” In 3D Data Processing Visualization and Transmission, 2002. Proceedings. First International Symposium on, pages 24–36, 2002.
33. J. H. Bruning, D. R. Harriott, J. E. Gallagher, D. P. Rosenfeld, A. D. White, D. J. Brangaccio, “Digital wavefront measuring interferometry for testing optical surfaces and lenses,” Appl. Opt. 13, 2693 (1974).
34. Wyant, J. C., “Phase-Shifting Interferometry,” Technical Report. Optical Sciences Center, University of Arizona, 1998.
35. Buckland, J. R., Huntley, J. M., and Turner, J. M., (1995), “Unwrapping noisy phase maps by use of a minimum-cost-matching algorithm,” Applied Optics, vol. 34, pp. 5100-5108.
36. Chavez, S., Xiang, Q. and An, L., (2002), “Understanding phase maps in MRI: a new cutline phase unwrapping method,” IEEE Transactions on Medical Imaging , vol. 21, no. 8, pp. 966-977.
37. Chen, C. and Zebker, H., (2000), “Network approaches to the two-dimensional phase unwrapping: intractability and two new algorithms,” Applied Optics, vol. 17, pp. 401-414.

38. Cho, B., (2004), “Quality map extraction for radar interferometry using weighted window,” Electronic Letters, vol. 40, no. 8.

39. Collaro, A., Fornaro, G., Franceschetti, G., Lanari, R., Sansosti, E. and Tesauro, M., (1997), “Local, global and unconventional phase unwrapping techniques,” 1997 International Geoscience and Remote Sensing Symposium. Remote Sensing - A Scientific Vision for Sustainable Development, pp. 433-435.

40. T., (1996), “Consistent 2-D phase unwrapping guided by a quality map,” in IEEE Proceeding of the 1996 International Geoscience and Remote Sensing Symposium, Lincoln, vol. 4, pp. 2057-2059.

41. Flynn, T., (1997), “Two-dimensional phase unwrapping with minimum weighted discontinuity,” Applied Optics, vol. 14, pp. 2691-2701.

42. Fornaro, G. and Franceschetti, G., (1995), “Two dimensional phase unwrapping based on the Laplace and Eikonal equations,” 1995 International Geoscience and Remote Sensing Symposium, IGARSS '95. Quantitative Remote Sensing for Science and Applications, vol. 3, pp. 1828-1830.

43. Fornaro, G., Franceschetti, G. and Lanari, R., (1996), “Interferometric SAR phase unwrapping using Green’s formulation,” IEEE Transaction Geoscience Remote Sensing, vol. 34, pp. 720–727.

44. Fornaro, G., Franceschetti, G., Lanari, R., Sansosti, E., and Tesauro, M., (1997), “Global and local phase-unwrapping techniques: a comparison,” Applied Optics, vol. 14, No. 10, pp. 2702-2708.

45. Ghiglia, D. C. and Romero, L. A., (1994), “Robust two-dimensional weighted and unweighted phase unwrapping that uses fast transforms and iterative methods,” Applied Optics, vol. 11, no. 1, pp. 107-117.

46. Ghiglia, D. C., and Romero, L. A., (1996), “Minimum L^p-norm two-dimensional phase unwrapping,” Applied Optics, vol. 13, No. 10, pp. 1999-2013.
47. Xu, W. and Cumming, I., (1996), “A region growing algorithm for InSAR phase unwrapping,” Proceedings of the 1996 International Geoscience and Remote Sensing Symposium, Lincoln, NE, May 27-31, IEEE, pp. 2044-2046.
48. 3. M. Arevalillo Herráez, D. R. Burton, M. J. Lalor and M. A. Gdeisat, “A Fast two dimensional phase unwrapping algorithm based on sorting by reliability following a non-continuous path,” Applied Optics, Vol. 41, No. 35, pp 7437-7444, 2001.
49. K. Itoh, “Analysis of the phase unwrapping problem,” Applied Optics, Vol. 21, No. 14, p. 2470, July 15, 1982.
50. Dennis Ghiglia and Mark Pritt, “Two-dimensional phase unwrapping theory,” algorithms and applications, John Wiley & Sons, 1998.
51. Quan, C., Tay, C. J., Chen, L. J., “A study on carrier-removal techniques in fringe projection profilometry,” Optics and Laser Technology Vol. 39, No. 6, September, 2007. p. 1155-1161.
52. Li J. L, Su X. Y, Su H. J, Cha S. S. “Removal of carrier frequency in phase-shifting techniques,” Opt Lasers Eng 1998; 30: 107-15.
53. Srinivasan V, Liu HC, Halioua M. “Automated phase-measuring profilometry: a phase mapping approach,” Appl Opt 1985, 24, 185-8.
54. Chen L, Quan C. “Fringe projection profilometry with nonparallel illumination: a least-squares approach,” Opt Lett. 2005, 30, 2101-3.
55. Chen L, Tay CJ. “Carrier phase component removal: a generalized least-squares approach,” J Opt Soc. Am A 2006, 23, 435-43.
56. Srinivasan, V., Liu, H. C., Halious, M., “Automated phase-measuring profilometry of

3-D diffuse objects," Appl Opt 1984, 23, 3105-8.

57. C. Quan, X. Y. He, C. F. Wang, C. J. Tay, and H. M. Shang. "Shape measurement of small objects using LCD fringe projection with phase shifting. Optics Communications," 189(1–3):21–29, 2001.
58. Takeda M, Ina H, Kobayashi S., "Fourier-transform method of fringe pattern analysis for computer-based topography and interferometry," J Opt Soc Am 1982;72:156–60.
59. W. Schreiber, G. Notni, "Theory and arrangements of self-calibrating whole-body three-dimensional measurement systems using fringe projection technique," Opt. Eng. 39 (1) (2000) 159–169.
60. Y. Y. Hung, L. Lin, H. M. Shang, B. G. Park, "Practical three-dimensional computer vision techniques for full-field surface measurement," Opt. Eng. 39 (1) (2000) 143–149.
61. H. Liu, W. Su, K. Reichard, S. Yin, "Calibration-based phase-shifting projected fringe profilometry for accurate absolute 3D surface profile measurement," Opt. Commun. 216 (1-3) (2003) 65–80.
62. X. Zhang, Y. Lin, M. Zhao, X. Niu, Y. Huang, "Calibration of a fringe projection profilometry system using virtual phase calibrating model planes," J. Opt. A: Pure Appl. Opt. 7 (4) (2005) 192–197.
63. L. Zhongwei, S. Yusheng, W. Congjun, W. Yuanyuan, "Accurate calibration method for a structured light system," Opt. Eng. 47 (5) (2008) 053604.
64. R. Anchini, G. Di Leo, C. Liguori, A. Paolillo, "A new calibration procedure for 3-D shape measurement system based on phase-shifting projected fringe profilometry," IEEE Trans. Instrumentation and Measurement 58 (5) (2009) 1291–1298.
65. E. Zappa, G. Busca, "Fourier-transform profilometry calibration based on an

exhaustive geometric model of the system," Opt. Laser Eng. 47 (7-8) (2009) 754–767.

66. X. Chen, J. Xi, Y. Jin, J. Sun, "Accurate calibration for a camera-projector measurement system based on structured light projection," Opt. Laser Eng. 47 (3-4) (2009) 310–319.
67. Z. Wang, H. Du, H. Bi, "Out-of-plane shape determination in generalized fringe projection profilometry," Opt. Express 14 (25) (2006) 12122-12133.
68. H. Du, Z. Wang, "Three-dimensional shape measurement with an arbitrarily arranged fringe projection profilometry system," Opt. Lett. 32 (16) (2007) 2438–2440.
69. X. Mao, W. Chen, X. Su, "Improved Fourier-transform profilometry," Appl. Opt. 46 (5) (2007) 664–668.
70. D. Feipeng, G. Shaoyan, "Flexible three-dimensional measurement technique based on a digital light processing projector," Appl. Opt. 47 (3) (2008) 377–385.
71. T. A. Clarke and J. G. Fryer. "The development of camera calibration methods and models. Photogrammetric Record," 16(91):51–66, 1998.
72. J. G. Fryer and D. C. Brown. "Lens distortion for close-range photogrammetry. Photogrammetric Engineering and Remote Sensing," 52(1):51–58, 1986.
73. J. Salvi, X. Armangu´e, and J. Batlle. "A comparative review of camera calibrating methods with accuracy evaluation. Pattern Recognition," 35(7):1617–1635, 2002.
74. Besl, P., Mckay, N., "A Method for Registration of 3-D Shapes," Trans. PAMI, Vol. 14, No. 2. 1992.
75. D. A. Field, "Laplacian smoothing and delaunay triangulations," Communications in Numerical Methods in Engineering, vol. 4, pp. 709–712, 1988.
76. [4] J. Vollmer, R. Mencl, and H. M¨uller, "Improved laplacian smoothing of noisy surface meshes," Computer Graphics Forum, vol. 18, no. 3, pp. 131–138, 1999.

77. M. Desbrun, M. Meyer, P. Schr¨oder, and A. H. Barr., “Implicit fairing of irregular meshes using diffusion and curvature flow,” Proceedings of ACM SIGGRAPH 99, pages 317–324, 1999.

78. L. Kobbelt, S. Campagna, J. Vorsatz, and H.-P. Seidel., “Interactive multiresolution modeling on arbitrary meshes,” In Proceedings of ACM SIGGRAPH 98, pages 105–114, 1998.

79. G. Taubin., “A signal processing approach to fair surface design,” In Proceedings of ACM SIGGRAPH 95, pages 351–358, 1995.

80. A. Belyaev and Y. Ohtake, “A comparison of mesh smoothing methods,” in Proceedings of Israel-Korea Bi-National Conference on Geometric Modeling and Computer Graphics, 2003, pp. 83–87.

81. Jones TR, Durant F, Desbrun M., “Non-iterative, feature-preserving mesh smoothing,” Proceedings of the 30th Annual Conference on Computer Graphics and Interactive Techniques, 2003; 943–949.

82. Fleishman S, Drori I, Cohen-Or D., “Bilateral mesh denoising,” Proceedings of the 30th Annual Conference on Computer Graphics and Interactive Techniques, 2003; 950–953.

83. Mao, Z., Ma, L., Zhao, M., Xiao, X., “SUSAN structure preserving filtering for mesh denoising,”, Vol. 22, No. 4, pp 276-284, April 2006.

84. Pfeiffer, J., Cerec 10 Year Anniversary Symposium (Chicago, IL: Quintessence), 1996.

85. Chen, L., Huang, C., “Miniaturized 3D surface profilometer using digital fringe projection,” Meas. Sci. Techn. Vol. 16, No. 5, pp. 1061-1068, 2005.

86. Riehemann, S., Palme, M., Kuehmstedt, P., Grossmann, C., Notni, G., Hintersehr, J., “Microdisplay-Based Intraoral 3D Scanner for Dentistry,” Journal of Display

Technology, Vol. 7, No. 3, pp. 151-155, 2011.

87. Hart DP., Lammerding J., Rohaly J., "3-D Imaging System," US Patent 2004/0155975 A1, Aug 12, 2004.
88. Trissel RG., "Polarizing multiplexer and methods for intra-oral scanning," US Patent 2007/0047079 A1, Mar 01, 2007.
89. Ernst MM., Neta U., Cohen C., Geffen M., "Three-dimensional modeling of the oral cavity," US Patent 2008/0273773 A1; Nov 6, 2008.
90. Dillon RF., Zhao B., Judell NHK., "Intra-oral three-dimensional imaging system," International Publication WO 2009/058656 A1, May 7, 2009.
91. Silvia L., Giordano F., Ari K., Michele C., Lapo G., Luciano B., "A Comparative Analysis Of Intraoral 3d Digital Scanners For Restorative Dentistry," The Internet Journal of Medical Technology, Vol. 5, No. 1, 2011.
92. ThorLabs, http://www.thorlabs.de/thorproduct.cfm?partnumber=DCC1645C. Accessed September 26, 2012.
93. Lanics Laser Electronics, http://www.lanics.com/products/diode-laser-dot.php. September 26, 2012.
94. Malacara, D., Servin, M., Malacara, Z., "Interferogram Analysis for Optical Testing," Second Edition. Taylor & Francis Group, 2005.
95. Greivenkamp, J. E., Bruning, J. H., "Phase Shifting Interferometry. Optical Shop Testing," Third Edition, D. Malacara, ed., (John Wiley, 2007), pp. 547–655, 2007.
96. Zhang, Z., "A flexible new technique for camera calibration," IEEE Trans. Pattern Anal. Vol. 22, pp. 1330–1334, 2000.
97. Huang PS, Hu Q, Jin F, Chiang F; "Color-encoded digital fringe projection technique for high-speed three-dimensional surface contouring," Opt. Eng. 0001;38(6):1065-1071.

98. Bernardini, F., Martin, I.M., Rushmeier, H., “High-quality texture reconstruction from multiple scans,” Visualization and Computer Graphics, IEEE Transactions on, vol.7, no.4, pp.318,332, Oct-Dec 2001.

99. B. Curless and M. Levoy., “A volumetric method for building complex models from range images,” In Proceedings of SIGGRAPH 96, ACM SIGGRAPH, Computer Graphics Proceedings, Annual Conference Series. pp. 303–312. August, 1996.

100. G. Turk and M. Levoy., “Zippered polygon meshes from range images,” In A. Glassner (ed), Proceedings of SIGGRAPH 94, Computer Graphics Proceedings, Annual Conference Series. pp. 311–318. July, 1994.

101. M. Soucy and D. Laurendeau., “A general surface approach to the integration of a set of range views,” IEEE Transactions on Pattern Analysis and Machine Intelligence, 17(4):344–358, April, 1995.

102. F. Bernardini, J. Mittleman, H. Rushmeier, C. Silva and G. Taubin., “The ball-pivoting algorithm for surface reconstruction,” IEEE Transactions on Visualization and Computer Graphics, 5(4):349–359, October-December, 1999.

103. M. Wheeler, Y. Sato and K. Ikeuchi., “Consensus surfaces for modeling 3D objects from multiple range images,” In Sixth International Conference on Computer Vision, IEEE. pp. 917–924. 1998.

104. A. Hilton, A. Stoddart, J. Illingworth and T. Windeatt., “Reliable surface reconstruction from multiple range images,” In Fourth European Conference on Computer Vision, pp. 117–126. 1996.

105. W. Lorensen and H. Cline., “Marching cubes: a high resolution 3D surface construction algorithm,” Computer Graphics, 21(4):163–170, 1987.

106. Lance Williams., “Casting curved shadows on curved surfaces,” In Proceedings of

SIGGRAPH ’78, pages 270-274, 1978.

107. Mark Segal and Kurt Akeley, “The OpenGL Graphics System: A Specification (Version 1.2.1),” www.opengl.org

Appendices

The important portion of the research work of this dissertation is to design and develop a computer software. The software is developed based on C/C++ object oriented, OpenCV, and OpenGL programming languages. The software is based on Windows GUI and can be executed on Microsoft Windows XP/Vista/7/8.1 operating systems. Several modules are developed inside of the system software such as real-time structured-light virtual 3D scanner and real-time structured-light optical scanning, etc. The scanning modules can perform coordinate acquisition, reconstruction, and display processes, simultaneously and quickly. In addition, the system has various functional modules such as system devices controlling, image processing and visualization, point cloud and triangular model visualization, points and mesh filtering and refinement, and post-processing, etc. Some features of the software include but not limited to:

1. General image Processing:
    - Import and export
    - Display
    - Noise reduction and smoothing filters
    - Color adjustment (brightness, contrast, equalize, etc.)
    - Resize
    - Rotate
    - Zoom in and zoom out
    - Filters for edge detection

2. General 3D Processing:

- Import and export of point clouds and triangular meshes
- 3D visualization with rotate, zoom, and pan using mouse and keyboard
- Point clouds and meshes filtering and smoothing
- Lightings and color adjustments
- Sectioning
- Translate, rotate, and scale
- Texturing
- Animation
- Mesh reconstruction, subdivision, smoothing, decimation, normal
- Point cloud and mesh registration
- Batch processing for more than one point clouds and meshes

3. General 3D measurement:

- Sinusoidal fringe pattern generation with any pitch and size
- Live camera capturing with 2D image processing
- Camera calibration

4. Simulation for real-time 3D scanning:

- Real-time 3D scanning using 3-step, 4-step, and 5-step phase shifting methods
- Phase unwrapping using quality-guided, flood-fill, multilevel, and linear algorithms
- Real-time 3D scanning with any image resolution
- Adjustable system parameters for camera, projector, and object

- Display of virtual scene from different angles
- Real-time visualization of reconstructed point cloud and mesh
- Various system models for collimating and non-collimating illumination
- Display and save wrapped, unwrapped, phase modulation, and color map images
- Real-time point cloud and mesh filtering
- Real-time reconstruction resolution adjustment
- Delay in real-time scanning
- Import of CAD/virtual objects
- Export of reconstructed point clouds and meshes

5. Real-time and Offline 3D scanning:

- Processing of 3-step, 4-step, and 5-step phase shifted images
- Unwrap the wrapped image
- Display and save the processed images
- Reconstruction of point clouds using various algorithms
- Point cloud to triangulation conversion with real-time visualization
- Real-time camera control
- Real-time projection of fringe patterns control
- 3D Reconstruction with and without reference plane
- Point-and-click scanning with multi-patches visualization
- Texture capturing and visualization
- Export of reconstructed point clouds and meshes

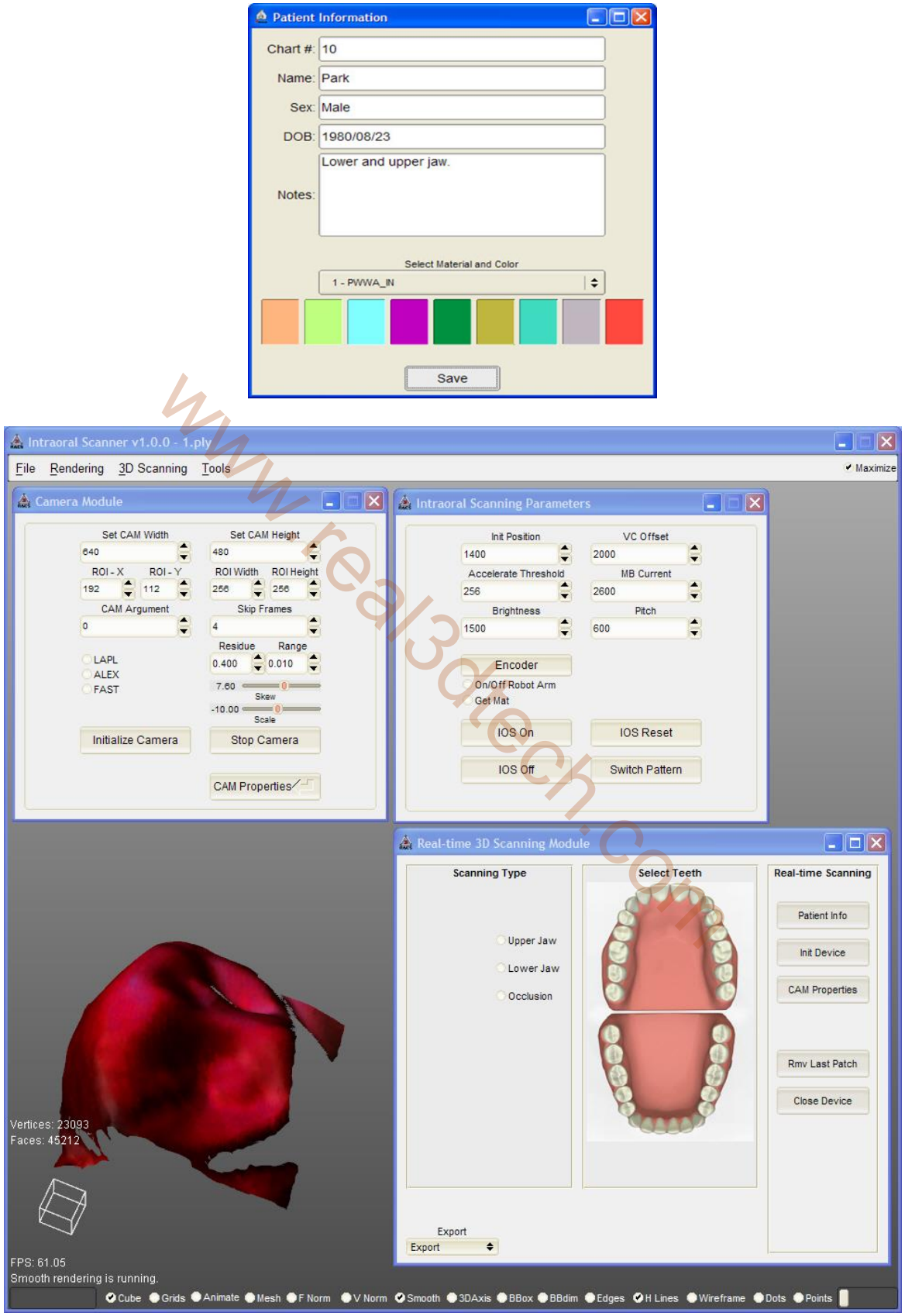

Fig. 68: Screenshots of IOS controls

The hardware of the IOS device is controlled by various parameters; therefore, specific modules are created in order to control the PZT and VC movement, LED power, illumination intensity, and camera, etc. Some screenshots of the GUI for the IOS device can be seen in Fig. 68.

프린지 투영법에 기초한 구강내 스캐너의 삼차원 형상 측정 분석

펄칸 울라

명지대학교 대학원 기계공학과

지도교수 박 강

최근에 3D 형상 측정은 많은 산업 분야에서 그 중요성이 증가되고 있다. 대표적인 3D 형상 측정 응용으로서는 생산제어, 역공학, 부피측정, 미용과 의학 응용을 위한 피부 면 측정, 구강내 치아 측정, 법의학 과학 조사, 마이크로 단위 측정, 연예오락분야 응용 등을 들 수 있다. 서로 다른 원리를 사용한 많은 3D 측정 시스템들이 개발되어 왔는데, 이들은 정확성, 분해능, 스피드, 스캐닝 효율 등에서 서로 다른 결과를 보여주고 있다. 많은 3D 측정 시스템들 중에 3D 프린지 투영법이 가장 널리 쓰이고 있는데, 3D 프린지 투영법이 가장 널리 쓰이는 이유는 실시간 측정이 가능하고, 빠르고, 유연하고, 강인하며, 정확하고, 높은 분해능을 가지고 있기 때문이다. 본 논문의 연구는 프린지 투영 측정법에 기초한 삼차원 측정 시스템의 분석에 관한 것이다. 평행광과 비평행광 투영법에 기초한 3D 측정 시스템의 4가지 수학적 모델이 평가되고 분석되었으며, 위상과 좌표의 관계의 성능비교 등이 제시되었다.

치의료용 3D 구강내 스캐너는 크기와 부피의 제약 때문에, 구강의 비접촉 형상측정을 수행하기가 쉽지 않다. 본 연구에서 독특한 평행광 조명에 기초한 3D 구강내 스캐너가 구강내의 치아 형상 측정을 위해 제시되었다. 또한 평행광 조명을 위한 비선형 시스템 모델들이 제안되었는데, 이는 측정시스템에 대한 더욱 정밀한 수학적 표현을 가능하게 해주고, 그 결과 측정정밀도의 개선을 가져왔다. 구강내 스캐너의 개발에 사용된 방법론과 알고리즘을 시험하고 증명하기 위하여, 실제 디지털 프린지 프로젝터(DFP) 기반 3D 스캐너와 유사한 실시간 가상 3D 스캐너를 제안하였다. 마지막으로

개발된 알고리즘과 시스템의 실현가능성과 성능을 증명하기 위하여 광학 측정과 시뮬레이션 측정 결과가 제시되었다.